

Electronically Tunable Light Modulation with Graphene and Noble Metal Plasmonics

Thesis by
Seyoon Kim

In Partial Fulfillment of the Requirements for the
degree of
Doctor of Philosophy

The logo for the California Institute of Technology (Caltech), featuring the word "Caltech" in a bold, orange, sans-serif font.

CALIFORNIA INSTITUTE OF TECHNOLOGY
Pasadena, California

2017
(Defended Oct 13, 2016)

To my mother

© 2017

Seyoon Kim

ORCID: 0000-0002-8040-9521

ACKNOWLEDGEMENTS

It was a long journey to get my PhD, and I was fortunate enough to meet a lot of great people at Caltech. First, I would like to thank Professor Harry Atwater for his endless support and patience. Harry has always encouraged me to push my limit and reach higher goals. His never-ending enthusiasm towards new science has inspired me when pursuing my studies.

I would like to thank my thesis committee members Professor Kerry Vahala, Professor David Rutledge, Professor Axel Scherer, and Professor Hyuck Choo. Their helpful advice and guidance have enabled me to complete my PhD. I would like to thank Professor Byoungcho Lee for research guidance before I entered Caltech. His teaching has made up the basis of my research. I would also like to thank Professor George Rossman for his help and assistance.

Min Seok Jang and Victor Brar have been my great mentors. I would not have been able to start working on graphene plasmonics without their help. Kelly Mauser has been my best friend, and she has spent thousands of hours correcting my English. I also thank Seokmin Jeon, Stan Burgos, and Hansuek Lee for helping me become accustomed to Caltech. I would like to thank Joeson Wong for his exfoliated graphene image.

I have been lucky enough to work with Laura Kim and Wei-Hsiang Lin on a graphene team, and Yulia Tolstova, Jeff Bosco, Sam Wilson, Nick Batara, Colton Bukowksy were the best office mates. My life could not be enjoyable without the help of Tiffany Kimoto, Jennifer Blankenship, Liz Jennings, and Lyann Lau. I also thank all Atwater group members and KNI staff. It has been my pleasure to meet Jeesoon Choi, Sang Hee Park, Jungwoo Kim, Yonghwi Kim, and many other Korean graduate students at Caltech.

Lastly, I would like to thank my family and friends in Korea. I would like to acknowledge full-support by a Samsung scholarship.

Seyoon Kim
October 2016
Pasadena, CA

ABSTRACT

Graphene is a monolayer of carbon atoms constructing a two-dimensional honeycomb structure, and it has an excellent carrier mobility and a very high thermal conductivity. Remarkably, it has been experimentally demonstrated that a monolayer graphene exhibits an exotic optical properties. To be specific, the plasmonic dispersion relation of a transverse magnetic graphene plasmon is electronically tunable by adjusting carrier density in graphene with external gate bias, and graphene plasmonic nano cavities have been utilized to modulate mid-infrared light.

In this thesis, we present how to efficiently modulate mid-infrared light by combining graphene plasmonic ribbons with noble metal plasmonic structures.

First, we propose and demonstrate electronically tunable resonant perfect absorption in graphene plasmonic metasurface enhanced by noble metal plasmonic effect, which results in modulating reflecting light. In this device, we improve coupling efficiency of free-space photons into graphene plasmons by reducing wavevector mismatching with a low permittivity substrate. In addition, the graphene plasmonic resonance is significantly enhanced by plasmonic light focusing effect of the coupled subwavelength metallic slit structure, which results in strongly fortifying resonance absorption in the graphene plasmonic metasurface. In the proposed device, theoretical calculation expects that perfect absorption in the graphene plasmonic metasurface is achievable with low graphene carrier mobility. We also present an analytical model based on surface admittance in order to fully understand how this enhancement occurs.

In the second device, we propose and demonstrate a transmission type light modulator by combining graphene plasmonic ribbons with subwavelength metal slit arrays. In this device, extraordinary optical transmission resonance is coupled to graphene plasmonic ribbons to create electrostatic modulation of mid-infrared light. Absorption in graphene plasmonic ribbons situated inside metallic slits can efficiently block the coupling channel for resonant transmission, leading to a suppression of transmission. This phenomenon is also interpreted by anti-crossing between the graphene plasmonic resonance in the ribbons and the noble metal plasmonic resonance in the subwavelength metal slit arrays.

Finally, we devise a platform to demonstrate graphene plasmonic resonance energy transport along graphene plasmonic ribbons. In this device, two metal-insulator-metal waveguides are connected by a subwavelength metal slit, and graphene plasmonic ribbons are located inside this slit. Due to the large impedance mismatch at the junction, light coupling efficiency across the junction is poor. If the graphene plasmonic ribbons are tuned to support strong graphene plasmonic

resonances, the light energy can be transferred via graphene plasmons along the ribbons, and it leads to significant improvement in the light coupling efficiency across the junction. In addition to enhanced light coupling efficiency, we also present how to totally suppress the transmission by inducing a Fano resonance between a non-resonant propagation mode across the junction and a resonant graphene plasmonic transport mode, which can be utilized to efficiently modulate light in a noble metal plasmonic waveguide with the graphene plasmon resonance energy transfer.

PUBLISHED CONTENT AND CONTRIBUTIONS

S. Kim, M. S. Jang, V. W. Brar, K. W. Mauser, and H. A. Atwater. Electronically tunable graphene plasmonic resonance energy transport (in preparation).

- S.K conceived the ideas, performed the simulations.

S. Kim, M. S. Jang, V. W. Brar, K. W. Mauser, and H. A. Atwater. Electronically tunable resonant perfect absorption in graphene plasmonic metasurface (in preparation).

- S.K conceived the ideas, performed the simulations, fabricated and measured the sample.

K. W. Mauser, S. Kim, S. Mitrovic, D. Fleischman, and H. A. Atwater. Resonant thermoelectric nanophotonics (submitted).

<https://arxiv.org/abs/1606.03313>

- S.K performed the simulations and data analysis.

S. Kim, M. S. Jang, V. W. Brar, Y. Tolstova, K. W. Mauser, and H. A. Atwater. Electronically tunable extraordinary optical transmission in graphene plasmonic ribbons coupled to subwavelength metallic slit arrays. *Nat. Commun.* **7**, 12323 (2016).

<http://dx.doi.org/10.1038/ncomms8032>

- S.K conceived the ideas, performed the simulations, fabricated and measured the sample.

V. W. Brar, M. C. Sherrott, M. S. Jang, S. Kim, L. Kim, M. Choi, L. A. Sweatlock, and H. A. Atwater. Electronic modulation of infrared radiation in graphene plasmonic resonators. *Nat. Commun.* **6**, 7032 (2015).

<http://dx.doi.org/10.1038/ncomms8032>

- S.K fabricated the sample.

M. S. Jang, V. W. Brar, M. C. Sherrott, J. J. Lopez, L. Kim, S. Kim, M. Choi, and H. A. Atwater. Tunable large resonant absorption in a midinfrared graphene Salisbury screen. *Phys. Rev. B* **90**, 165409 (2014).

<http://dx.doi.org/10.1103/PhysRevB.90.165409>

- S.K participated in preparing the sample.

V. W. Brar, M. S. Jang, M. Sherrott, S. Kim, J. J. Lopez, L. B. Kim, M. Choi, and H. A. Atwater. Hybrid surface-phonon-plasmon polariton modes in graphene/monolayer h-BN heterostructures. *Nano Lett.* **14**, 3876-3880 (2014).

<http://dx.doi.org/10.1021/nl501096s>

- S.K participated in preparing the sample and measuring the optical properties of the sample.

CONTENTS

Acknowledgements	i
Abstract	ii
Published Content and Contributions	iv
Contents.....	v
List of Illustrations and/or Tables	viii
1. Introduction	1
1.1 Plasmonics on Noble Metal Surfaces.....	1
1.1.1 Surface Plasmon Polaritons Dispersion Relation	1
1.1.2 Plasmonic Nanobar Antennas	4
1.1.3 Extraordinary Optical Transmission	6
1.1.4 Plasmonic Metal-Insulator-Metal Waveguide.....	8
1.1.5 Limitation in Tunable Plasmonic Resonance	9
1.2 Graphene	10
1.2.1 Tunable Optical Properties in Graphene	11
1.2.2 Light Modulation via Graphene Plasmons	12
1.3 Scope of this Thesis.....	15
1.3.1 Electronically Tunable Resonant Absorption in Graphene Plasmonic Metasurface Enhanced by Noble Metal Plasmonic Effect.....	15
1.3.2 Electronically Tunable Extraordinary Optical Transmission in Graphene Plasmonic Ribbons Coupled to Subwavelength Metallic Slit Arrays	16
1.3.3 Electronically Tunable Graphene Plasmonic Resonance Energy Transport.....	16
2. Graphene Plasmons and Chemical Vapor Deposition Grown Graphene	18
2.1 Graphene Plasmons	18
2.1.1 Dispersion Relation of Graphene Plasmons	19
2.1.2 Perfect Absorption in Graphene Plasmonic Ribbons	22
2.1.3 Modeling Graphene in Electromagnetics	25
2.2 Chemical Vapor Deposition Grown Graphene.....	27
2.2.1 Graphene Growth in Chemical Vapor Deposition Method	27
2.2.2 Graphene Transfer	30
2.2.3 Raman Spectroscopy of Graphene.....	32
2.2.4 Transport Measurement.....	35

3. Electronically Tunable Resonant Perfect Absorption in Graphene Plasmonic Metasurface.....	39
3.1 Introduction	40
3.2 Device Geometry and Light Modulation Mechanism	41
3.3 Type A: Graphene Plasmons on Low Permittivity Substrate	43
3.3.1 Electric Field Enhancement by Salisbury Screen.....	43
3.3.2 Graphene Plasmon Dispersion Relation.....	45
3.3.3 Perfect Absorption in Graphene Plasmonic Ribbons	47
3.4 Type B and C: Coupled Subwavelength Metal Slits	48
3.4.1 Field Enhancement in Subwavelength Metal Slits	48
3.4.2 Perfect Absorption with Lower Graphene Carrier Mobility.....	49
3.4.3 Image Graphene Plasmonic Ribbons	52
3.5 Surface Admittance Model	53
3.5.1 Surface Admittance of Metasurface.....	53
3.5.2 Analytic Model for Calculating Absorption.....	57
3.5.3 Critical Coupling	57
3.5.4 Perfect Absorption with Lower Graphene Carrier Mobility.....	62
3.6 Experimental Measurements.....	64
3.6.1 Characteristics of Graphene.....	64
3.6.2 Mid-Infrared Measurements	66
3.6.3 Numerical Fitting	68
3.7 Conclusions	69
4. Electronically Tunable Extraordinary Optical Transmission in Graphene Plasmonic Ribbons Coupled to Subwavelength Metallic Slit Arrays.....	70
4.1 Introduction	71
4.2 Device Geometry and Light Modulation Mechanism	72
4.3 Substrate Geometry Optimization.....	74
4.4 Theoretical Modulation of Coupled Structure.....	76
4.4.1 Light Modulation in Coupled Structure	76
4.4.2 Dependency on Graphene Carrier Mobility	78
4.5 Anti-Crossing Behavior in Coupled Structure	79
4.5.1 Dependence on Number of Intergap Graphene Plasmonic Ribbons.....	81
4.5.2 Dependency on Graphene Carrier Mobility	82
4.5.3 Absorption-Induced Transparency.....	84

4.6	Experimental Measurements.....	84
4.6.1	Characteristics of Graphene.....	85
4.6.2	Light Modulation in Transmission.....	86
4.6.3	Broad Angular Distribution Effect.....	87
4.6.4	Numerical Fitting	89
4.7	Conclusions	90
5.	Electronically Tunable Graphene Plasmonic Resonance Energy Transport	91
5.1	Introduction	92
5.2	Graphene Plasmonic Resonance Energy Transport.....	93
5.2.1	Energy Transfer from MIM Waveguide Mode to Graphene Plasmonic Mode.....	95
5.2.2	Energy Propagation along Graphene Plasmonic Ribbons	96
5.3	Electronically Tunable Light Modulation in MIM Waveguides Connected by a Subwavelength Metal Slit	99
5.3.1	Light Transmission across the Subwavelength Metal Slit.....	99
5.3.2	Fano Resonance within the Subwavelength Metal Slit	102
5.3.3	Light Modulation Efficiency Dependent on Graphene Carrier Mobility	105
5.4	Conclusions	106
	Bibliography.....	108

LIST OF ILLUSTRATIONS AND/OR TABLES

Figure 1.1 Surface plasmon polariton on semi-infinite metal surface.....	2
Figure 1.2 Surface gratings.	4
Figure 1.3 Plasmonic nanobar antennas.	5
Figure 1.4 Extraordinary optical transmission.....	7
Figure 1.5 Plasmonic metal-insulator-metal waveguide.....	8
Figure 1.6 Graphene.....	10
Figure 1.7 Light modulation via interband transition.	12
Figure 1.8 Light modulation in graphene plasmonic ribbons.	14
Figure 2.1 Graphene plasmonic waveguide.....	20
Figure 2.2 Insulator-metal-insulator plasmonic waveguide.....	21
Figure 2.3 Graphene plasmonic ribbons on Salisbury screen.	22
Figure 2.4 Perfect absorption in graphene plasmonic ribbons.	24
Figure 2.5 Graphene optical surface conductivity.	26
Figure 2.6 Graphene dielectric function.	27
Figure 2.7 Graphene growth in chemical vapor deposition method.....	28
Figure 2.8 Graphene images.....	29
Figure 2.9 Defective graphene growth.	30
Figure 2.10 Graphene transfer.....	31
Figure 2.11 Defective graphene transfer.	32
Figure 2.12 Raman spectrum of graphene.....	32
Figure 2.13 Phonon vibrations in graphene.	33
Figure 2.14 Raman spectral process in graphene.....	34
Figure 2.15 Transport measurement.....	36
Figure 2.16 Graphene doping.....	37
Figure 3.1 Device geometry.....	42
Table 3.1 Conditions for perfect absorption at $1,356\text{ cm}^{-1}$	43
Figure 3.2 Substrate-dependent field enhancement.	44
Figure 3.3 Substrate-dependent electric field distributions.....	45
Figure 3.4 Graphene plasmons on low permittivity substrate.....	46
Figure 3.5 Graphene plasmonic ribbons.....	47
Figure 3.6 Subwavelength metal slits.....	48

Figure 3.7 Graphene plasmonic ribbons coupled to subwavelength metal slits.	49
Figure 3.8 Enhanced light-matter interactions in graphene plasmonic ribbons.....	50
Figure 3.9 Absorption maps.....	51
Figure 3.10 Image graphene plasmonic ribbons.....	52
Figure 3.11 Schematic of surface admittance.....	54
Figure 3.12 Surface admittance fitting.....	56
Figure 3.13 Surface admittance chart.....	58
Figure 3.14 Dependency on substrate thickness.....	59
Figure 3.15 Subwavelength metal slit effect on surface admittance.....	61
Figure 3.16 Dependency on structural geometries.....	62
Figure 3.17 Perfect absorption with lower graphene carrier mobility.....	63
Figure 3.18 Characteristics of experiment sample.....	65
Figure 3.19 Mid-infrared measurements.....	66
Table 3.2 Summary of measurement results.....	67
Figure 3.20 Measurement summary.....	67
Figure 3.21 Numerical fitting.....	68
Figure 4.1 Device and working mechanism.....	72
Figure 4.2 Bare graphene plasmonic ribbons.....	73
Figure 4.3 Characteristic of membrane.....	74
Figure 4.4 Resonance in a substrate.....	75
Figure 4.5 Graphene plasmonic ribbons.....	76
Figure 4.6 Coupled structure simulations.....	77
Figure 4.7 Light modulation in transmission.....	79
Figure 4.8 Anti-crossing behavior in the coupled structure.....	80
Figure 4.9 Anti-crossing behavior dependence on graphene carrier mobility.....	83
Figure 4.10 Characteristics of graphene.....	85
Figure 4.11 Experimental results.....	86
Figure 4.12 Broad angular distribution effect.....	88
Figure 4.13 Numerical fitting.....	89
Figure 5.1 Plasmonic resonance energy transport.....	93
Figure 5.2 Schematic of launching graphene plasmonic resonance energy transport.....	94
Figure 5.3 Energy transfer.....	95
Figure 5.4 Energy propagation.....	96

Figure 5.5 Energy transport.....	97
Figure 5.6 Electric field distribution comparison.	98
Figure 5.7 Schematic of device.	99
Figure 5.8 Light modulation by intergap graphene plasmonic ribbons.....	100
Figure 5.9 Electric field and power flow distributions.	101
Figure 5.10 Transmission coefficients.....	103
Figure 5.11 Light modulation by an intergap graphene sheet.	104
Figure 5.12 Dependency on graphene carrier mobility.	106

CHAPTER 1

INTRODUCTION

1.1 Plasmonics on Noble Metal Surfaces

Light has been utilized in a wide range of fields including optical imaging, data storage, energy conversion, communication, analytical chemistry, and photochemistry [1-5]. A major issue in those fields is how to overcome the diffraction limit in order to increase optical resolution [6]. In addition, intensifying the light-matter interaction is also important in light-energy conversion and photon-mediated reactions [7, 8]. These aspects are the reason why the field of plasmonics has drawn considerable attention. Surface plasmon polaritons are a longitudinal electromagnetic wave coupled to free carriers collectively oscillating on noble metal surface [9]. Due to its low-dimensional properties [10], surface plasmon polaritons excited on noble metal surfaces can confine light below the optical diffraction limit and significantly enhance the light intensity in a nanoscale local region resulting in strong light-matter interaction. Enormous advances in nanoscale fabrication technology allow for realization of subwavelength metallic structures exhibiting interesting plasmonic effect such as plasmonic optical circuits, artificially created metasurfaces, surface enhanced Raman scattering, plasmonic beam shaping, and beam focusing in subwavelength scale [11-15].

1.1.1 Surface Plasmon Polaritons Dispersion Relation

Surface plasmon polariton excited on metal/dielectric interface, as shown in Figs. 1.1(a) and (b), is characterized by dispersion relation derived from phase matching condition of Maxwell's equations, and the dispersion relation is given by [16]

$$\omega = c_0 k_{sp} \sqrt{\frac{\epsilon_m + \epsilon_d}{\epsilon_m \epsilon_d}} \quad (1.1)$$

where c_0 is the light speed in air, k_{sp} is the propagation constant of surface plasmon polariton, and ϵ_m and ϵ_d are the frequency-dependent permittivities of the metal and the dielectric, respectively.

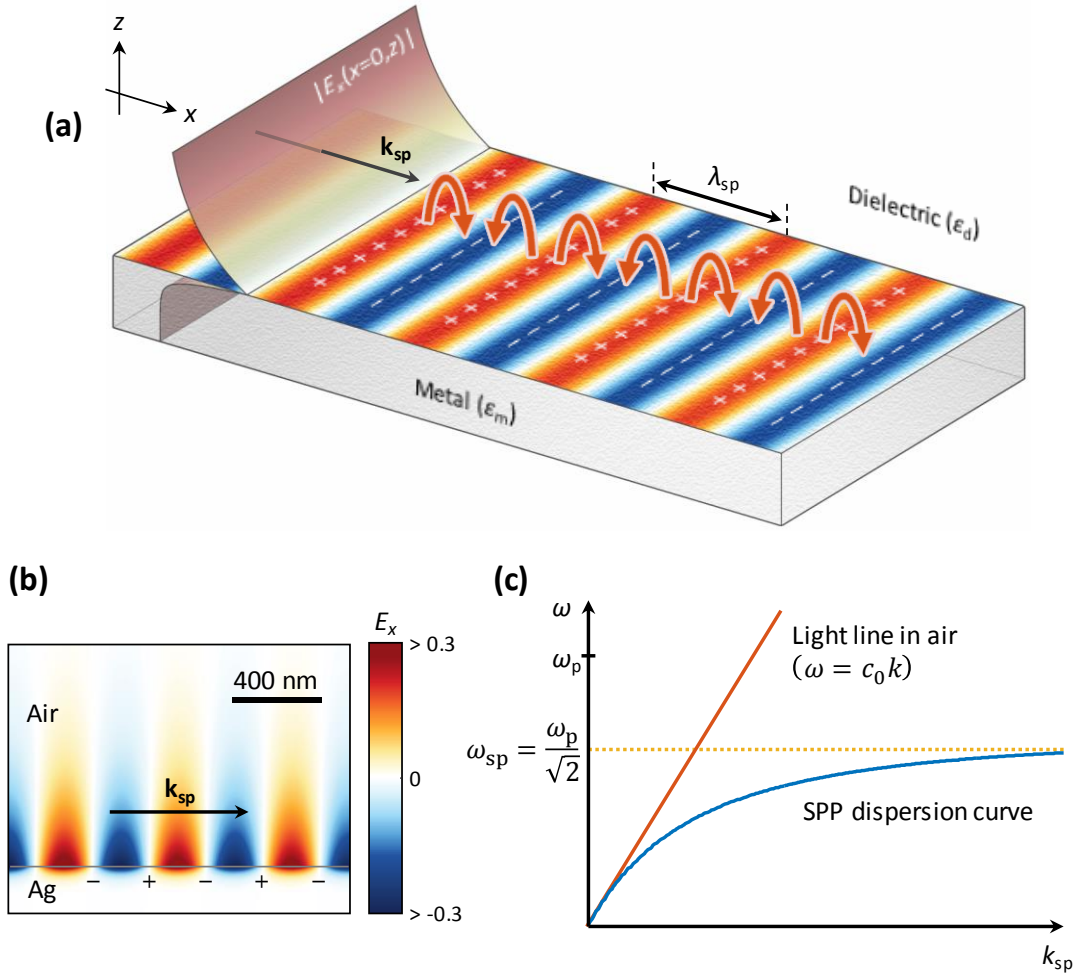


Figure 1.1 | Surface plasmon polariton on semi-infinite metal surface. (a) Schematic of surface plasmon polariton (SPP) excited on metal/dielectric interface displaying induced surface charges (red: holes, blue: electrons) on the metal surface and electric fields. (b) E_x field distribution of SPP excited on Ag/air interface. Free-space wavelength is 532 nm, and the propagation constant normalized by free-space wavenumber (k_{sp}/k_0) is calculated by $1.05+i0.46$ with $\epsilon_{Ag}=-10.2+i0.83$ [17]. (c) Schematic of SPP dispersion curve excited on metal/air interface.

In the Drude model, the conduction electrons in metal is treated as an ideal gas moving freely between scattering events [18]. Neglecting the oscillation damping of the electrons in the metal [19], and the relative permittivity of the metal can be written as

$$\epsilon_m(\omega) \approx 1 - \frac{\omega_p^2}{\omega^2} \quad (1.2)$$

where $\omega_p = \sqrt{Ne^2/\epsilon_0 m}$ is the plasma frequency, N is the conduction electron density in the metal, e is the elementary charge, and m is the electron mass. In Eq. (1.2), the important point is that the

permittivity of the metal can be negative below the plasma frequency, and it can satisfy the following condition in Eq. (1.3) [20]:

$$\varepsilon_m(\omega_{sp}) + \varepsilon_d(\omega_{sp}) = 0 \quad (1.3)$$

This condition makes a zero numerator in Eq. (1.1), and it indicates collective oscillations bound to the metal/dielectric interface with infinite surface plasmon propagation [20]. Assuming that air is the homogeneous dielectric medium ($\varepsilon_d=1$), Eq. (1.4) is derived from Eqs. (1.2) and (1.3).

$$\omega_{sp} = \frac{\omega_p}{\sqrt{2}} \quad (1.4)$$

On the metal/air interface, the surface plasmon polariton dispersion relation is given by Eq. (1.5) from Eqs. (1.1) and (1.2), and the dispersion curve is plotted in Fig. 1.1(c) [19].

$$\omega = \sqrt{\frac{\omega_p^2}{2} + (c_0 k_{sp})^2 - \left[\frac{\omega_p^4}{2} + (c_0 k_{sp})^2 \right]^{1/2}} \quad (1.5)$$

In Eq. (1.5), the dispersion curve approaches the light line in air ($\omega=c_0k$) at a small propagation constant limit ($k_{sp} \ll \omega_p/c_0$). When $k_{sp} \gg \omega_p/c_0$, the dispersion curve is saturated to the ω_{sp} in Eq. (1.4).

As shown in Fig. 1.1(c), the propagation constant of surface plasmon polariton is always larger than the wavevector in air, and it indicates that we can confine the light below subwavelength scale by surface plasmon polaritons. In addition, it implies that it is not possible to match the non-radiative surface plasmon resonance condition by free-space light in air. To overcome this wavevector mismatch, we need to diffract light using corrugated structures such as surface gratings [19]. In Fig. 1.2, the surface plasmon polariton is excited on Ag substrate by dielectric surface gratings diffracting incoming Gaussian beam to match the surface plasmon resonance condition.

In the following section, we will briefly review three representative plasmonic structures in visible range: plasmonic nanobar antennas enhancing near-field intensity, subwavelength metal slit array exhibiting extraordinary optical transmission, and plasmonic metal-insulator-metal waveguide having subwavelength gap. These plasmonic structures will be coupled to graphene plasmonic light modulators through this thesis in order to enhance the light modulation performance.

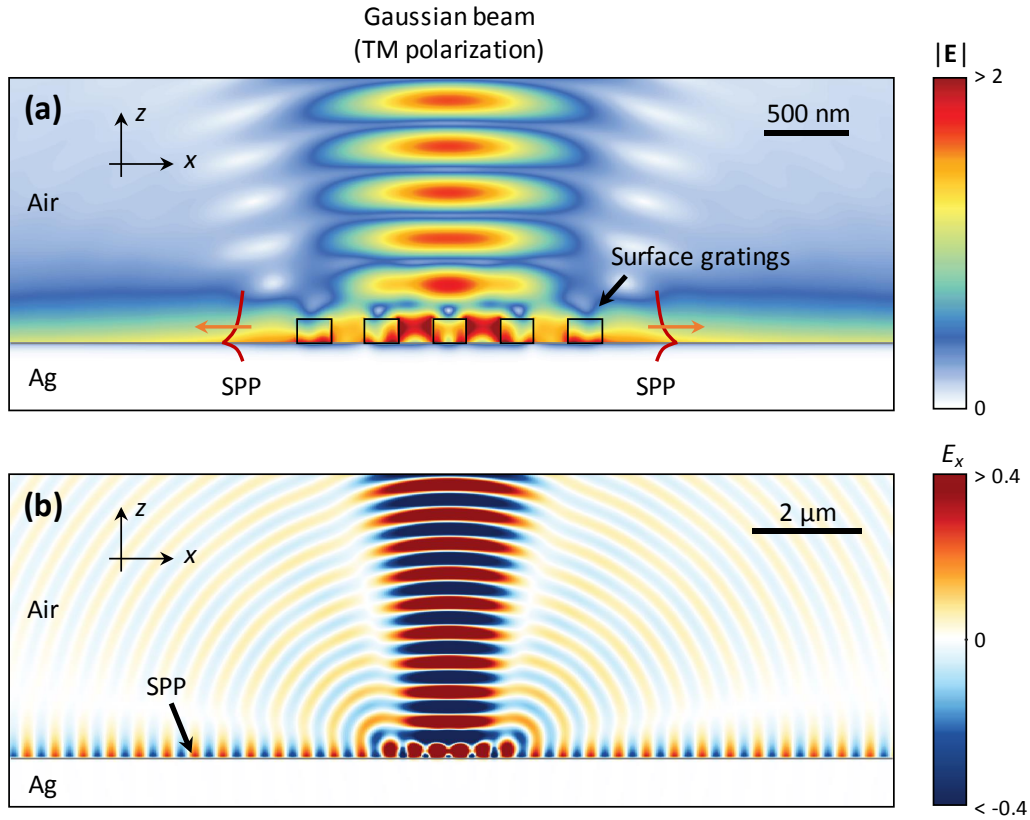


Figure 1.2 | Surface gratings. (a) Electric field distribution and (b) E_x field distribution of surface plasmon polariton (SPP) on Ag/air interface excited by surface gratings with a Gaussian beam (beam width=500 nm). Free-space wavelength is 532 nm. Five surface gratings consist of SiO_2 ($\epsilon_{\text{SiO}_2}=2.13$) [17], and the grating pitch, the grating width, and the grating thickness are 400 nm, 200 nm, and 140 nm, respectively.

1.1.2 Plasmonic Nanobar Antennas

Compared to surface plasmon polaritons propagating on a flat metal surface, localized surface plasmons are confined within finite size geometries, such as nanoparticles or nanobars, and those structures' size is in subwavelength scale [9]. The advantage of the subwavelength plasmonic structures is that they can capture more light than its physical size by localized surface plasmon resonance, and it results in significantly enhancing near field intensity around the subwavelength plasmonic structures. This property has been utilized in surface enhanced Raman spectroscopy, photovoltaic, and plasmonic sensors in order to intensify the light-matter interaction, resulting in increasing the efficiencies of the devices [7, 13, 21].

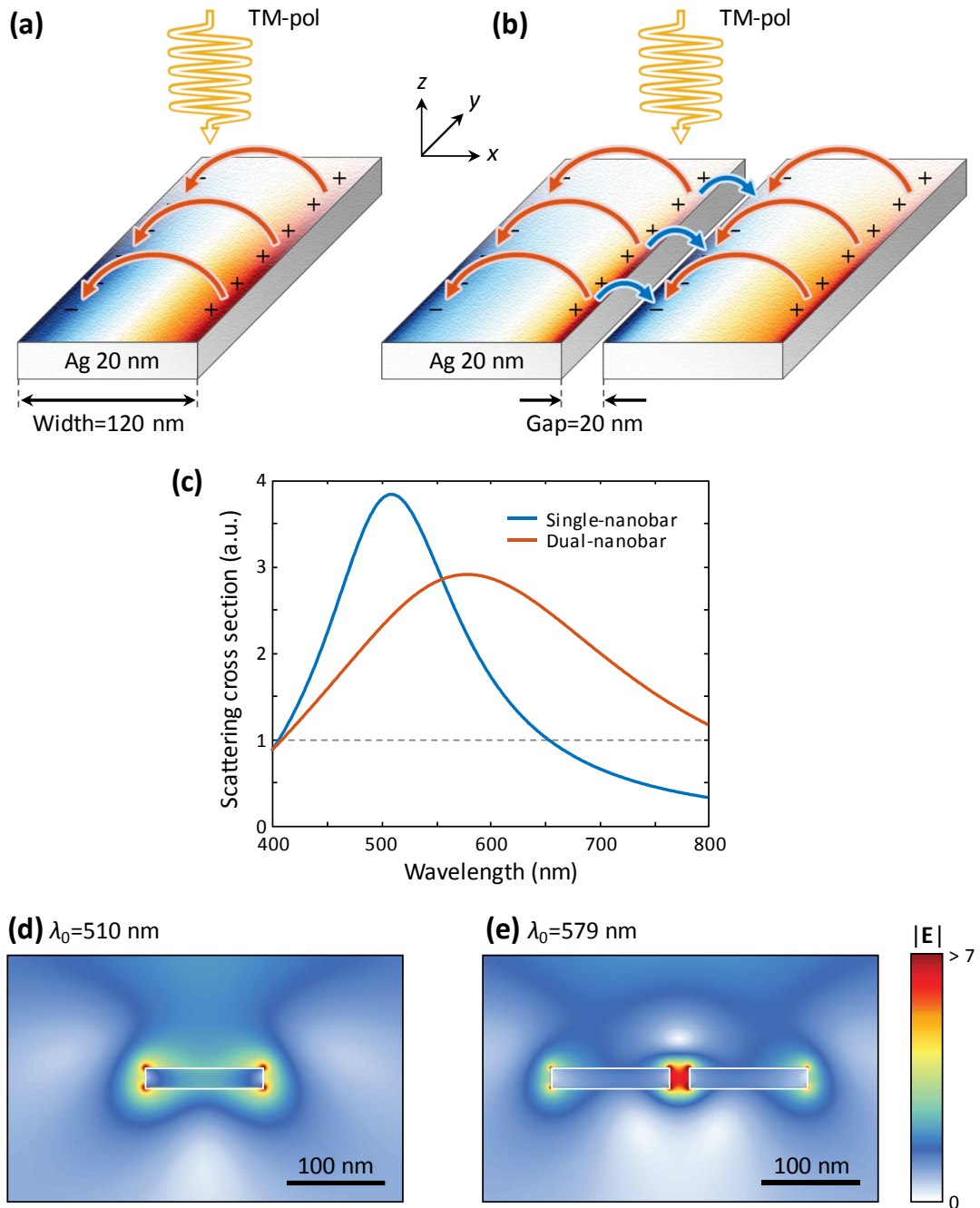


Figure 1.3 | Plasmonic nanobar antennas. Schematics of (a) a single-nanobar plasmonic antenna and (b) a dual-nanobar plasmonic antenna. In (a) and (b), the red and the blue arrows denote plasmons and interaction between antennas, respectively. The overlapped distributions represent the charge distribution on the surfaces (red: holes, blue: electrons). (c) Simulation results of scattering cross section of the plasmonic antennas. Electric field distributions of (d) the single-nanobar plasmonic antenna and (e) the dual-nanobar plasmonic antennas at their resonance frequencies.

Figure 1.3 shows simulation results of plasmonic antennas consisting of subwavelength nanobars. Both plasmonic antennas surrounded by air consist of 20 nm thick Ag and each antenna width is 120 nm (Figs. 1.3(a) and (b)). In the dual-nanobar plasmonic antenna, gap is 20 nm. As shown in Fig. 1.3(c), both plasmonic antennas exhibit plasmonic resonance, and their scattering cross sections exceed their physical size (i.e. antenna width). It indicates that they can capture more light than their physical size at the localized surface plasmon resonances, denoted as the arrows in Figs. 1.3(a) and (b). As a result of the localized surface plasmon resonance, near fields around the plasmonic antennas are significantly enhanced, as shown in Figs. 1.3(d) and (e).

Compared with the single-nanobar antenna, the dual-nanobar antenna displays redshift in its spectrum, and this redshift originates from plasmonic interaction between two adjacent plasmonic antennas [22], which corresponds to the blue arrow in Fig. 1.3(b). As a result of the plasmonic interaction, the dual-nanobar plasmonic antenna strongly intensifies the inter-gap field, which could lead to inducing strong light-matter interaction inside the subwavelength metal gap.

1.1.3 Extraordinary Optical Transmission

In classical electromagnetic theory, light passing through a subwavelength aperture is diffracted in all directions, and its transmission is suppressed by diffraction limit. In 1998, it has been demonstrated that subwavelength metal aperture array exhibits strong transmission into a forward direction at a certain frequency even through the aperture in deep-subwavelength scale [23]. This exotic optical phenomenon has been called as extraordinary optical transmission (EOT), and it has been proved that the EOT originates from the surface plasmon resonance [24, 25].

Figure 1.4(a) shows the mechanism of the EOT through subwavelength metal slit array. Transverse magnetic (TM) polarized incoming light is diffracted by the periodically corrugated structure, and the scattered lights induce surface plasmons on the top metal surface. The surface plasmons then tunnel through the subwavelength metal slits and excite surface plasmons on the bottom metal surface. The surface plasmon on the bottom metal surface subsequently re-radiates into free space, resulting in strong transmission into a forward direction at the EOT resonance frequency, as shown in Fig. 1.4(b). At the EOT resonance, the absorption is also maximized due to the strong plasmonic resonance effect, as shown in Fig. 1.4(b).

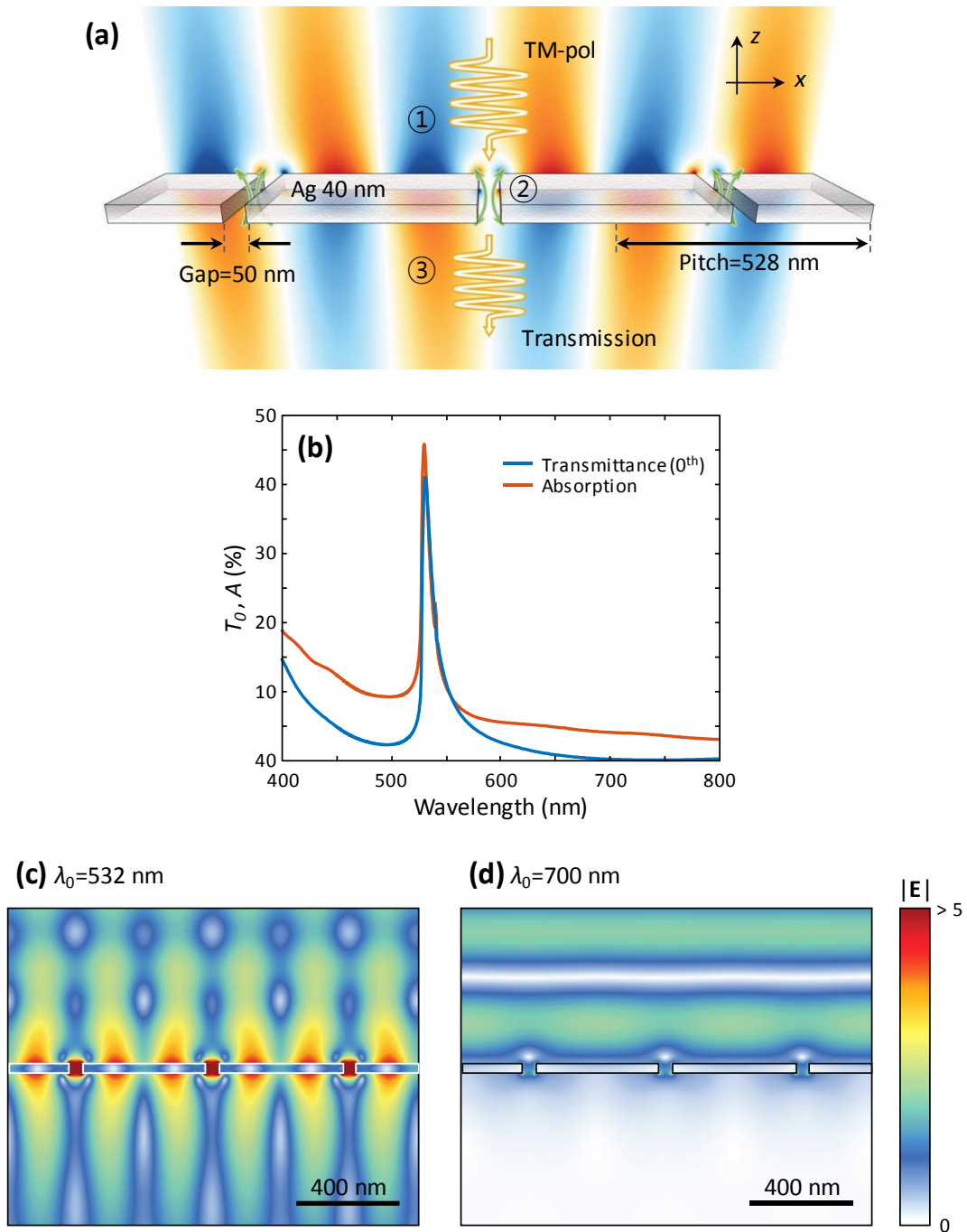


Figure 1.4 | Extraordinary optical transmission. (a) Schematic of EOT through subwavelength metal slit array. The overlapped field distribution corresponds to $\text{Re}(E_z)$. (b) Simulation results of the EOT spectrum exhibiting strong transmission at free-space wavelength $\lambda_0=532$ nm. Electric field distributions (c) at the EOT resonance ($\lambda_0=532$ nm) showing strong surface plasmons and (d) far from the EOT resonance ($\lambda_0=700$ nm).

The subwavelength metal slits play a pivotal role in EOT [26, 27]. Due to the optical coupling between the surface plasmons on the top and bottom metal surfaces, significantly enhanced intergap electric fields are exhibited in Fig.1.4(c). For frequency far away from the EOT resonance, there is no strong surface plasmon on the top and the bottom side, and the intergap electric fields are not enhanced, as shown in Fig. 1.4(d).

1.1.4 Plasmonic Metal-Insulator-Metal Waveguide

In an optical fiber, the core size is limited by the diffraction limit, and the smallest diameter is in the order of free-space wavelength divided by refractive index of the core. It means that it is difficult to realize highly integrated optical circuits with dielectric based waveguides. However, the optical circuit size can be miniaturized to subwavelength scale with plasmonic waveguides because of the high confinement factor of plasmons [11].

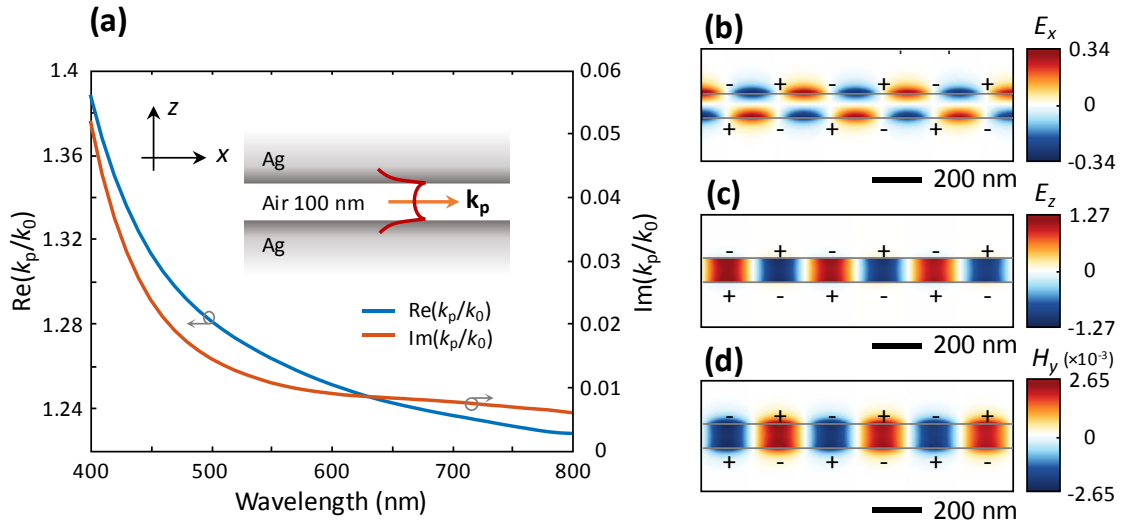


Figure 1.5 | Plasmonic metal-insulator-metal waveguide. (a) Schematic of plasmonic MIM waveguide and its frequency-dependent dispersion relation. (b) E_x , (c) E_z , and (d) H_y field distributions of the plasmonic MIM waveguide at $\lambda_0 = 532$ nm. The (+) and (-) signs denote the induced surface charges coupled to the surface plasmon polaritons.

Figure 1.5(a) shows the schematic of plasmonic metal-insulator-metal (MIM) waveguide consisting of 100 nm of air gap and Ag clads and its frequency-dependent dispersion relation. In this plasmonic MIM waveguide, the electromagnetic wave is highly confined within the subwavelength air gap due to the low-dimensional property of the plasmons, as shown Figs. 1.5(b-d).

To calculate the dispersion relation of the fundamental plasmonic waveguide mode, we have to consider the field continuity boundary conditions between the top and bottom air/metal interfaces, and the propagation constant the propagating mode k_p corresponds to the root of the characteristic equation given by [28]

$$\begin{aligned} & \left(\frac{\varepsilon_{\text{air}} k_{z,\text{Ag}}}{\varepsilon_{\text{Ag}} k_{z,\text{air}}} + 1 \right) \left(\frac{\varepsilon_{\text{air}} k_{z,\text{Ag}}}{\varepsilon_{\text{Ag}} k_{z,\text{air}}} + 1 \right) \\ & - \left(\frac{\varepsilon_{\text{air}} k_{z,\text{Ag}}}{\varepsilon_{\text{Ag}} k_{z,\text{air}}} - 1 \right) \left(\frac{\varepsilon_{\text{air}} k_{z,\text{Ag}}}{\varepsilon_{\text{Ag}} k_{z,\text{air}}} - 1 \right) \exp(i2k_{z,\text{air}} d_{\text{air}}) = 0 \end{aligned} \quad (1.6)$$

where $k_{z,\text{air}} = k_0 \sqrt{\varepsilon_{\text{air}} - (k_p/k_0)^2}$, $k_{z,\text{Ag}} = k_0 \sqrt{\varepsilon_{\text{Ag}} - (k_p/k_0)^2}$, and d_{air} is the air thickness inside the core. For an infinite air core ($d_{\text{air}} = \infty$), Eq. (1.6) becomes the dispersion relation of surface plasmon polariton on a semi-infinite metal surface in Eq. (1.1) because $k_{z,\text{air}}$ is always imaginary due to the fact that the surface plasmons are bound to the air/metal interface.

1.1.5 Limitation in Tunable Plasmonic Resonance

Although plasmons on noble metal surfaces possess a lot of benefits in terms of enhancing light-matter interaction and reducing optical device size into subwavelength scale, electrically tuning the plasmonic response for light modulation is not easily achievable. The main reason for this difficulty is the fact that such plasmons are excited on noble metal surfaces with high free carrier density. To tune the plasmonic resonance, we have to adjust the permittivities of noble metals by increasing or decreasing their free carrier densities in Eq. (1.2). However, the carrier density of noble metals supporting surface plasmons, such as Au or Ag, is in the order of 10^{22} cm^{-3} , and this value is too high to adjust by external electrical bias. There are some alternative strategies to tune the plasmons resonance by coupling plasmonic structures with electro-optic materials, adjusting the size of plasmonic structures, or utilizing phase transition in surrounding materials [29-34]. Potential drawbacks in the alternative ways to tune the plasmonic resonance is that switching speed would be limited by the relaxation time, tunability would be not enough for ultra-speed light modulation, or large scale of active region would be required to achieve desirable light modulation efficiency.

1.2 Graphene

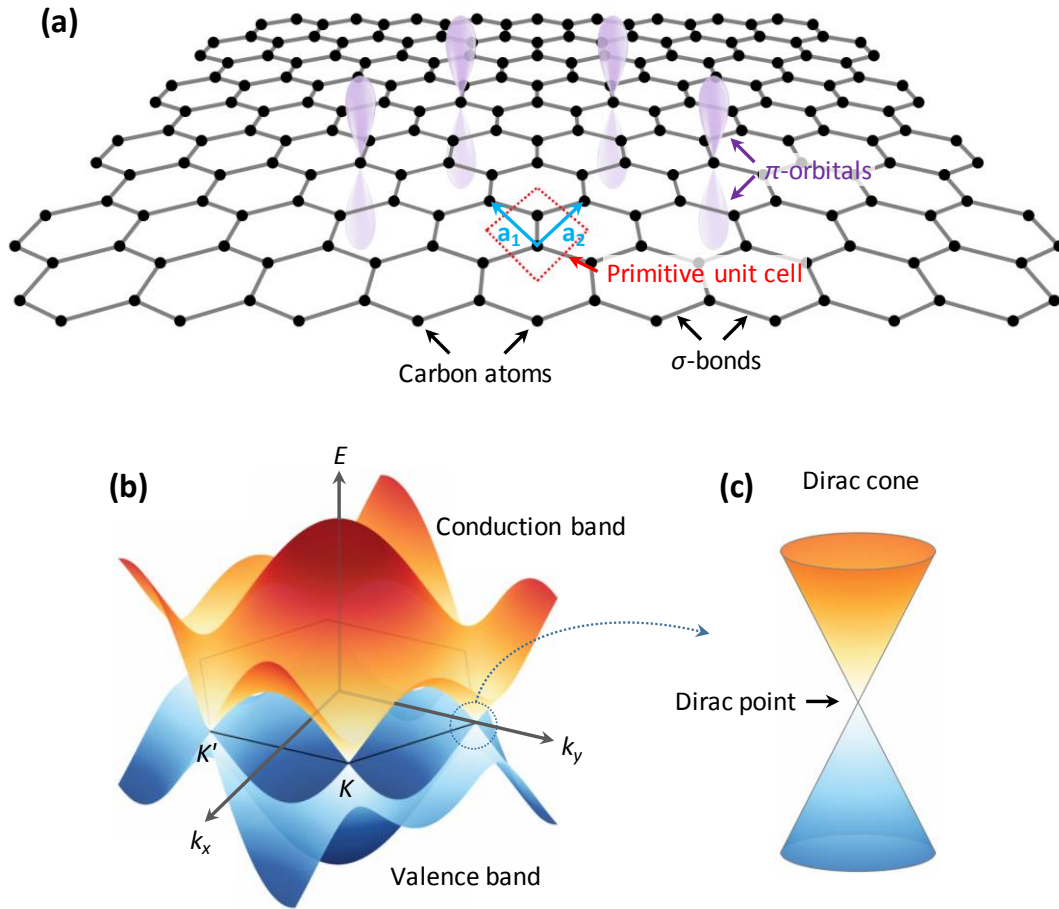


Figure 1.6 | Graphene. (a) Schematic of monolayer graphene. The \mathbf{a}_1 and the \mathbf{a}_2 denote primitive basis vectors. Electronic band structure (b) in the honeycomb lattice graphene and (c) at the Dirac points.

Graphene is a monolayer of carbon atoms constructing two-dimensional honeycomb lattice having two sp^2 -bonded atoms in the primitive unit cell [35], as shown in Fig. 1.6(a). In the graphene, electrons in carbon atoms corresponding to $2S$, $2P_x$, and $2P_y$ make the σ -bonds between the adjacent carbon atoms, and the remaining $2P_z$ electrons form the π -orbitals determining the low-energy electronic band structure [36], and the electronic dispersion relation neglecting the next nearest-neighbor hopping energy is given by [37]

$$E = \pm t \sqrt{3 + 2 \cos(\sqrt{3}k_y a) + 4 \cos\left(\frac{\sqrt{3}}{2}k_y a\right) \cdot \cos\left(\frac{3}{2}k_x a\right)} \quad (1.7)$$

where t is the nearest-neighbor hopping energy (~ 2.8 eV), a is the carbon-carbon distance (~ 1.42 Å) and the (+) and the (-) denote the conduction band and the valence band, respectively, and the electronic band structure is shown in Fig. 1.6(b).

The monolayer graphene possess a lot of exotic physical properties: strong mechanical properties with an intrinsic tensile strength of 130 GPa and Young's modulus of 1 TPa [38], a high thermal conductivity of about 5 kW/mK [39]. In particular, graphene exhibits a superior electrical property with a superior carrier mobility because the graphene has a linear electronic dispersion relation at K and the K' points, which results in massless Dirac Fermions in graphene [35], approximated by

$$E \approx \pm \hbar v_F \sqrt{k_x^2 + k_y^2} \quad (1.8)$$

where v_F is the Fermi velocity in graphene ($v_F \approx 1 \times 10^8$ cm/s). Here, the crossing points are called as Dirac point [37], and the conduction and valence bands meet at the Dirac points, as shown in Fig. 1.6(c),

1.2.1 Tunable Optical Properties in Graphene

One of the most important properties of graphene is that graphene carrier density is tunable by doping the graphene, and the doping is achievable via external electronic bias. In an electrostatic gating method, the graphene carrier density is tunable from charge neutral point to the order of 10^{13} cm⁻². It means that we can electronically tune the optical response of graphene as well as the surface conductivity in graphene.

Figure 1.7 shows a simple light modulation via interband transition in graphene. When light is illuminated on a monolayer graphene in Fig. 1.7(a), there is different light absorption mechanisms depending on the graphene Fermi level E_F , or doping level. If $E_F < \hbar\omega/2$, the incoming photon is absorbed by inducing interband transition. In this interband absorption, the absorbance is about 2.3% independent of the photon energy, and it is called as a universal absorbance [40]. In intraband transition regime ($E_F > \hbar\omega/2$), the interband transition is suppressed by Pauli blocking, and the absorbance becomes much smaller than the universal absorbance, as shown in Fig. 1.7(b). The smooth transition between the interband absorption and the intraband absorption originates from Fermi-Dirac distribution of the free carriers in graphene. As a result of light absorption, the transmitted light is modulated as a function of the graphene Fermi level, as shown in Fig. 1.7(c), and this light modulation is achievable by electrical gating method.

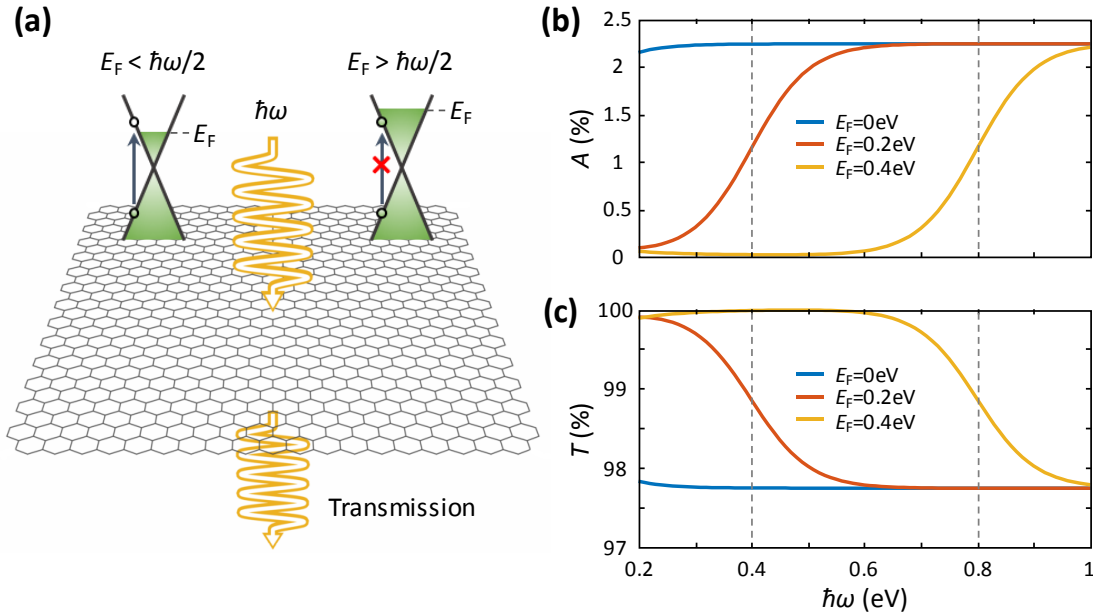


Figure 1.7 | Light modulation via interband transition. (a) Schematic of light modulation via interband transition in graphene surrounded by air. (b) Simulation results of absorption spectrum and (c) transmission spectrum depending on different graphene Fermi level (E_F). In this simulation, the graphene carrier mobility is assumed as $10,000 \text{ cm}^2\text{V}^{-1}\text{s}^{-1}$.

1.2.2 Light Modulation via Graphene Plasmons

It has been reported that free carries in graphene can be coupled with photons, and it excites plasmons in graphene similar to the plasmons on noble metal surface [41-43]. Compared with the noble metal plasmons, it has been reported that the graphene plasmon exhibit lower loss as propagating. In addition, the graphene plasmon exhibits significantly larger confinement factor (~ 100) than the noble metal plasmons [44], and this property is beneficial to miniaturize the graphene plasmonic devices. The most important advantage in graphene plasmons is that it is possible to electronically adjust the carrier density of graphene, and it allows us to directly tune the strong graphene plasmonic resonance from mid-infrared to terahertz range [45-50], which is not possible in the noble metal plasmons.

Figure 1.8 shows light modulation using simple graphene plasmonic ribbons (GPRs) array. In Fig. 1.8(a), TM polarized light is illuminated onto the GPRs with width/gap=100 nm/100 nm, and the graphene carrier mobility is assumed as $10,000 \text{ cm}^2\text{V}^{-1}\text{s}^{-1}$ in this simulation. If the graphene Fermi level is tuned to match the graphene plasmonic resonance condition between the light frequency and the graphene plasmon wavevector, the incoming light excites graphene plasmons in the GPRs, and it results in light modulation via graphene plasmonic absorption. As mentioned

before, the graphene Fermi level is adjustable by gating bias, and it indicates that the light modulation is also tunable depending on the graphene Fermi levels, as shown in Figs. 1.8(b) and (c). Figs. 1.8(d-f) shows field distributions around the GPRs with graphene plasmons, and the near fields are significantly enhanced at the graphene plasmonic resonance.

In addition, we can observe that the size of the GPRs is comparable to the plasmonic nanobar antennas in Fig. 1.3 although the wavelength of the GPRs is more than 10 times longer than the wavelength of the plasmonic nanobar antennas. It indicates that the confinement factor in the graphene plasmons is significantly larger than the noble metal plasmons. Compared with the light modulation via interband transition, we can also obtain strong light modulation effect by exploiting the tunable graphene plasmons.

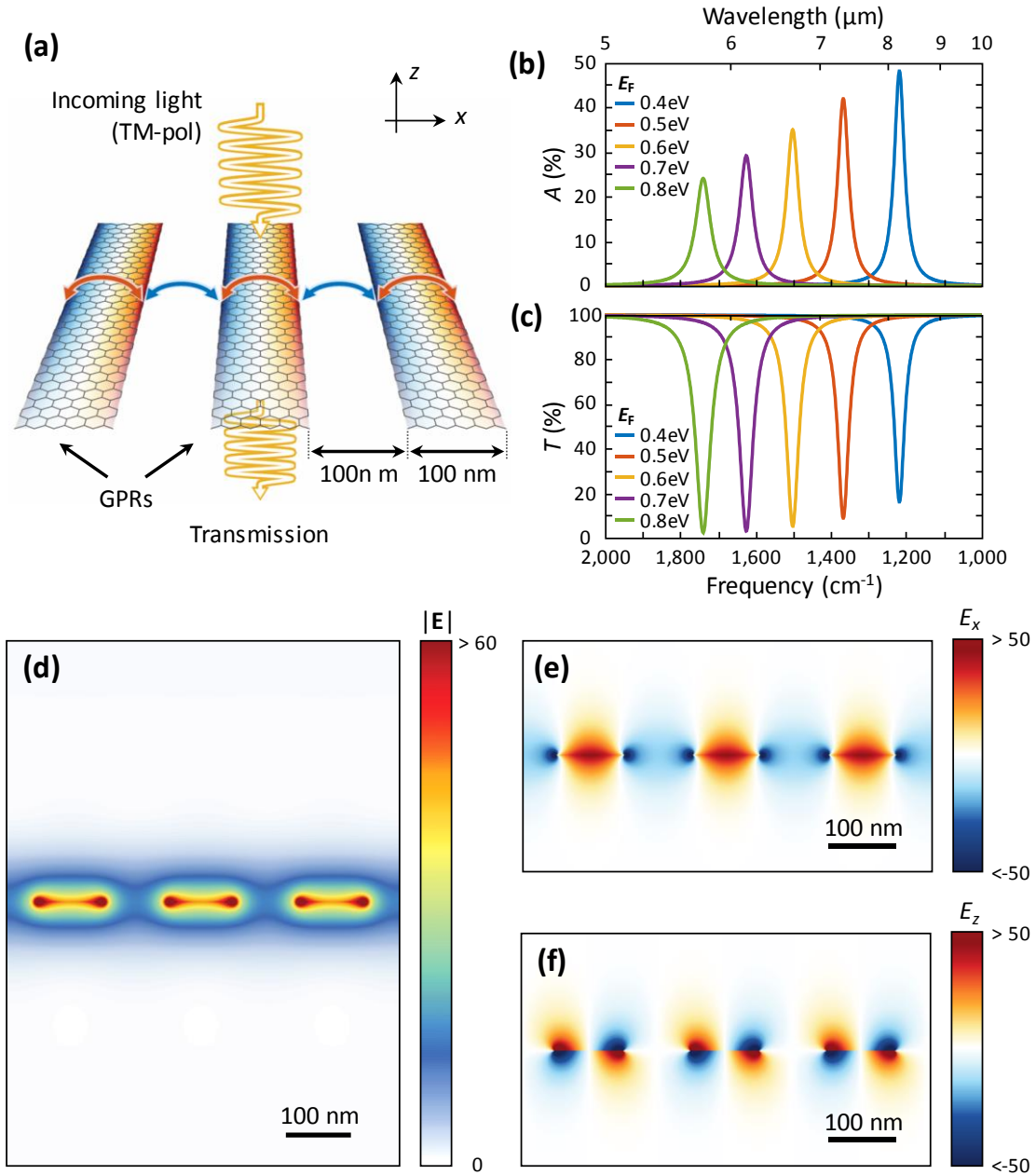


Figure 1.8 | Light modulation in graphene plasmonic ribbons. (a) Schematic of GPRs surrounded by air for tunable light modulation. The red and the blue arrows denote graphene plasmons and interaction between adjacent GPRs, respectively. The overlapped distributions represent the charge distribution in graphene (red: holes, blue: electrons) (b) Simulation results of absorption spectra and (c) transmission spectra depending on different graphene Fermi level (E_F). (d) Electric field, (e) E_x , and (f) E_z field distributions representing graphene plasmons at free-space wavelength $\lambda_0=6.66 \mu\text{m}$ with graphene Fermi level $E_F=0.6 \text{ eV}$.

1.3 Scope of this Thesis

In this thesis, we present how to electronically tune the plasmonic resonance in graphene. Using the tunable property of graphene plasmon, we devise electronically tunable light modulators using graphene plasmon in mid-infrared range. In addition to the tunable graphene plasmonic resonance properties, we also demonstrate that the graphene plasmonic resonance can be enhanced when we couple the graphene plasmonic light modulators with noble metal plasmonic structures, which results in increasing light modulation efficiency.

To begin with, we will review the details on the tunable graphene plasmons and strong light absorption in graphene plasmonic ribbons. In addition, we will show how to grow large scale graphene by chemical vapor deposition (CVD), and how to transfer and characterize the CVD graphene. Then, we will present three kinds of electronically tunable light modulators based on graphene plasmonic ribbons coupled to noble metal plasmonic structures.

1.3.1 Electronically Tunable Resonant Absorption in Graphene Plasmonic Metasurface Enhanced by Noble Metal Plasmonic Effect

In the first light modulator, we propose and demonstrate electronically tunable resonant absorption in graphene plasmonic metasurface enhanced by noble metal plasmonic effect, which results in modulating reflecting light. The ultimate purpose of this devices is to achieve strong graphene plasmonic resonance even with low quality graphene, such as CVD graphene.

Theoretical calculations predict perfect absorption in the proposed graphene plasmonic metasurface despite a low graphene carrier mobility ($200 \text{ cm}^2\text{V}^{-1}\text{s}^{-1}$) at a graphene Fermi level easily accessible with electrostatic gating. We present a rigorous analytic model based on effective surface admittance to elucidate the origin of the enhanced absorption, which shows that the perfect absorption corresponds to a critical coupling between the graphene plasmonic metasurface and the carefully controlled substrate.

Experimental measurements reveal 96.9% absorption in the graphene plasmonic metasurface at $1,389 \text{ cm}^{-1}$, corresponding to a modulation efficiency of 95.9% in reflection, corresponding to a 2.15 fold improvement in the modulation efficiency over reflection without the coupled subwavelength metal slits.

1.3.2 Electronically Tunable Extraordinary Optical Transmission in Graphene Plasmonic Ribbons Coupled to Subwavelength Metallic Slit Arrays

In the second device, we present how to efficiently modulate transmitting light using graphene plasmonic ribbons. In contrast to the reflective type graphene plasmonic modulators, a strategy of using electrostatically tunable graphene plasmons to modulate transmitted light with near-unity efficiency has not yet been reported. In order to enhance the graphene plasmonic resonance in a transmission type light modulator, we couple the graphene plasmonic ribbons to subwavelength metal slit array exhibiting extraordinary optical transmission in mid-infrared.

In this structure, extraordinary optical transmission resonance in subwavelength metal slit array is coupled to electrostatically tunable graphene plasmonic resonance in graphene plasmonic ribbons to create electrostatic modulation of mid-infrared light. Absorption in graphene plasmonic ribbons situated inside metallic slits can efficiently block the coupling channel for resonant transmission, leading to a suppression of transmission. We also present anti-crossing model to analyze the light modulation effect between the extraordinary optical transmission resonance and the graphene plasmonic resonance.

Full wave simulations predict a transmission modulation of 95.7% via this mechanism. Experimental measurements reveal a modulation efficiency of 28.6% in transmission at $1,397\text{ cm}^{-1}$, corresponding to a 2.67 fold improvement over transmission without a metallic slit array.

1.3.3 Electronically Tunable Graphene Plasmonic Resonance Energy Transport

Finally, we report electronically tunable graphene plasmonic resonance energy transport along graphene plasmonic ribbons, and we devise a platform to demonstrate the energy transport in mid-infrared. In this structure, two metal-insulator-metal plasmonic waveguides are connected by a subwavelength metal slit, and graphene plasmonic ribbons are located inside this slit. Due to the large impedance mismatch between the noble metal plasmonic waveguide and the subwavelength metal slit, light coupling efficiency across the junction is poor.

If the graphene plasmonic ribbons inside the slit are tuned to support strong graphene plasmonic resonances, this generates another pathway for transporting light energy across the junction. As a result, the light transmission across the subwavelength metal slit is enhanced significantly compared to a bare slit without the graphene plasmonic resonance energy transport.

In order to electronically modulate the transmission in the noble metal plasmonic waveguide using the graphene plasmonic resonance energy transport, we also have to actively suppress the light energy transport across the junction. To achieve this, we engineer the junction geometry in order to induce a strong Fano resonance between a non-resonant propagation mode across the junction and a resonant transmission mode via the graphene plasmonic resonance energy transport. Theoretical calculations predict a 100% light modulation efficiency with moderate graphene carrier mobility ($1,660 \text{ cm}^2\text{V}^{-1}\text{s}^{-1}$) at a graphene Fermi level easily accessible with electrostatic gating. The maximum resonant transmission in the plasmonic waveguide across the junction is 43.4%, while the transmission is 14.2% without the graphene plasmonic resonance energy transport.

CHAPTER 2

GRAPHENE PLASMONS AND CHEMICAL VAPOR DEPOSITION GROWN GRAPHENE

In this chapter, we will review the details on dispersion relation of tunable graphene plasmons in mid-infrared and how to enhance electronically tunable light modulation efficiency in graphene plasmonic ribbons (GPRs) by intensifying light-matter interaction in the GPRs. Then, we will present large scale graphene growth using the chemical vapor deposition (CVD) method and a method to transfer the CVD-grown graphene onto arbitrary substrates. To characterize the CVD-grown graphene, we will briefly explain Raman spectroscopy and transport measurement in graphene.

2.1 Graphene Plasmons

As shown in Chapter 1, the graphene plasmonic ribbons exhibit higher confinement factor and stronger near field enhancement compared to the noble metal plasmonic antennas. It is also possible to adjust the carrier density in graphene by doping the graphene via external gate bias, and it allows us to electronically tune the graphene plasmonic resonance. In addition, it has been demonstrated that graphene plasmons exhibit a lifetime in the order of femtosecond or sub-picosecond timescales [51, 52]. It indicates that we can realize ultrafast optical switching using graphene plasmons.

Graphene can support transverse magnetic (TM) and transverse electric (TE) modes. Similar to the surface plasmons on noble metal surface, TM graphene modes are electric dipole waves coupled to free carriers in graphene. In contrast, TE graphene plasmon modes, which are not observable on noble metal surface, correspond to magnetic dipole waves with no spatial charge density perturbation, and the TE graphene plasmon modes exhibit the propagating speed close to the light speed in surrounding media [53-55], and thus show a weak damping but less confinement factors than TM graphene plasmon modes. To take advantage of high confinement factors and strong graphene plasmonic resonances, this thesis will be limited to consideration of the TM graphene plasmon modes.

In this section, we will present tunable dispersion relation of graphene plasmons in a graphene plasmonic waveguide, and the properties of graphene plasmons will be compared with

noble metal plasmons in an insulator-metal-insulator (IMI) waveguide. Then, the strong light absorption in graphene plasmonic ribbons will be discussed for tunable light modulation. At the end of this section, we will explain how to model the graphene in full-wave electromagnetic simulations.

2.1.1 Dispersion Relation of Graphene Plasmons

Figure 2.1(a) shows the schematic of TM graphene plasmon propagating along graphene, and its dispersion relation [45, 56, 57] is given by

$$\frac{\varepsilon_{r1}}{\sqrt{k_p(\omega)^2 - \varepsilon_{r1}\omega^2/c_0^2}} + \frac{\varepsilon_{r2}}{\sqrt{k_p(\omega)^2 - \varepsilon_{r2}\omega^2/c_0^2}} = -i \frac{\sigma(\omega)}{\omega\varepsilon_0} \quad (2.1)$$

where ε_{r1} and ε_{r2} are the relative permittivities of surrounding media above and below the graphene, respectively, and $\sigma(\omega)$ is the frequency dependent surface conductivity of graphene neglecting spatial dispersion. When we use a semi-classical Drude-like expression for the surface conductivity of graphene given by Eq. (2.2), the dispersion relation of graphene plasmon in a quasi-static regime ($k_p \gg \omega/c_0$) is expressed by Eq. (2.3) [45].

$$\sigma(\omega) \approx i \frac{e^2 |E_F|}{\pi \hbar^2 (\omega + i\tau^{-1})} \quad (2.2)$$

$$k_p(\omega) \approx \frac{\pi \hbar^2 \varepsilon_0 (\varepsilon_{r1} + \varepsilon_{r2})}{e^2 |E_F|} \left(1 + \frac{i}{\tau\omega} \right) \omega^2 \quad (2.3)$$

In Eqs. (2.2-3), E_F is the graphene Fermi level and τ is the intrinsic relaxation time constant induced by impurities, defects, or scattering processes. This intrinsic relaxation time constant determines the graphene carrier mobility, and the graphene carrier mobility represents the quality of graphene. More rigorous expression for the surface conductivity of graphene will be presented in Section 2.1.3, and the graphene plasmonic resonance depending on the graphene carrier mobility will be discussed in Section 2.1.4.

The graphene plasmon shown in Fig. 2.1(a) resembles the E_x -symmetric (or H_y -antisymmetric) plasmonic mode in an IMI waveguide [28, 58] shown in Fig. 2.2(a) in that electromagnetic waves propagating along the surfaces are highly confined in the graphene or the thin metal layer, the electromagnetic waves exponentially decay along the perpendicular directions. However, the most distinctive difference is that the graphene plasmon dispersion relation in Eq. (2.3) indicates that the dispersion relation is tunable by adjusting the graphene Fermi level, i.e.

doping graphene, as shown Fig. 2.1(b). Notably, the graphene plasmon dispersion relation implies that the graphene plasmonic resonance frequency is proportional to the graphene Fermi level.

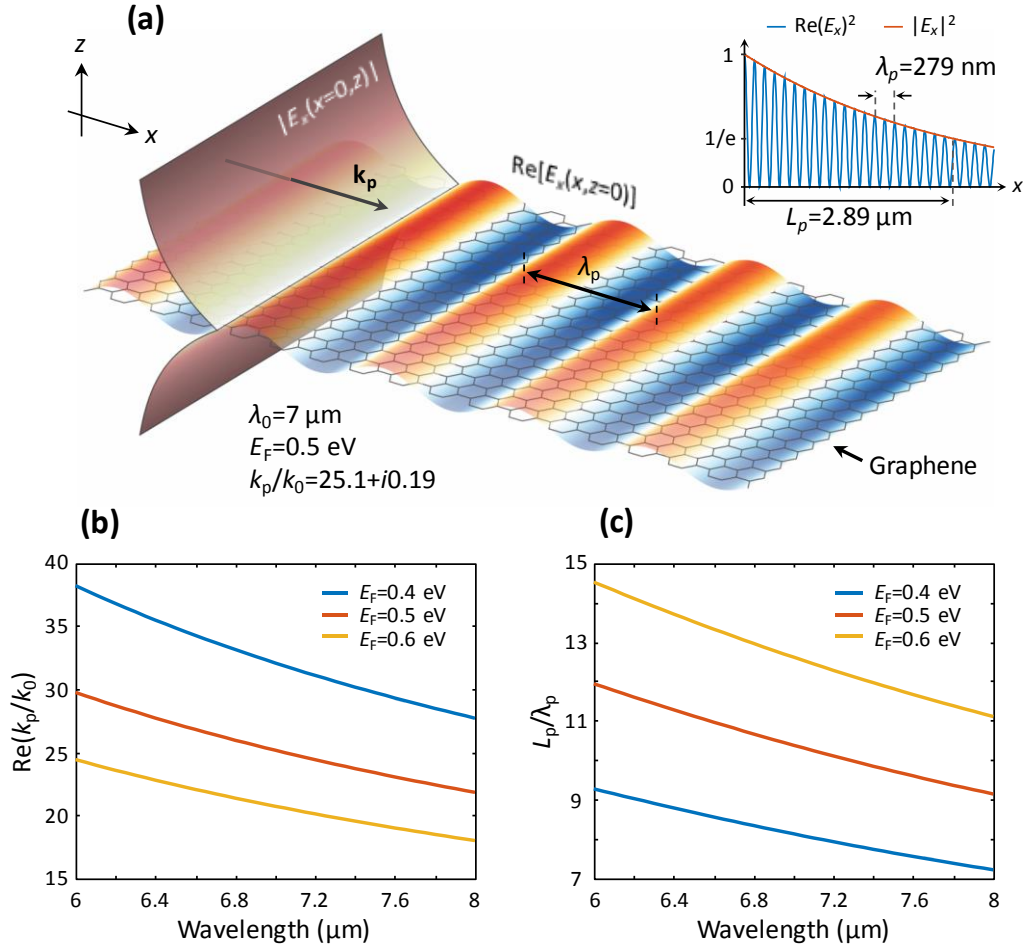


Figure 2.1 | Graphene plasmonic waveguide. (a) Schematic of graphene plasmonic waveguide surrounded by air. The graphene carrier mobility is assumed as $10,000 \text{ cm}^2\text{V}^{-1}\text{s}^{-1}$. (b) Real part of graphene plasmon wavenumber (k_p) normalized by free-space wavenumber (k_0) with different graphene Fermi level (E_F). (c) Graphene plasmon propagation length (L_p) over graphene plasmon wavelength (λ_p) with different graphene Fermi level.

In addition to the tunable dispersion relation, the graphene plasmon exhibit significantly high confinement factor compared to the IMI plasmonic mode shown in Fig. 2.2. With $E_F=0.5 \text{ eV}$, light having $7 \text{ }\mu\text{m}$ of free-space wavelength (λ_0) is coupled to graphene plasmon with 279 nm of graphene plasmon wavelength (λ_p), and it corresponds to 25.1 of $\text{Re}(k_p/k_0)$. However, the IMI plasmonic mode exhibits only 1.95 of $\text{Re}(k_p/k_0)$ with $\lambda_0=532 \text{ nm}$ and $\lambda_p=273 \text{ nm}$.

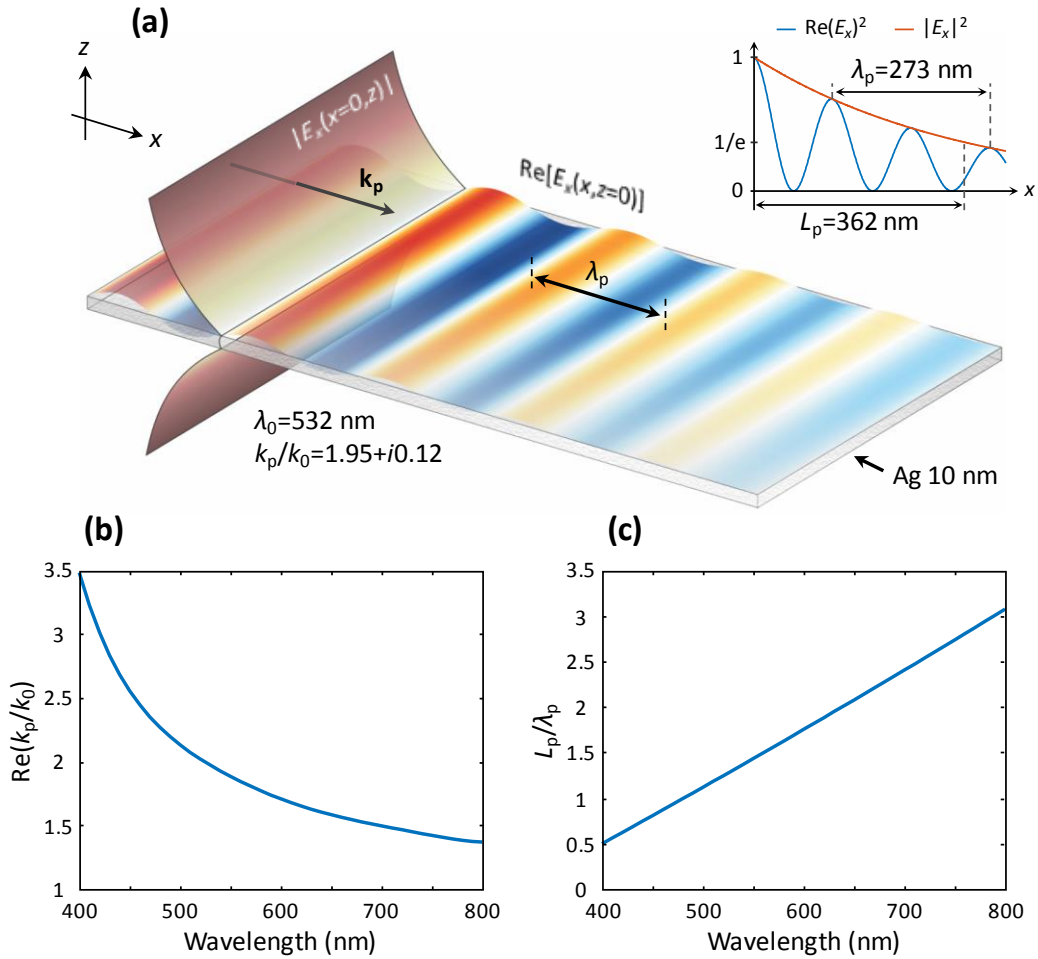


Figure 2.2 | Insulator-metal-insulator plasmonic waveguide. (a) Schematic of E_x -symmetric (or H_y -antisymmetric) IMI plasmonic waveguide with 10 nm thick Ag surrounded by air. (b) Real part of plasmon wavenumber (k_p) normalized by free-space wavenumber (k_0). (c) Plasmon propagation length (L_p) over plasmon wavelength (λ_p).

Moreover, the graphene plasmon has lower loss than the plasmon in the IMI waveguide, as shown in Figs. 2.1(c) and 2.2(c), although the graphene plasmon shows a higher confinement factor. In Fig. 2.1(a), the propagation length of the graphene plasmon (L_P) is $2.89 \mu\text{m}$, and it indicates that the graphene plasmon can propagate 10.4 times longer distance than its wavelength. However, the propagation length over the plasmon wavelength in Fig. 2.2(a) exhibits only 1.33 with $L_p = 362$ nm.

As discussed in this section, the graphene plasmon has tunable dispersion relation depending on the graphene Fermi level, and the graphene plasmon exhibits lower loss and higher confinement factor than the noble metal plasmon.

2.1.2 Perfect Absorption in Graphene Plasmonic Ribbons

As shown in Chapter 1, we can tune light absorption in graphene plasmonic ribbons (GPRs) by adjusting the graphene Fermi level. In particular, it has been theoretically demonstrated that perfect absorption is achievable if we increase the light-matter interactions in the GPRs with Salisbury screen [59], and nearly 40% of electronically tunable absorption in the GPRs has been demonstrated experimentally [60].

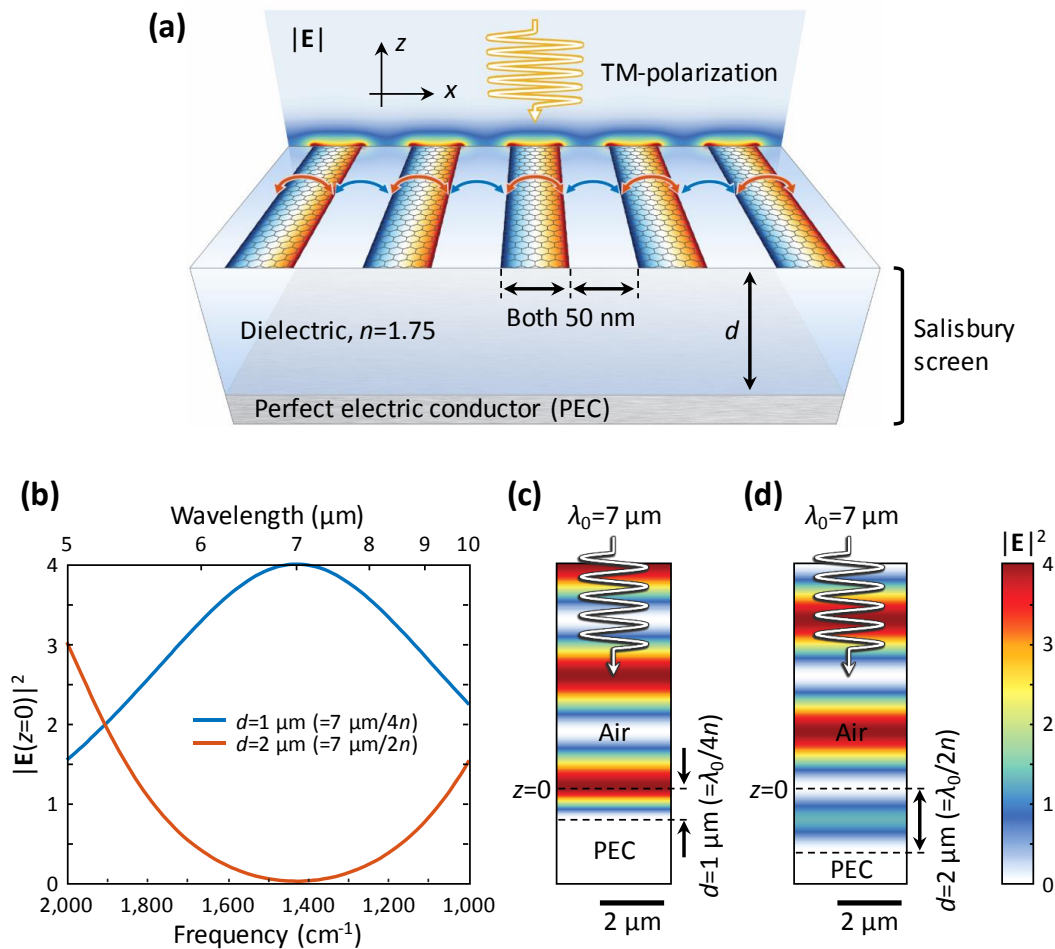


Figure 2.3 | Graphene plasmonic ribbons on Salisbury screen. (a) Schematic of GPRs on Salisbury screen consisting of a dielectric layer ($n=1.75$) and a perfect electric conductor reflector. (b) Electric intensity on the air/dielectric interface depending on frequency with different dielectric layer thickness. Electric intensity distributions (c) with maximum constructive interference and (d) maximum destructive interference on the air/dielectric interface.

Figure 2.3(a) shows the schematic of GPRs-based mid-infrared light modulator with Salisbury screen. The GPRs' width/gap are assumed as 50 nm/50 nm, and 1.01 μm thick dielectric layer with $n=1.75$ with perfect electric conductor reflector constitute the Salisbury screen.

Salisbury screen was invented during World War II in order to reduce radar cross section for stealthy operation [61]. The principle of the Salisbury screen is that incoming light and outgoing light reflected from a back reflector interfere, maximum constructive interference occurs at quarter wavelength position above the back reflector because light undergoes π -phase shift when it is reflected by the back reflector, as shown in Figs. 2.3(b) and (c). In the same manner, the electric field is minimized at the air/dielectric interface if the interface is located at the half wavelength position because of the destructive interference between the incoming light and the reflected light from the perfect electric conductor reflector, as shown in Figs. 2.3(b) and (d). Therefore, we can significantly enhance the absorption if absorbing materials are positioned at this quarter wavelength position due to the intensified electric field induced by the Salisbury screen resonance leading to strong light-matter interaction. In this device, we design the Salisbury screen exhibiting maximized electric field at the air/dielectric ($n=1.75$) interface with free-space wavelength $\lambda_0=7 \mu\text{m}$, corresponding to 1 μm thick dielectric layer. Then, the GPRs are located at the air/dielectric interface in order to enhance the absorption in the GPRs, which results in high modulation efficiency in reflection.

Figures 2.4(a) and (b) show the gate-dependent tunable reflection and absorption and in the GPRs on the Salisbury screen. As mentioned in Section 2.1.1, the graphene plasmon dispersion relation is tunable by adjusting the graphene Fermi level. In Eq. (2.3), we can derive that the graphene plasmonic resonance frequency is approximately proportional to the square root of the graphene Fermi level. Therefore, the graphene plasmonic resonance peaks in the GPRs exhibit blue-shift as increasing the graphene Fermi level.

In general, we can induce stronger graphene plasmonic resonance with higher graphene Fermi level because there are more free carriers interacting with graphene plasmons. Suppose that the geometry of the GPRs is fixed, it indicates that stronger absorption occurs at higher frequency due to the relation between the resonance frequency and the graphene Fermi level. However, the perfect absorption is achieved when the graphene plasmonic resonance frequency matches the quarter wavelength condition of the Salisbury screen, as shown in Figs. 2.4(a) and (b), and the absorption decrease at higher frequency (or higher graphene Fermi level). This is the result of the enhanced electric fields around the GPRs by the maximized constructive interference from the Salisbury screen.

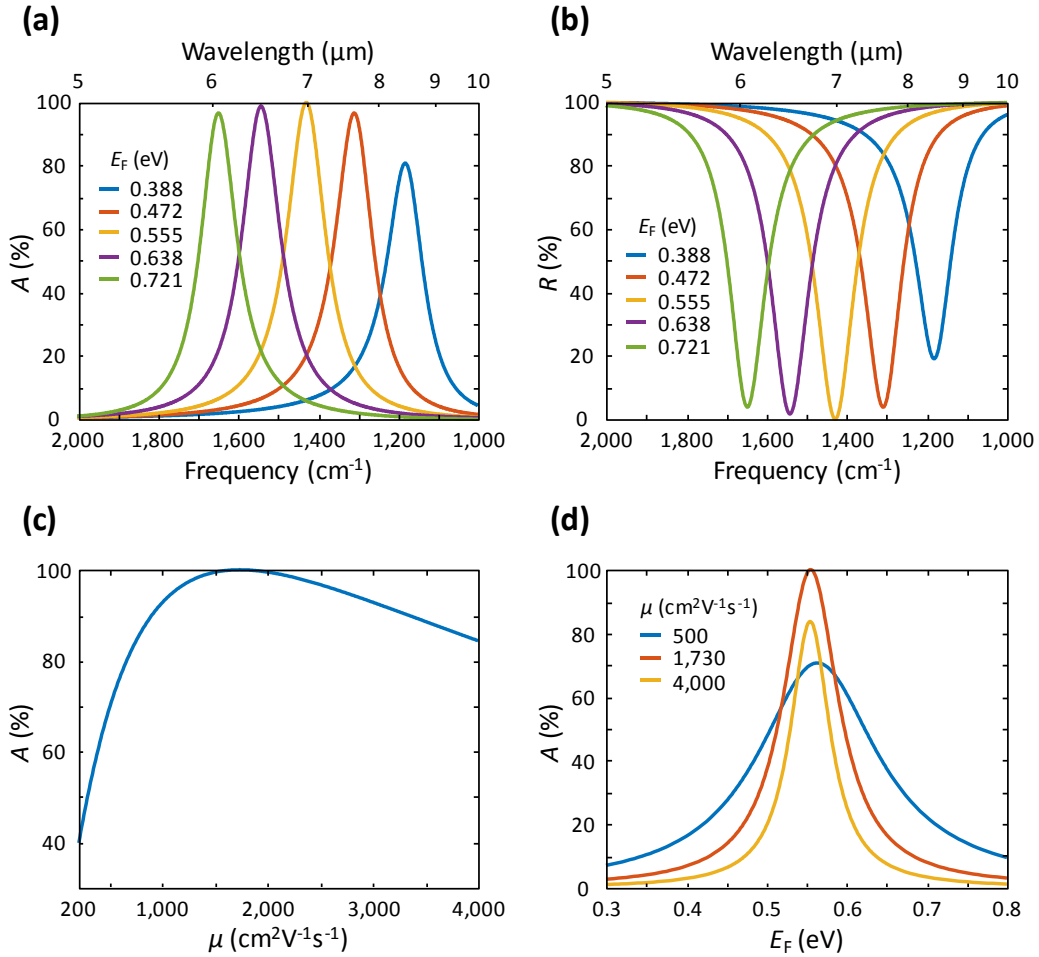


Figure 2.4 | Perfect absorption in graphene plasmonic ribbons. Gate-dependent (a) absorption spectra and (b) reflection spectra from the GPRs on Salisbury screen. (c) Absorption depending on the graphene carrier mobility (μ). (d) Absorption depending on the graphene Fermi level (E_F) with different graphene carrier mobility (μ).

In the GPRs-based light modulation, graphene carrier mobility is an important factor to determine the light modulation efficiency. The graphene carrier mobility indicates the carrier scattering in the graphene, and it represents the graphene quality [62]. Therefore, the degree of the graphene plasmonic resonance is limited by the graphene carrier mobility. With high graphene carrier mobility, or high quality graphene, we can induce strong graphene plasmonic resonance having high Q-factor in the graphene plasmonic resonators. However, low graphene carrier mobility weakens the graphene plasmonic resonance resulting in reducing Q-factor in the graphene plasmonic resonators. Figure 2.4 (c) shows the absorption depending on the graphene carrier mobility. The perfect absorption occurs with graphene carrier mobility $\mu=1,730 \text{ cm}^2\text{V}^{-1}\text{s}^{-1}$, and the absorption decreases with lower graphene carrier mobility because of lower graphene plasmonic

resonance. Above graphene carrier mobility $\mu=1,730 \text{ cm}^2\text{V}^{-1}\text{s}^{-1}$, the absorption also decrease as increasing the graphene carrier mobility, as shown in Figs. 2.4(c) and (d). This is not because the graphene plasmonic resonance is reduced with higher graphene carrier mobility, but because the condition of graphene carrier mobility $\mu>1,730 \text{ cm}^2\text{V}^{-1}\text{s}^{-1}$ corresponds to over-coupling between the graphene plasmonic resonance and the Salisbury screen resonance. The details on the absorption depending on the graphene carrier mobility will be discussed in Chapter 3.

2.1.3 Modeling Graphene in Electromagnetics

To calculate the optical response of graphene in electromagnetics, we first have to derive the dynamical optical surface conductivity of the graphene. In the local limit of random phase approximation neglecting the spatial dispersion, the frequency dependent optical conductivity of graphene is given by [63-65]

$$\begin{aligned} \sigma(\omega) &= \sigma_{\text{intra}}(\omega) + \sigma_{\text{inter}}(\omega) \\ &= \frac{e^2\omega}{i\pi} \left[\int_{-\infty}^{\infty} dE \frac{|E|}{(\hbar\omega)^2} \cdot \frac{df_d(E)}{dE} - \int_0^{\infty} dE \frac{f_d(-E) - f_d(E)}{(\hbar\omega)^2 - 4E^2} \right] \end{aligned} \quad (2.4)$$

where $\sigma_{\text{intra}}(\omega)$ and $\sigma_{\text{inter}}(\omega)$ are the conductivities originating from the intraband and the interband transitions in graphene, respectively. And $f_d(E) = \frac{1}{1+\exp[(E-E_F)/k_B T]}$ is the Fermi-Dirac distribution function with graphene Fermi level E_F . If there are impurities, defects, or disorders in graphene, it creates electron-electron scattering, and it results in reducing the graphene carrier mobility. In order to consider this electron disorder scattering process, the frequency ω is replaced with $\omega+i\tau^{-1}$, where τ is the intrinsic relaxation time. The intrinsic relaxation time τ is given by

$$\tau = \frac{\mu|E_F|}{ev_F^2} \quad (2.5)$$

where μ is the graphene carrier mobility, E_F is the graphene Fermi level, e is the elementary charge, and v_F is the Fermi velocity in graphene. With this intrinsic relaxation time, the $\sigma_{\text{intra}}(\omega)$ and $\sigma_{\text{inter}}(\omega)$ are simplified by

$$\sigma_{\text{intra}}(\omega) = \frac{i2e^2k_B T}{\pi\hbar^2(\omega + i\tau^{-1})} \log \left[2 \cosh \left(\frac{|E_F|}{2k_B T} \right) \right] \quad (2.6)$$

$$\sigma_{\text{inter}}(\omega) = \frac{e^2}{4\hbar} G \left(\frac{\hbar\omega}{2} \right) + \frac{ie^2\omega}{\pi} \int_0^{\infty} dE \frac{G(E) - G \left(\frac{\hbar\omega}{2} \right)}{(\hbar\omega)^2 - (2E)^2} \quad (2.7)$$

where $G(E) = \frac{\sinh(E/k_{\text{B}}T)}{\cosh(E/k_{\text{B}}T) + \cosh(|E_{\text{F}}|/k_{\text{B}}T)}$. Figure 2.5 shows the real part and the imaginary part of the frequency dependent optical surface conductivity of graphene normalized by e^2/\hbar with $E_{\text{F}}=0.3$ eV and graphene carrier mobility $\mu=10,000$ $\text{cm}^2\text{V}^{-1}\text{s}^{-1}$ at room temperature ($T=300$ K). As shown in Fig. 2.5(a), the real part of the graphene optical surface conductivity is dominated by the $\sigma_{\text{inter}}(\omega)$ because of the interband transition absorption.

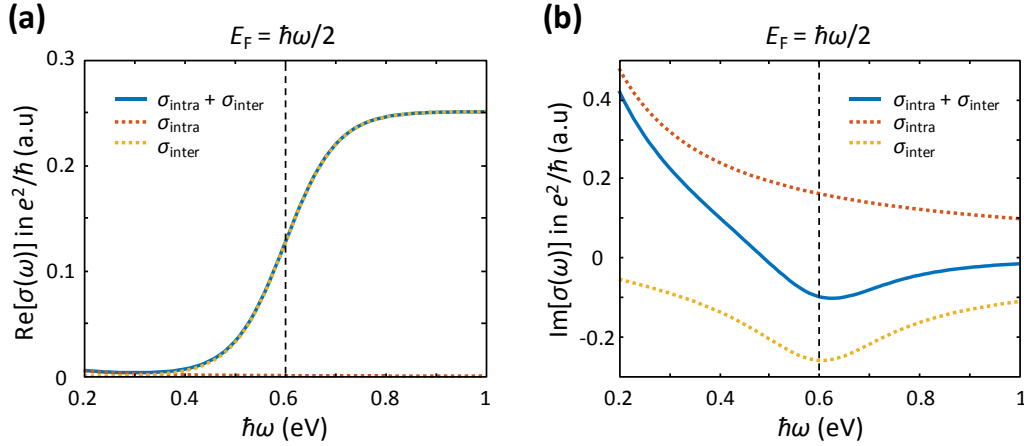


Figure 2.5 | Graphene optical surface conductivity. (a) Real part and (b) imaginary part of frequency dependent optical surface conductivity of graphene with $E_{\text{F}}=0.3$ eV and $\mu=10,000$ $\text{cm}^2\text{V}^{-1}\text{s}^{-1}$ at room temperature ($T=300$ K).

In full-wave electromagnetic simulations, there are two ways to model the atomically thin monolayer graphene. First, we can model the graphene with surface current $\mathbf{J}_{\parallel} = \sigma \mathbf{E}_{\parallel}$, where the subscript \parallel denotes the parallel component to graphene surface. Second, the graphene can be modeled by a very thin layer with frequency dependent permittivity given by [59, 63, 64]

$$\varepsilon(\omega) = 1 + \frac{i\sigma(\omega)}{\varepsilon_0\omega d_{\text{g}}} \quad (2.8)$$

where d_{g} is the graphene thickness. Figure 2.6(a) shows the permittivity of graphene with $d_{\text{g}}=0.1$ nm depending on the graphene Fermi level at $\hbar\omega=0.5$ eV with graphene carrier mobility $\mu=10,000$ $\text{cm}^2\text{V}^{-1}\text{s}^{-1}$. If the graphene thickness d_{g} is chosen below 0.5 nm, the difference between the surface current modeling and the thin layer modeling is negligible in mid-infrared range, as shown in Fig. 2.6(b).

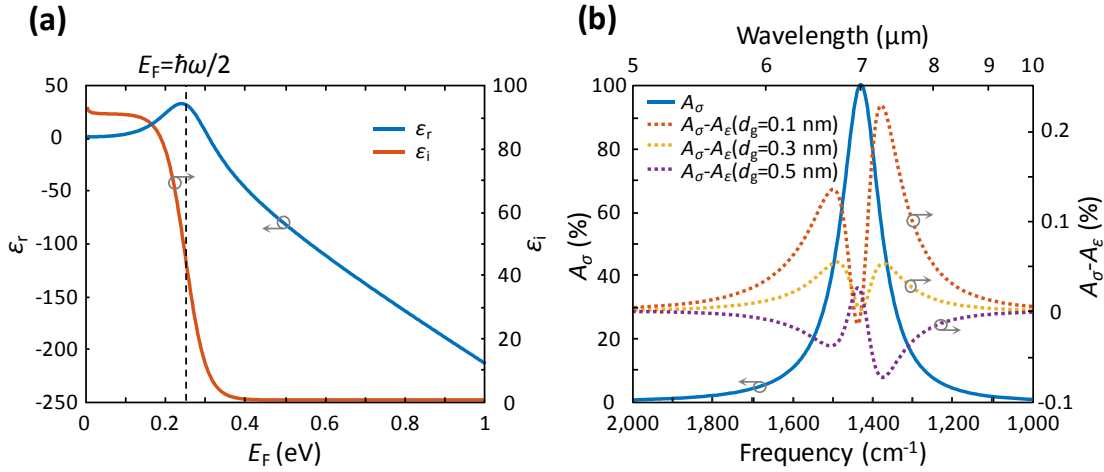


Figure 2.6 | Graphene dielectric function. (a) Relative permittivity of graphene modeled by 0.1 nm thick layer depending on the graphene Fermi level (E_F) with photon energy $\hbar\omega=0.5$ eV and graphene carrier mobility $\mu=10,000$ $\text{cm}^2\text{V}^{-1}\text{s}^{-1}$. (b) Absorption comparison between the surface current modeling (A_σ) and relative permittivity with thin layer (A_ϵ) for modeling graphene of the GPR structure in Fig. 2.3. The graphene Fermi levels (E_F) for the A_σ and A_ϵ with $d_g=0.1$ nm, 0.3 nm, and 0.5 nm are chosen by 0.555 eV, 0.552 eV, 0.556 eV, and 0.560 eV, respectively.

2.2 Chemical Vapor Deposition Grown Graphene

Monolayer graphene can be grown by chemical vapor deposition (CVD) method, and the size of the CVD-grown graphene is scalable [66-69]. In 2010, 30-inch monolayer graphene for transparent electrodes has been demonstrated [70]. In addition, it allows us to transfer the monolayer graphene onto arbitrary substrates [71]. These two advantages of the CVD-grown graphene is very important in device fabrication. When it comes to the graphene quality, exfoliated graphene has higher graphene carrier mobility than CVD-grown graphene [72, 73]. However, it has been demonstrated that the graphene carrier mobility of CVD-grown graphene can be as good as the exfoliated graphene by growing millimeter size single crystal graphene [74-77].

2.2.1 Graphene Growth in Chemical Vapor Deposition Method

Figure 2.7 shows the schematic of graphene growth in a CVD method. Copper foil (Alfa Aesar, 0.025 mm thick, purity=99.999%) is placed in a tube furnace, and the tube is pumped by a roughing pump. As heating the tube, we flow CH_4 and H_2 gases. Here, the CH_4 gas supplies the carbon source for graphene growth, and the H_2 gas corresponds to a purging gas.

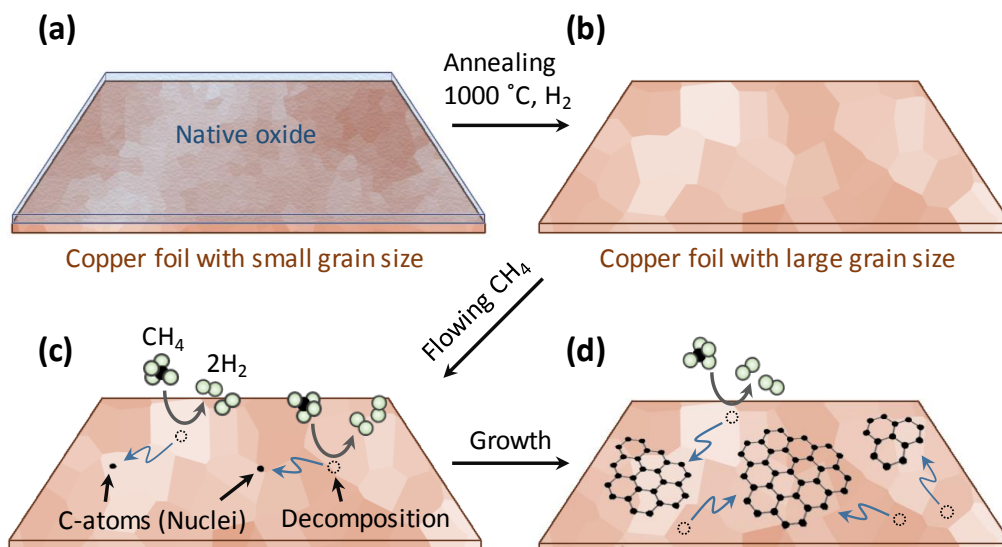


Figure 2.7 | Graphene growth in chemical vapor deposition method. (a) Pristine copper foil with small grain size and a native oxide layer. (b) Annealed copper foil with large crystalline grain size. The native oxide layer is removed during the annealing process. (c) CH₄ decomposition on the copper foil and nucleation of carbon atoms. (d) Graphene growth with further CH₄ decomposition.

Before flowing CH₄ gas, we first have to anneal the copper foil at 1,000 °C for an hour with H₂ in order to remove the native oxide layer. In addition, the annealing process reduces the defects in the pristine copper foil and increases the copper grain size, as shown in Figs. 2.7(a) and (b). When we start flowing CH₄ gas, the copper foil acts as catalyst to decompose the CH₄ gas at high temperature, and the decomposition occurs randomly on arbitrary positions on the copper foil surface. Since copper has nearly zero affinity to carbon [68], the decomposed carbon atoms cannot diffuse into the copper foil, and they wander on the copper foil surface. As wandering on the copper foil surface, the decomposed carbon atoms are trapped by defects on the copper foil, as shown in Fig. 2.7(c). The trapped carbon atoms perform as nuclei for graphene growth, and further CH₄ decomposition leads to deposition of graphene islands, as shown in Fig. 2.7(d). In this process, each graphene island expands to different lattice orientation, and coalesced graphene layer becomes polycrystalline. When the graphene layer covers the copper foil surface, it prevents further CH₄ decomposition because the covered graphene layer acts as an inert blanket. After flowing CH₄ gas for an hour at 1,000 °C, we can grow a continuous monolayer polycrystalline graphene layer on the copper foil.

Figure 2.8 compares the size of the exfoliated graphene and the CVD-grown graphene on SiO₂/Si substrate. As shown in Fig. 2.8, the size of the exfoliated graphene is not compared to the

CVD-grown graphene, and the CVD-grown graphene displays continuous coverage on a very large scale.

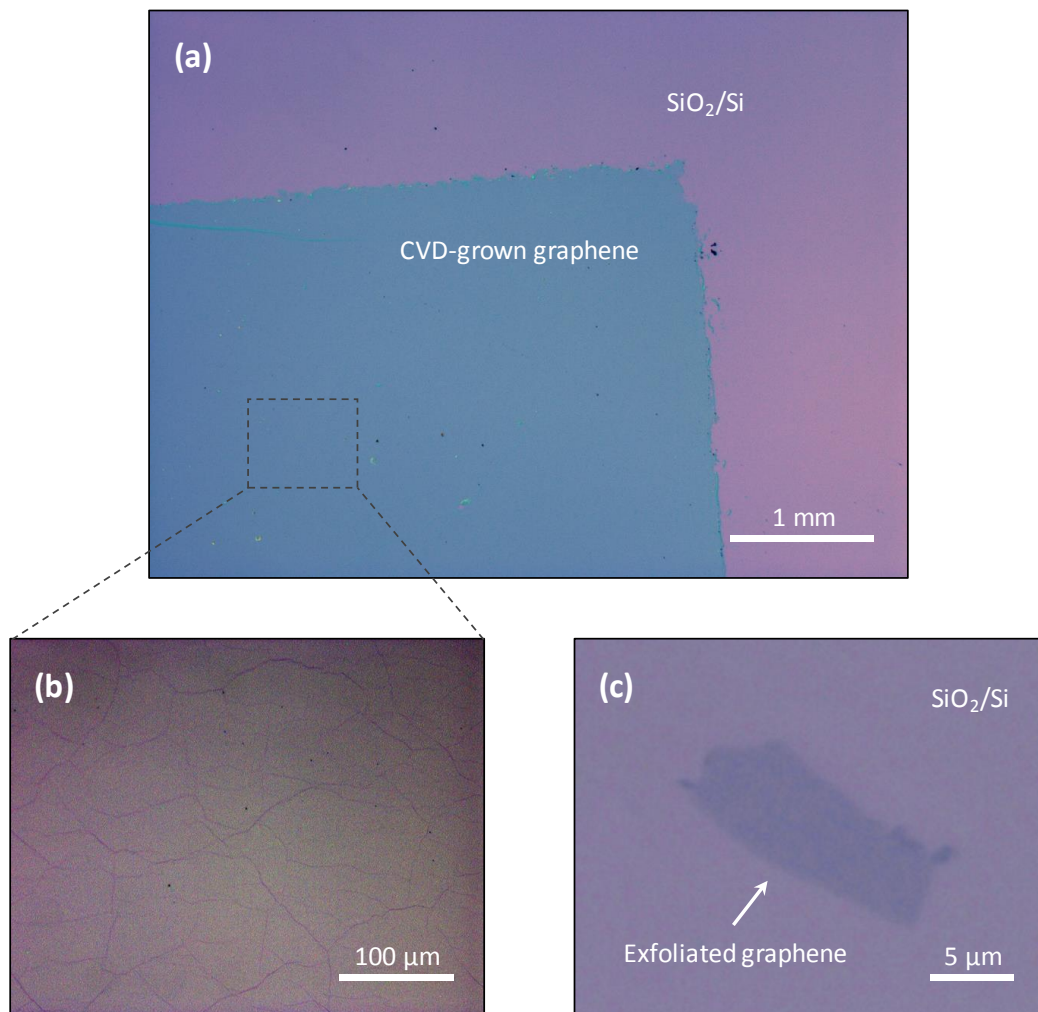


Figure 2.8 | Graphene images. Optical microscope images of CVD-grown graphene on SiO₂/Si substrate (a) with a large field of view and (b) with a small field of view. (c) Optical microscope images of exfoliated graphene on SiO₂/Si substrate.

There are critical parameters determining graphene quality [78]. First of all, the growth temperature is the most important parameters. High temperature near to copper melting temperature is required to anneal the copper foil as well as to decompose the CH₄ gas. If the annealing and the growth temperature is too low, it leads to uncontrollable multilayer graphene growth, as shown in Fig. 2.9(a). We expect that the enough high temperature reduces the pristine defects in the copper foil, and it would lead to more conformal graphene growth. We cannot grow the graphene at too

high temperature because the copper foil is evaporated even below its melting temperature (1,085 °C). In our graphene growth CVD system, the optimized temperature is 1,000 °C.

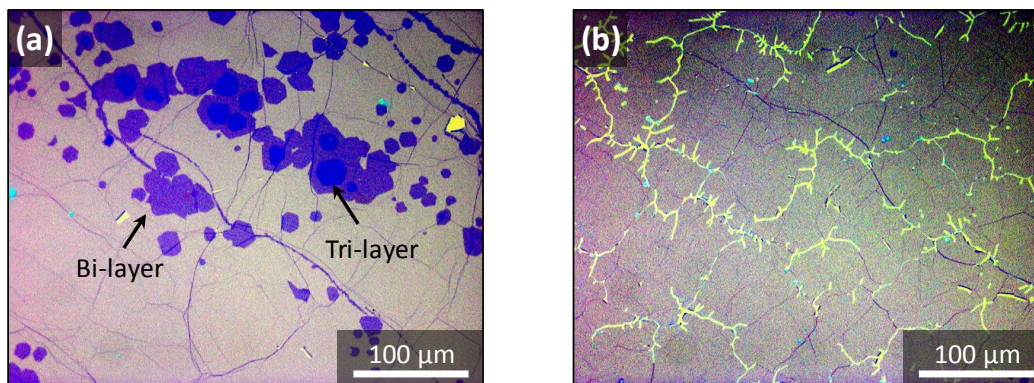


Figure 2.9 | Defective graphene growth. (a) CVD-grown Graphene with multi-layers. (b) Incompletely grown graphene.

The gas flow rate is also very important to grow graphene [77, 79, 80]. In order to grow high quality graphene, we have to reduce both the density of the carbon atom nuclei because it leads to larger crystalline graphene domain size. In addition, we also have to slow down the graphene growth rate in order to secure enough time to make appropriate carbon-carbon bonding. These two conditions are achievable by decreasing the CH_4 gas flow rate and by increasing the H_2 purging gas flow rate because it reduces the ratio of carbon source. However, the graphene would be incompletely grown if the CH_4 gas rate is too small, as shown in Fig. 2.9(b). In our graphene growth CVD system, the 1 sccm of CH_4 gas flow rate and the 50 sccm of H_2 gas flow show the best quality of graphene.

2.2.2 Graphene Transfer

After growing a monolayer graphene on a copper foil using a CVD method, we can transfer the graphene onto arbitrary substrate. The procedure is shown in Figure. 2.10. To begin with, PMMA layer (MicroChem, 495 A4) is spin coated on the graphene/copper foil to support the graphene layer on etchant or DI water. About 200nm of PMMA is coated on the graphene with 2,500 RPM for a minute spin-coating. To support the graphene layer, PDMS and polymeric tapes can be also used instead of PMMA [68]. However, PMMA spin-coating is most common because it induces less cracks during transferring process and it is easier to remove the PMMA without damaging the graphene than the PDMS or the polymeric taps. After baking the

PMMA/graphene/copper foil stack, the graphene grown on the backside of the copper foil is etched in a plasma asher with O_2 at 100 W of power for a minute. In this process, the top graphene layer is protected by the PMMA layer.

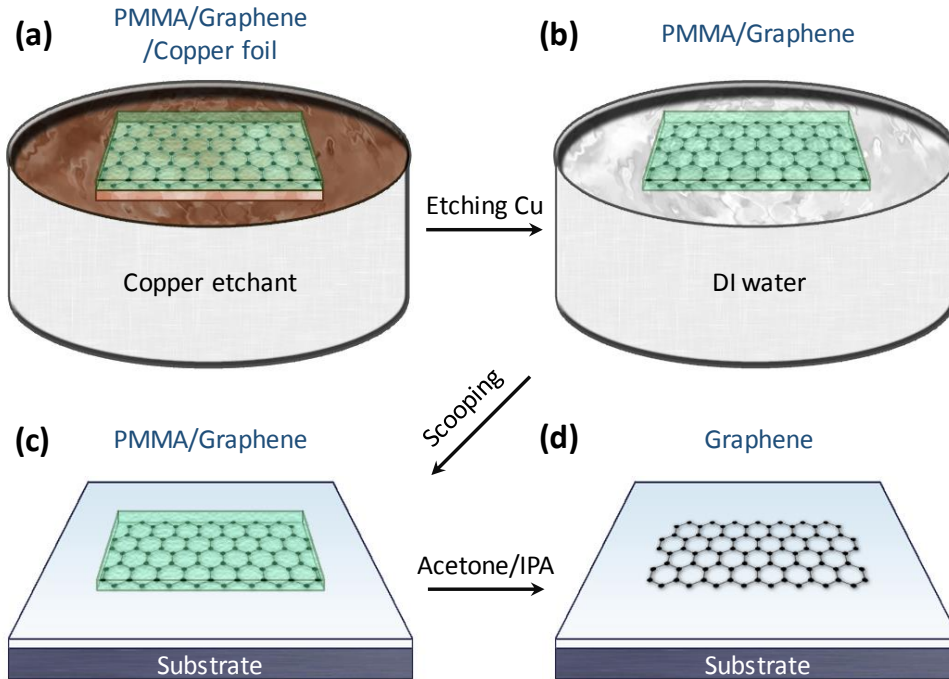


Figure 2.10 | Graphene transfer. (a) Etching copper foil in copper etchant. (b) Rinsing in DI water. (c) Scooping the PMMA/graphene layer onto a substrate. (d) Removing the top PMMA layer in acetone and rinsing in IPA.

Then, the copper foil is etched in $FeCl_3$ solution (Transene, CE 100) for an hour. After rinsing the PMMA/graphene stack on DI water thoroughly, the PMMA/graphene stack is scooped onto a target substrate.

If the copper etching time is too short or the PMMA/graphene stack is not properly rinsed in DI water, some metallic residues could be trapped between the graphene and the substrate [81], as shown in Fig. 2.11(a). After annealing the PMMA/graphene/substrate stack at $80\text{ }^\circ\text{C}$ for overnight in order to dry the water between the graphene and the substrate, the PMMA layer is removed by acetone and rinsed by IPA. If the PMMA/graphene/substrate stack is not annealed properly, it could cause weak adherence between the graphene and the substrate, and it leads to lifting off the graphene after removing the PMMA, as shown in Fig. 2.11(b).

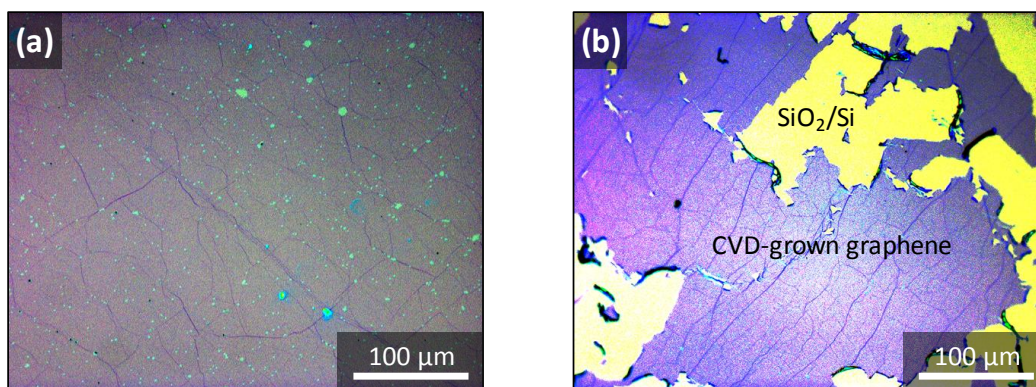


Figure 2.11 | Defective graphene transfer. (a) Trapped metallic residues beneath graphene. (b) Improperly annealing graphene before removing top PMMA layer.

2.2.3 Raman Spectroscopy of Graphene

Raman spectroscopy is a technique to observe molecular vibrations in materials, and it is very sensitive to molecular geometry and bonding [82]. Therefore, the Raman spectroscopy has been widely in modern semiconductor technologies to characterize the carrier concentration and the defects in semiconductors [83].

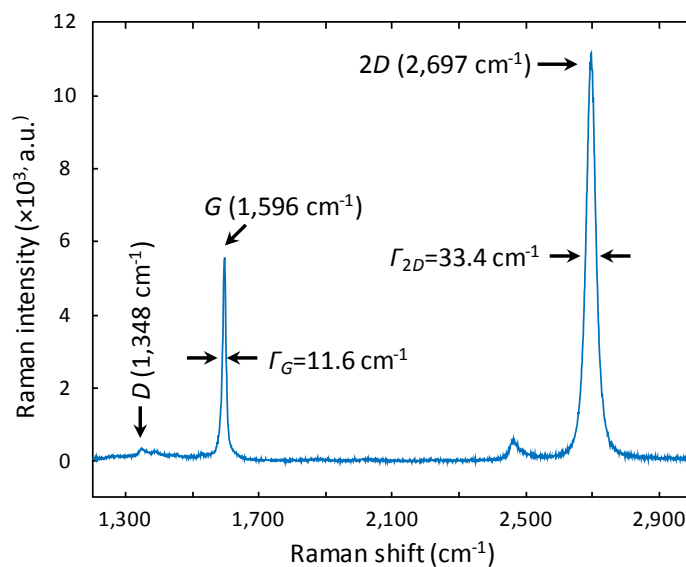


Figure 2.12 | Raman spectrum of graphene. Raman spectrum associated with phonons in graphene. The I_{2D}/I_G ratio is 2.01, and the I_G/I_D ratio is 16.8. Γ_G and Γ_{2D} denote the full width half maximums of the G and $2D$ peaks, respectively.

The Raman spectroscopy is also useful in the study of graphene because it can be utilized to investigate the characteristics of graphene. To be specific, we can figure out the doping level, the defect density, the strain, and the edge chirality of graphene [83-86]. In addition, it is possible to distinguish between a mono layer graphene and a multilayer graphene. Figure 2.12 shows Raman spectrum of the CVD-grown graphene transferred onto thermal SiO₂/Si substrate, and there are three distinctive peaks: 2*D* band, *G* band, and *D* band, and these Raman bands are associated with iTO and iLO phonons in graphene [83], and the Raman shift is determined by the energy difference between the photon absorption and emission [86].

In the Raman spectrum, the 2*D* band has the strongest intensity appearing at around 2,700 cm⁻¹, and it corresponds to the second order in-plane breathing mode of the carbon rings involving two iTO phonons at around the *K* point, as shown in Figs 2.13(a) and 2.14(a-b). For a monolayer graphene, the 2*D* band exhibits a single symmetric peak, and multilayer graphene splits the 2*D* band by overlapping a couple of other vibrational modes.

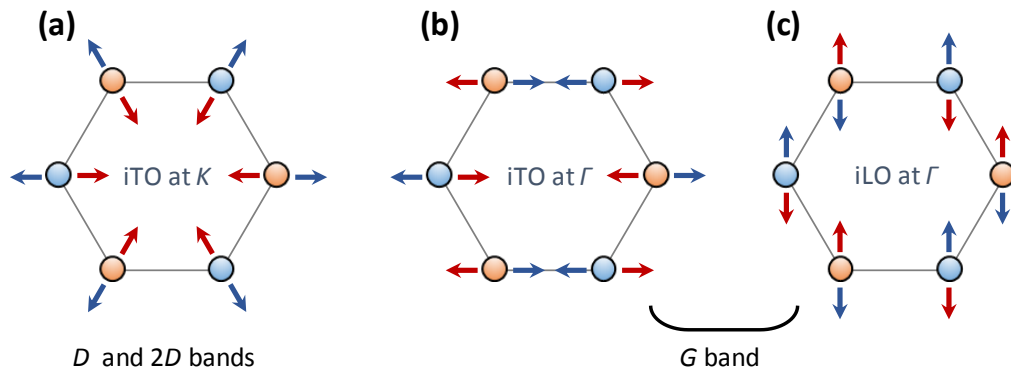


Figure 2.13 | Phonon vibrations in graphene. (a) iTO phonon at *K* point for *D* and 2*D* bands. (b) iTO phonon and (c) iLO phonon at Γ point for *G* band.

At around 1,600 cm⁻¹, there is a *G* band originating from the first order in-plane stretching mode of the carbon rings, and the *G* band is associated with doubly degenerate in-plane phonon modes (iTO and iLO phonons) at the center of the Brillouin zone (Γ point), as shown in Figs 2.13(b-c) and 2.14(c). The *G* band position redshifts with increasing the number of graphene layer.

The *D* band shown at around 1,350 cm⁻¹ is referred to the disorder band or the defect band in graphene. The *D* band is also the second order in-plane breathing mode of the carbon rings (iTO phonon at around the *K* point), as shown in Figs 2.13(a) and 2.14(d). In contrast to the 2*D* band, it is activated by proximity to defects in graphene for the momentum conservation. Since the electron

scattering by the defects in graphene is an elastic scattering process, the Raman shift in the D band is half of the Raman shift in the $2D$ band.

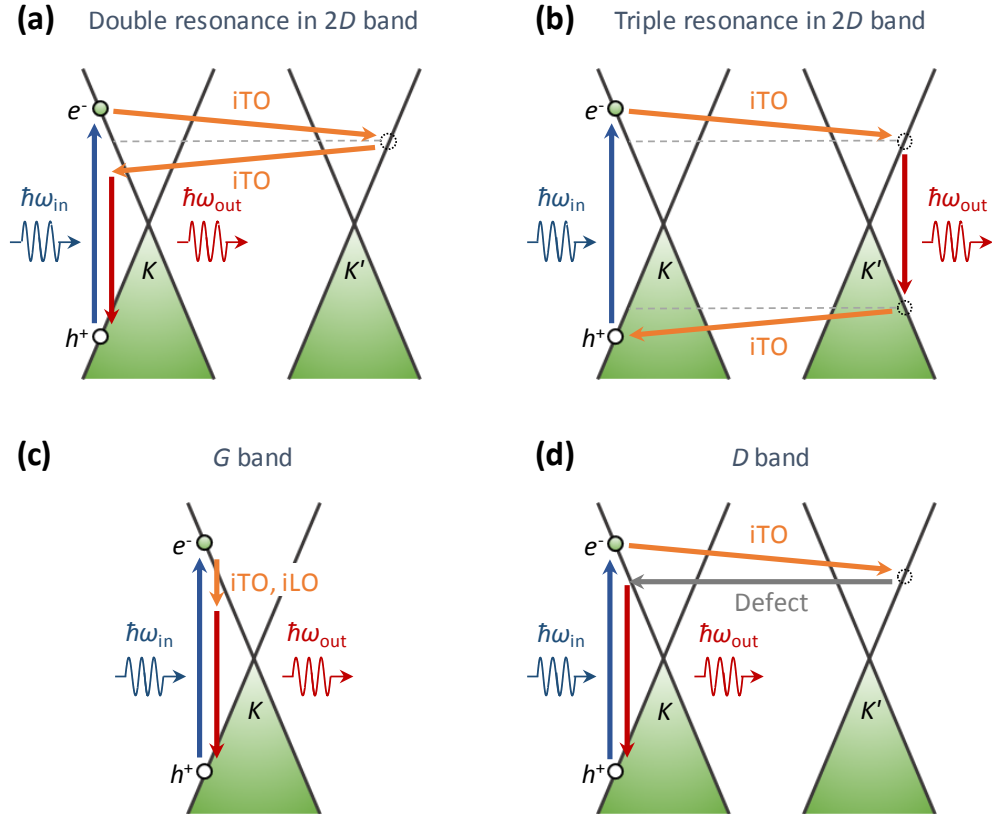


Figure 2.14 | Raman spectral process in graphene. (a) Double resonance $2D$ band process. (b) Triple resonance $2D$ band process. (c) First-order G band process. (d) Second-order D band process involving inelastic one phonon and elastic electron scattering on defects.

By comparing the each peak intensity, we can characterize the properties of graphene. To begin with, we can easily determine whether the graphene is monolayer from the ratio between the intensities of the $2D$ band (I_{2D}) and the G band (I_G). If the graphene is multilayer, the I_{2D} is usually smaller than the I_G . In Fig. 2.12, the I_{2D}/I_G ratio is 2.01, and it indicates that the graphene is monolayer.

When we transfer the graphene on a substrate, there could be several impurities. For example, water could be trapped between the graphene and the substrate during the scooping process [87-89]. There could be some remaining iron ions or chlorine ions beneath the graphene, which are the main components for the copper etchant [81]. In addition, it is very hard to completely remove the PMMA coated on the graphene because sp^3 hybridization is produced between the

PMMA and the graphene [90, 91]. Those impurities act as dopants for graphene, and it induces the background doping in graphene. This background doping can be also estimated from the I_{2D}/I_G ratio. Assuming that the graphene Fermi level is aligned at the Dirac point, a monolayer graphene transferred onto a SiO₂/Si substrate exhibits the $I_{2D}/I_G \sim 3$. If there are some impurities in the graphene, this ratio decreases because of the background doping [92-94]. In Fig 2.12, the I_{2D}/I_G ratio is about 2.01 without a gating bias, and it indicates that there is a certain amount of background doping in the graphene. More accurate background doping level is measurable by a transport measurement, and it will be discussed in Section 2.2.4.

The intensity of the D band (I_D) is proportional to the density of the defects in graphene, and we can estimate the amount of the defects by measuring the D band. In exfoliated graphene or graphite, the D band is very weak because they are nearly defect free. When we grow graphene using a CVD method, there should be a certain amount of defects in graphene originating from missing carbon atoms or grain boundaries between adjacent crystalline domains. In Fig. 2.12, the D band is nearly discernible, and the I_G/I_D ratio is 16.8, which indicates that there are few defects in the CVD-grown graphene. We can observe a broad peak at around the D band, and it originates from the mixture of sp^2 and sp^3 hybridization of amorphous carbon produced by the PMMA residues on graphene [95, 96].

2.2.4 Transport Measurement

To determine the graphene Fermi level with a gating bias, we first have to measure the background doping level in graphene. During the transfer process, impurities, such as residual metallic ions or water, can be trapped between the graphene and the substrate. Moreover, it is not easy to completely remove the PMMA residue on the graphene in solvent [90, 91, 95]. Those impurities act as dopants in graphene, and it induces a certain amount of background doping. To measure the background doping level in graphene, we perform the transport measurement, as shown in Fig. 2.15(a). In this configuration, the resistance between the source and the drain is measured as varying the gate voltage (V_G) between the graphene and the back electrode. As shown in Fig. 2.15(b), the resistance is maximized at the charge neutral point, where the graphene Fermi level is aligned with the Dirac point, because the carrier density is minimized at the CNP, and it leads to reducing the graphene conductivity. Here, the CNP is not located at zero gate voltage because impurities on the graphene and between the graphene and the substrate induces background doping. In most of the cases, such impurities mentioned above induce hole doping in graphene. Therefore, the CNP in graphene is observed in a positive gate voltage.

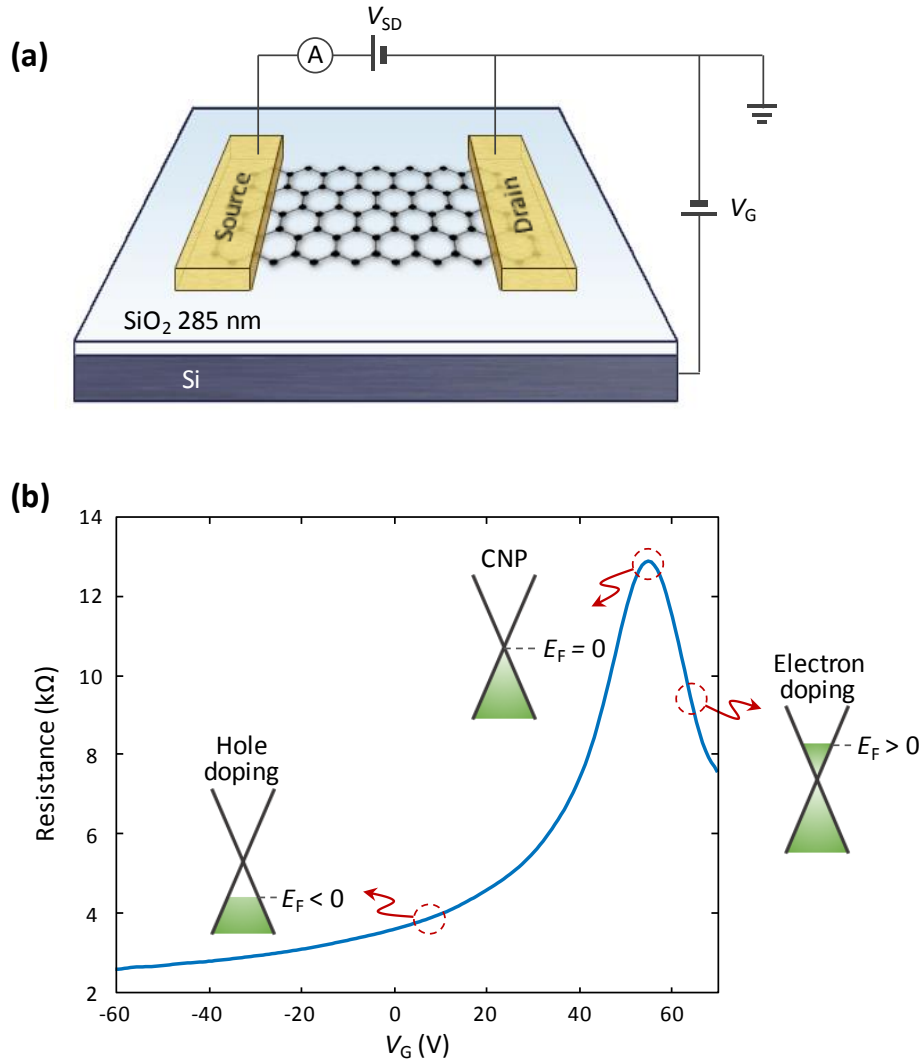


Figure 2.15 | Transport measurement. (a) Schematic of transport measurement in graphene to measure the charge neutral point (CNP). (b) Gate-dependent resistance of graphene transferred onto SiO₂ 285nm/Si substrate exhibiting the CNP at V_G=55V.*

In this electrostatic gating method, we can calculate gate-dependent graphene Fermi level using a simple capacitor model [92]. When we apply a gate voltage (V_G), an electrostatic potential difference (ϕ) is created between the graphene and the back electrode, and additionally accumulated charges in graphene induce a small shift in the graphene Fermi level (ΔE_F). Assuming there is no background doping in graphene, the gate voltage is expressed by

$$V_G = \phi + \frac{\Delta E_F}{e} \quad (2.9)$$

* This data is excerpted from Ref. 101 with the author's approval.

where e is the elementary charge. In Eq. (2.9), electrostatic potential difference ϕ is determined by the geometric capacitance C , and the chemical capacitance of the graphene induces the $\Delta E_F/e$. Here, it has been reported that the electrostatic potential ϕ is much larger than the potential by graphene Fermi level shift $\Delta E_F/e$ [92]. Therefore, we can assume $V_G \approx \phi$.

When carriers are accumulated by the gate voltage, the electrostatic potential ϕ is given by

$$\phi = \frac{Q}{C} = \frac{ne}{C} \quad (2.10)$$

where Q is the number of accumulated carriers, and n is the carrier density. And, the geometric capacitance is calculated by

$$C = \frac{\kappa\epsilon_0}{d} \quad (2.11)$$

where κ is the dielectric constant of the insulator, ϵ_0 is the vacuum permittivity, and d is the insulator thickness. Using Eqs. (2.9-2.11), we can convert the gate voltage V_G to carrier density n . With given carrier density n , the graphene Fermi level is calculated by

$$|E_F| = \hbar v_F \sqrt{\pi n} \quad (2.12)$$

where v_F is the Fermi velocity in graphene ($v_F \approx 1 \times 10^8$ cm/s).

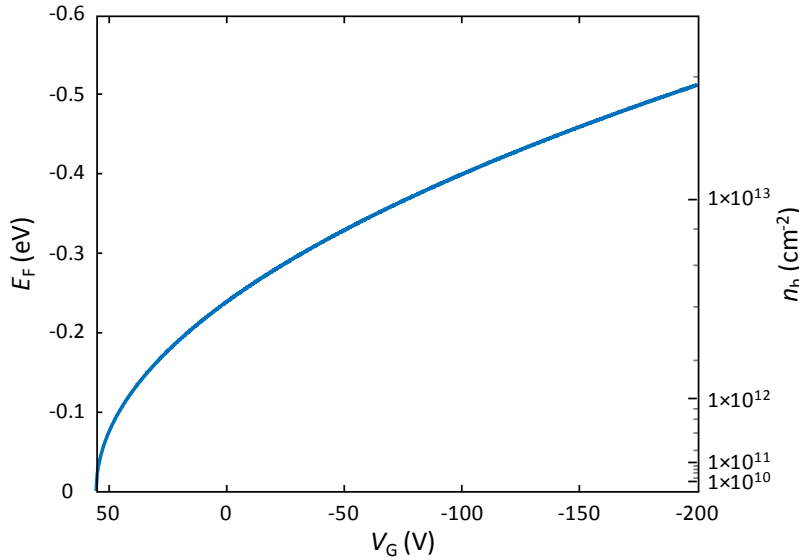


Figure 2.16 | Graphene doping. Gate-dependent graphene Fermi level (E_F) and graphene carrier density (n_h) on SiO₂ 285 nm/Si substrate in a hole doping regime. The CNP is located at $V_G=55$ V, and the dielectric constant κ of SiO₂ is assumed as 3.9.

Figure 2.16 shows the converted graphene Fermi level of the graphene on SiO₂ 285 nm/Si substrate in Fig. 2.15(a) with the measured CNP, and the n_h in Fig. 2.16 indicates hole density in

graphene. In graphene plasmons, higher graphene Fermi level is preferable because stronger graphene plasmons can be excited if there are more carriers in graphene. However, the maximum graphene Fermi level is limited by the breakdown voltage of the insulator, and the graphene can be doped up to about -0.6 eV ($n_h=2.65\times 10^{13} \text{ cm}^{-2}$) in this gating method. To further increase the doping level, chemical doping or ionic gel can be used [93, 97, 98].

CHAPTER 3

ELECTRONICALLY TUNABLE RESONANT PERFECT ABSORPTION IN GRAPHENE PLASMONIC METASURFACE

Graphene plasmons have been recently utilized to create a variety of dynamically tunable metasurfaces whereby the reflected or transmitted radiation can be controlled by varying the graphene carrier density. The efficiencies of these devices, however, have been low and largely limited by the poor coupling between free-space photons and graphene plasmons. Here we propose and demonstrate electronically tunable resonant absorption in graphene plasmonic metasurfaces enhanced by substrate control and noble metal plasmonic effects. Theoretical calculations predict that perfect absorption in the proposed metasurface is no longer limited by graphene carrier mobility. We present a rigorous analytic model based on effective surface admittance to elucidate the origin of the enhanced absorption, which shows that the perfect absorption is achieved when the interaction between the graphene plasmonic metasurface and the substrate is carefully engineered to induce critical coupling to free-space. Experimental measurements reveal 96.9% absorption in the graphene plasmonic metasurface at $1,389\text{ cm}^{-1}$, corresponding to a modulation efficiency of 95.9% in reflection.

3.1 Introduction

Graphene based optical modulators and phase shifters have recently emerged as an area of intense research partly due to the ability of confined graphene plasmonic resonances to create a strong electrostatic response at THz to mid-IR frequencies. Additionally, the high confinement factor of graphene plasmons allow for the creation of highly miniaturize [41-44, 46, 48-50] and active optical elements [51, 59, 60, 99-117]. Despite these capabilities, a major obstacle in graphene plasmonics is the low coupling rate between free-space photons and graphene plasmons, which leads to low device efficiency. This detrimental effect is due to the inherent thinness of graphene, as well as the large wavevector mismatch between graphene plasmons and free-space photons [41, 49, 50]. To circumvent these issues, large chemical doping [104, 105], carefully designed substrates [59, 60, 106, 107], and combined subwavelength noble metal plasmonic structures [108-117] have been utilized to either increase the oscillator strength of the graphene, or impedance match the graphene plasmons to free-space photons.

In spite of these efforts, even 50% absorption in graphene plasmonic ribbons (GPRs) has not yet, to the best of our knowledge, been realized in mid-infrared even as simple theoretical schemes have predicted 100% [59, 60]. This discrepancy is due largely to the low carrier mobility in processed graphene samples (due to edge roughness in GPRs or PMMA residue from processing [35, 89, 90, 118, 119]) in comparison to the large mobilities expected in theoretical work which have much higher oscillator strengths. Furthermore, it is still unclear that this high carrier mobility can be retained at high frequencies.

In this chapter, we devise a series of graphene plasmonic metasurfaces that exhibit incrementally higher levels of electronically tunable resonant absorption through systematic improvements in materials choice and geometrical design. First, we utilize lower permittivity substrates to improve resonant absorption in GPRs through better wavevector matching between graphene plasmons and free-space photons. Second, by confining the light through noble metal plasmonic subwavelength metal slits we can increase the field strength around GPRs to improve oscillator strength. And third, by exploiting image GPRs created by the metal slit edges, we can further augment the light-matter interactions in GPRs leading to significant enhancement in resonant absorption. Unlike other mid-infrared perfect absorbers solely relying on noble metal plasmonic effects [111, 120], we create perfect absorption in the graphene itself by utilizing graphene plasmon resonance enhanced by noble metal plasmonic light focusing effect, providing an ideal platform for tunable strong light matter interactions.

In the proposed graphene plasmonic metasurfaces, theoretical calculations predict perfect absorption in mid-infrared with graphene carrier mobility as low as $200 \text{ cm}^2\text{V}^{-1}\text{s}^{-1}$ and at a moderate doping with the graphene Fermi level position less than -0.6 eV , which are more realistic parameters than those previously proposed in devices to experimentally realize the perfect absorption. We describe the nature of these improvements by using an effective surface admittance inspired theoretical model, which reveals that the perfect absorption is achieved when the interaction between the graphene plasmonic metasurface and the substrate is carefully engineered to induce critical coupling to free-space. In mid-infrared reflection measurement, we demonstrate in a fabricated device that electronically tunable resonant absorption can be increased to 96.9% at $1,389 \text{ cm}^{-1}$, with a modulation efficiency of 95.9%.

3.2 Device Geometry and Light Modulation Mechanism.

Figure 3.1 shows the three reflection-type light modulators based on GPRs that we develop in this work. All devices are designed on $\text{SiO}_2/\text{SiN}_x$ membrane stacks with a back reflector (Ti 3 nm/Au 100 nm), which create a “Salisbury screen” effect to enhance absorption in the GPRs [59, 60, 107].

Type A device in Fig. 3.1(a) corresponds to a device consisting of bare GPRs on the SiO_2 150 nm/ SiN_x 1 μm /Au substrate with 100 nm/100 nm of ribbon/ gap width. Type B and C devices on the SiO_2 150 nm/ SiN_x 500 nm/Au substrate in Figs. 3.1(b) and (c) have GPRs coupled to subwavelength metal slits, and the GPRs are patterned inside the slits. The metal strips consist of Ti 2 nm/Au 80 nm. In the type B device, the GPR is located at the center of the slit, and the ribbon, the metal slit and strip width are 100 nm, 200 nm, and 910 nm, respectively. Compared to the type B device, one side of the GPR in the type C device is at the center of the slit, and another end is buried beneath the metal strip. The type C device has 50 nm wide ribbons and 100 nm/615 nm of metal slit/strip width. The total area for each device is about $75 \mu\text{m} \times 75 \mu\text{m}$, and their SEM images are shown in Figs. 3.1(d-i).

The geometry of all devices were chosen such that they would display maximum absorption at $1,356 \text{ cm}^{-1}$ with the graphene Fermi level below -0.6 eV , which were the similar conditions of maximum absorption that we reported for a standard GPR device on SiN_x/Au substrate [60], which we refer to here as type 0 device. Varying the substrate and surface environment can yield tangible benefits towards the goal of achieving perfect absorption in electrostatically gated graphene structures with lower graphene carrier mobility.

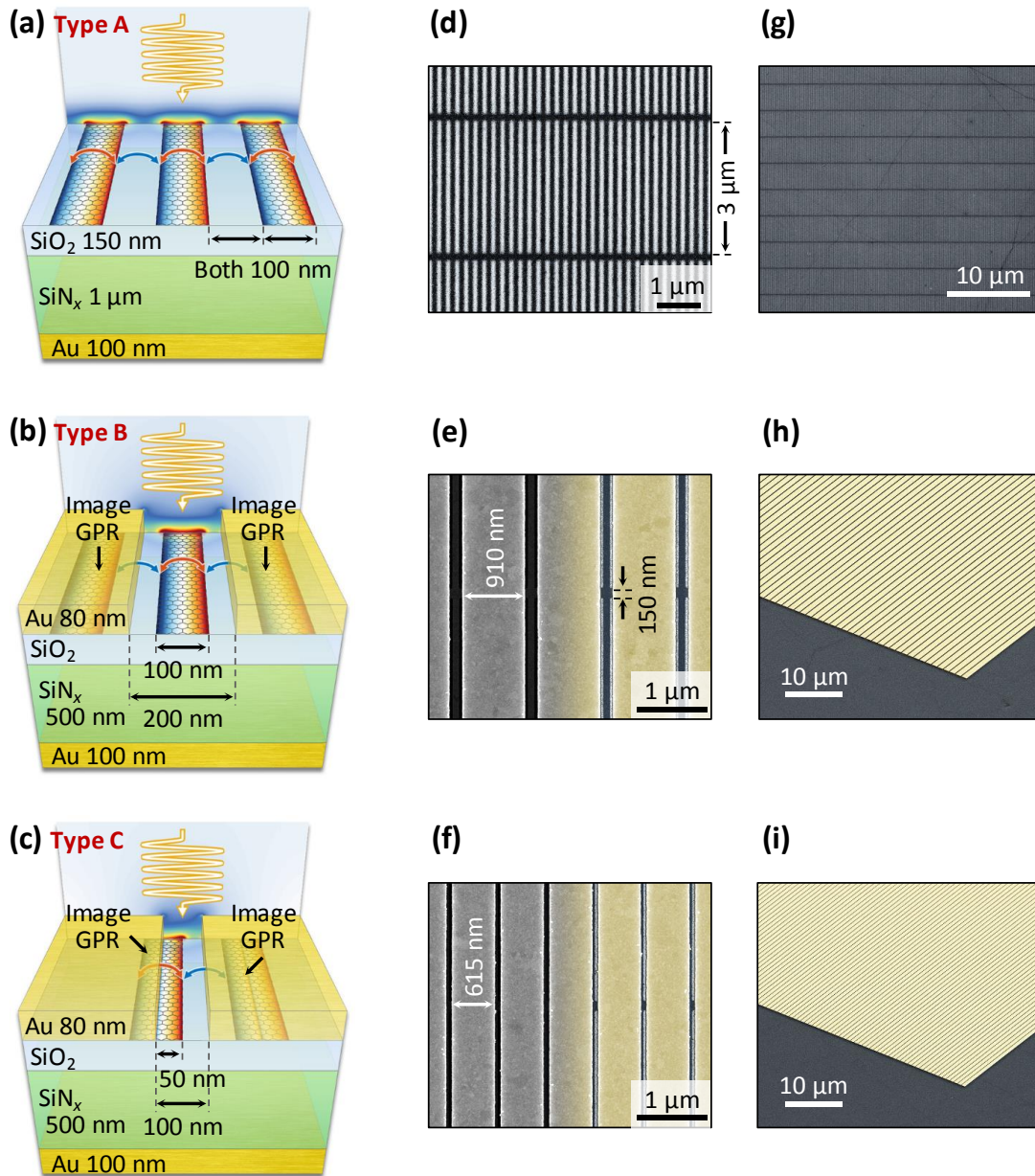


Figure 3.1 | Device geometry. Schematic of (a-c) type A, B, and C devices, respectively, and (d-i) corresponding SEM images (false color). In a-c, field distributions on the back side correspond to electric field distributions, and $\text{Re}(E_z)$ distributions are overlapped in graphene plasmonic ribbons (GPRs). In the SEM images, the dark strips are the GPRs. In e and f, the left sides are the original SEM images, and contrast and color adjusted SEM images are overlapped on the right side to display clear GPRs inside the slits. To prevent electrical disconnection, GPRs have 150 nm wide bridges, and the length of the GPR strip is 2.5 μm . In g, the bright regions correspond to the dead resonators due to electrical disconnections.

Table 3.1 overviews the theoretical conditions for perfect absorption for the type 0 to C devices with the required effective graphene carrier mobility shown for each geometry. These results show that varying the substrate and surface environment can yield tangible benefits towards the goal of achieving perfect absorption in electrostatically gated graphene structures. Here, we point out that the optimized SiN_x thickness for the type B and C devices is thinner than 1 μm due to the phase shift of light as passing through the metasurfaces, which will be discussed later in terms of admittance matching.

	Type 0	Type A	Type B	Type C
μ_h (cm ² V ⁻¹ s ⁻¹)	3,174	2,271	613	315
E_F (eV)	-0.484	-0.484	-0.486	-0.482

Table 3.1 | Conditions for perfect absorption at 1,356 cm⁻¹. Graphene carrier mobility and graphene Fermi level are denoted by μ_h and E_F , respectively, and the negative E_F indicates hole doping.

3.3 Type A: Graphene Plasmons on Low Permittivity Substrate

3.3.1 Electric Field Enhancement by Salisbury Screen

In order to enhance the absorption in GPRs, we exploited field enhancement at around the GPRs by Salisbury screen consisting of a dielectric stack and a back reflector [59-61]. Since the field enhancement at the interface between the air and the dielectric stack is a result of the interference between the incoming light and the reflected light from the back reflector, the electric field intensity at the interface could be larger or smaller than the incoming light depending on the wavelength and the dielectric stack thickness. When the thickness of the dielectric stack matches to the quarter wavelength condition, the electric field intensity is maximized at the interface because the phase shift of the reflected light at the back reflector is π , which leads to constructive interference at the air/dielectric stack interface at the quarter wavelength condition. Theoretical maximum enhancement is a factor of 4, and the enhancement factor decreases with absorption in the dielectric stack and the back reflector.

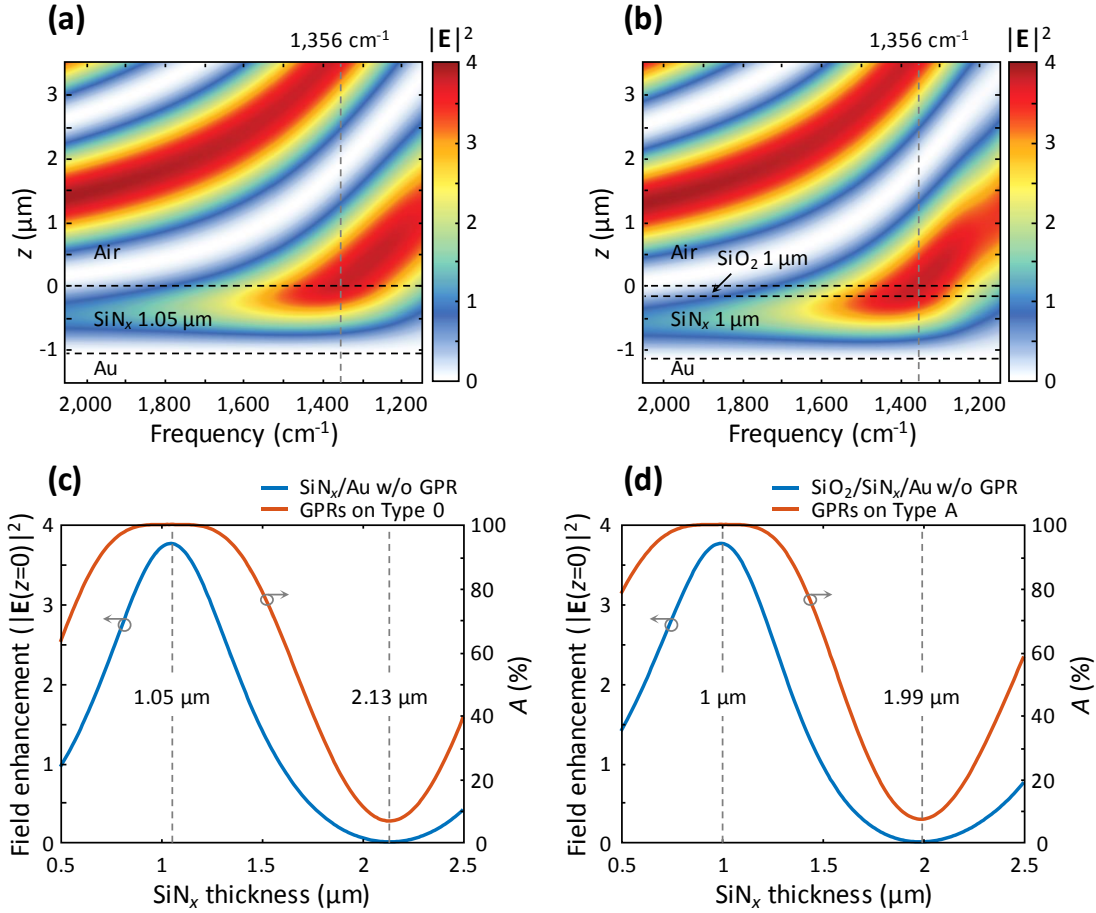


Figure 3.2 | Substrate-dependent field enhancement. (a) Field enhancement as a function of frequency on SiN_x 1.05 μm/Au and (b) corresponding absorption in the type 0 device at 1,356 cm⁻¹ as a function of the SiN_x thickness (d_{SiN_x}). (c) Field enhancement as a function of frequency on SiO₂ 150 nm/SiN_x 1 μm/Au and (d) corresponding absorption in the type A device at 1,356 cm⁻¹ as a function of the SiN_x thickness (d_{SiN_x}).

Figures 3.2(a) and (b) show the electric field intensity enhancement on the SiN_x/Au and the SiO₂/SiN_x/Au Salisbury screens. Both Salisbury screens are optimized to maximize the electric field intensity at 1,356 cm⁻¹ on the air/SiO₂ interface, and the maximum electric field intensity enhancements on the SiN_x on the SiO₂ are 3.76 and 3.77 at 1,356 cm⁻¹, respectively.

Figures 3.2(c) and (d) show the absorption in the GPRs by the field enhancement at 1,356 cm⁻¹. The electric field at the air/dielectric interface exhibit resonance depending on the SiN_x thickness, and the maxima and the minima occur at $d_{\text{sub}} \approx \frac{\lambda_0}{4n_{\text{sub}}}$ and $d_{\text{sub}} \approx \frac{\lambda_0}{2n_{\text{sub}}}$, respectively (λ_0 : free-space wavelength, d_{sub} : substrate thickness, n_{sub} : effective refractive index of substrate). As a result of the standing wave resonance in the substrate, the absorption in the GPRs follows the

field enhancement profiles, as shown in Figs. 3.2(c) and (d). Figure 3.3 shows that the near-fields around the GPRs also increase or decrease depending on the field enhancement.

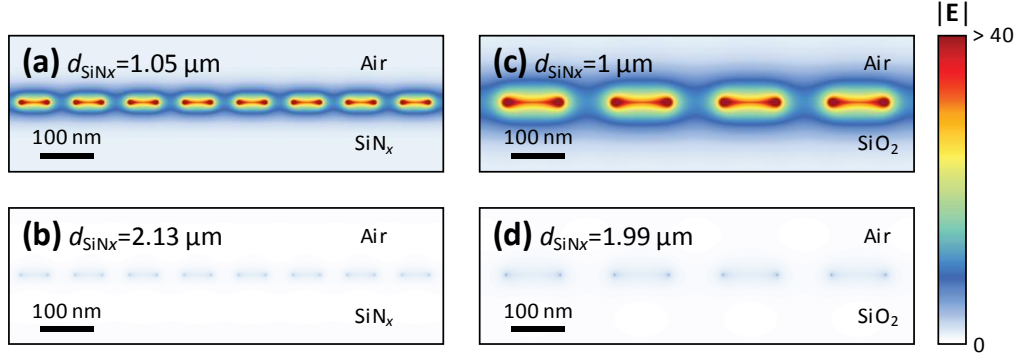


Figure 3.3 | Substrate-dependent electric field distributions. Electric field distributions (a) at the maximum absorption and (b) at the minimum absorption in the type 0 device. Electric field distributions (c) at the maximum absorption and (d) at the minimum absorption in the type A device.

3.3.2 Graphene Plasmon Dispersion Relation

The fundamental problem that leads to low absorption in graphene plasmonic devices is the large wavevector mismatch with free-space [41, 49, 50]. While this property is useful for strong light-matter interactions and light confinement, it leads to low efficiency devices. One way to address this problem is to heavily dope the graphene, which blueshifts graphene plasmons at a given wavelength. However, chemical doping, such as using ionic gels, could limit the switching speed and the applicability of the devices in solid state hardware. A more attractive idea is utilizing a low permittivity substrate which naturally blueshifts graphene plasmons. To see this, consider the dispersion relation of a transverse magnetic graphene plasmons in the quasi-static regime [45, 56, 57]:

$$k_p = \epsilon_0(1 + \epsilon_{\text{sub}}) \frac{i\omega}{\sigma} \quad (3.1)$$

where ϵ_{sub} is the substrate relative permittivity, and σ is the optical surface conductivity of graphene [63, 64]. This dispersion relation implies that graphene plasmons have a relatively small wavenumber on a low permittivity substrate, thus reducing the wavevector mismatch between free-space photons and graphene plasmons, resulting in high coupling efficiency.

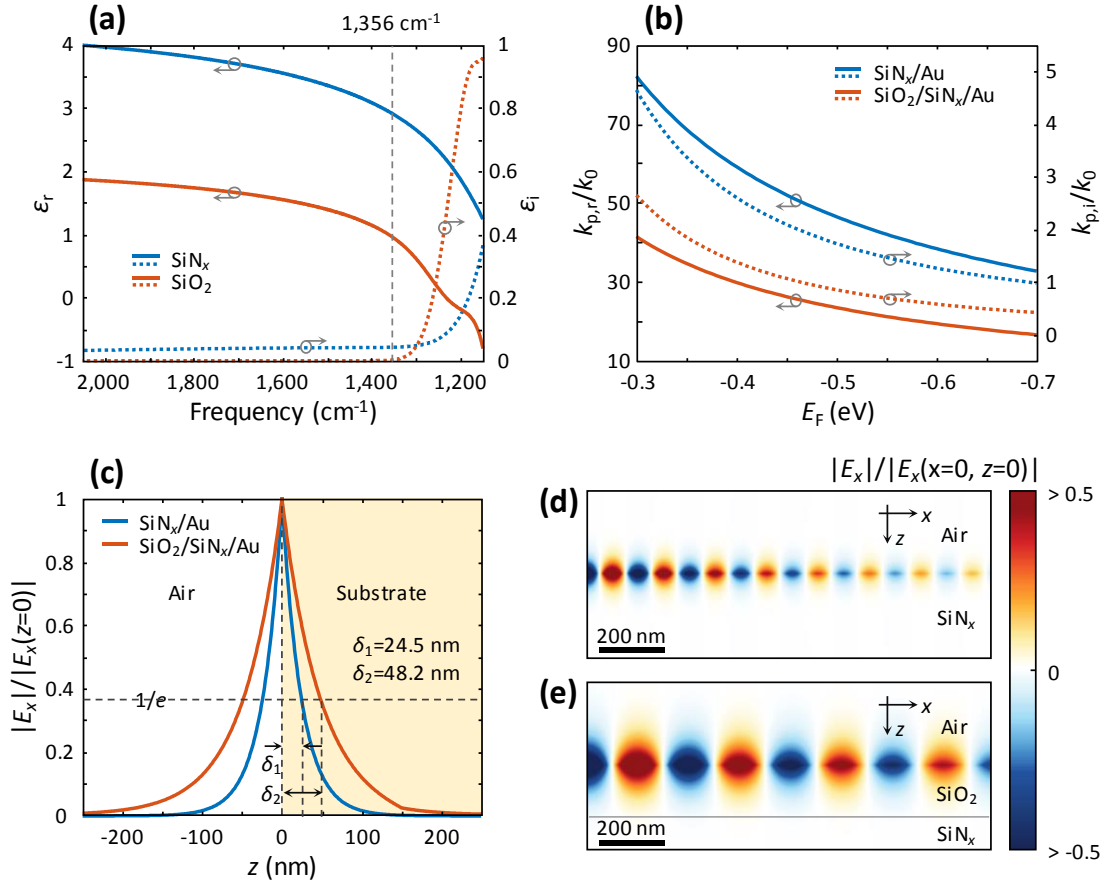


Figure 3.4 | Graphene plasmons on low permittivity substrate. (a) Permittivities of SiO_2 and SiN_x measured by mid-infrared ellipsometry. (b) Normalized wavenumbers (k_p/k_0) of graphene plasmons at 1,356 cm^{-1} on SiN_x/Au and $\text{SiO}_2/\text{SiN}_x/\text{Au}$ substrates. (c) E_x profile of graphene plasmon waveguide mode on each Salisbury screen substrate. Propagating E_x distribution of graphene plasmon along the graphenes on (d) SiN_x/Au and (e) $\text{SiO}_2/\text{SiN}_x/\text{Au}$ substrates.

Figure 3.4(a) is the relative permittivities of SiO_2 and SiN_x measured by mid-infrared ellipsometry showing that SiO_2 has lower permittivity than SiN_x . To verify the low permittivity effect at 1,356 cm^{-1} , we designed the Salisbury screens comprised of SiN_x 1.05 $\mu\text{m}/\text{Au}$ and SiO_2 150 nm/ SiN_x 1 $\mu\text{m}/\text{Au}$ stacks. The dispersion relation of graphene plasmons on each Salisbury screen is calculated in Fig. 3.4(b) as a function of graphene Fermi level (E_F). Since SiO_2 has lower permittivity than SiN_x , the graphene plasmon on SiO_2 exhibits a smaller wavenumber (or longer wavelength) than on SiN_x , as shown in Fig. 3.4(b). The normalized wavenumber (k_p/k_0) of graphene plasmon on $\text{SiO}_2/\text{SiN}_x/\text{Au}$ is $24.2+i0.91$ with $E_F=-0.484$ eV, and this wavenumber is nearly half of the graphene plasmon wavenumber on SiN_x/Au , where the normalized wavenumber is $48.1+i1.82$ with the same E_F . Here, the graphene plasmon on the SiO_2 barely recognizes the bottom SiN_x

because the skip depth into the substrate ($\delta_2=48.2$ nm) is shorter than the SiO_2 thickness (150 nm), as shown in Fig. 3.4(c). In addition, the graphene plasmon on the SiO_2 has a smaller confinement factor than on the SiN_x . As a result, the graphene plasmon on the SiO_2 has smaller decay rate, and it can propagate more distance than on the SiN_x , as shown in Figs. 3.4(d) and (e). The propagation lengths on the SiN_x/Au and on the $\text{SiO}_2/\text{SiN}_x/\text{Au}$ substrates are 323 nm and 647 nm, respectively.

3.3.3 Perfect Absorption in Graphene Plasmonic Ribbons

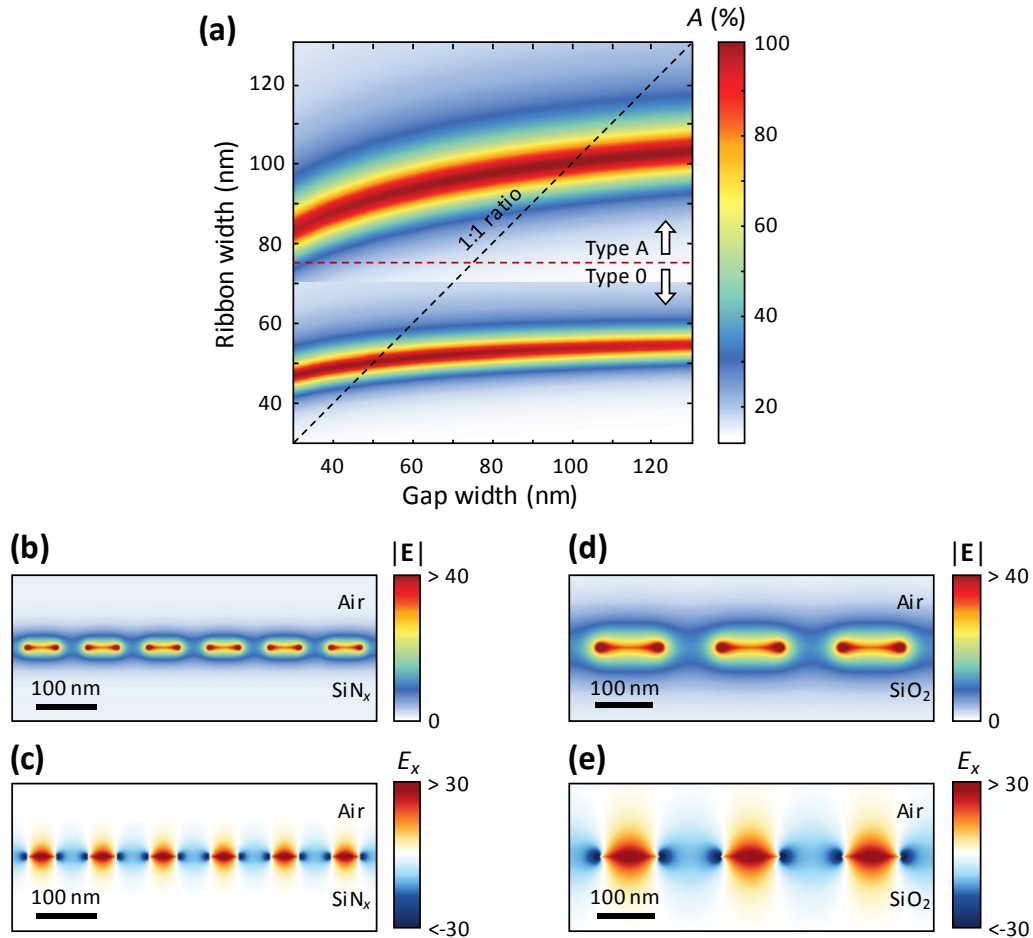


Figure 3.5 | Graphene plasmonic ribbons. (a) Absorption in graphene plasmonic ribbons (GPRs) as a function of the ribbon width and the gap width. (b) Electric field distribution and (c) E_x around the 50.2 nm/50.2 nm of ribbon/gap width GPRs on the type 0 device. (d) Electric field distribution and (e) E_x around the 100 nm/100 nm of ribbon/gap width GPRs on the type A device.

The required ribbon width of GPRs for resonant absorption is determined by the graphene plasmon wavelength [101]. Therefore, wider GPRs can be used on the $\text{SiO}_2/\text{SiN}_x/\text{Au}$ substrate

compared to the SiN_x/Au substrate. Figure 3.5(a) shows absorption at $1,356\text{ cm}^{-1}$ on each Salisbury screen as a function of ribbon width and gap width with $E_F = -0.484\text{ eV}$. Along the 1:1 of ribbon:gap ratio line ensuring the same graphene coverage for both devices, we chose $50.2\text{ nm}/50.2\text{ nm}$ and $100\text{ nm}/100\text{ nm}$ of ribbon/gap width GPRs for the type 0 and A devices, respectively, and their electric field and E_x distributions are shown in Figs. 3.5(b-e). Since the wavevector mismatch is reduced on a low permittivity substrate, the type A device induces stronger resonance than the type 0 device. As a result, type A devices exhibits perfect absorption with $\mu_h = 2,271\text{ cm}^2\text{V}^{-1}\text{s}^{-1}$, while the $\mu_h = 3,174\text{ cm}^2\text{V}^{-1}\text{s}^{-1}$ is required in the type 0 device to achieve perfect absorption.

3.4 Type B and C: Coupled Subwavelength Metal Slits

3.4.1 Field Enhancement in Subwavelength Metal Slits

The Salisbury screen structure enhances the electric field intensity around GPRs via Fabry-Perot interference, and thus induces strong resonant absorption in GPRs [59-61]. While the back reflector increase the field strength by a factor of 4, larger improvements can be achieved with a carefully designed noble metal plasmonic antennas harvesting light efficiently [121, 122], which we outline in Figs. 3.6(a) and (b).

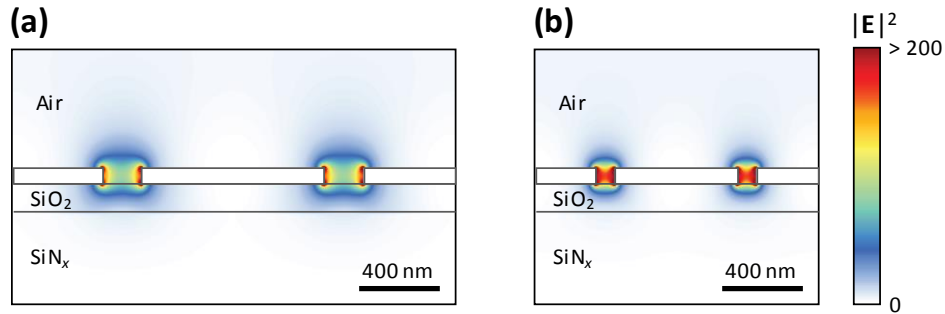


Figure 3.6 | Subwavelength metal slits. Electric intensity distributions without graphene plasmonic ribbons (a) in the type B slit and (b) in the type C slit.

As can be seen in Fig. 3.6, the type B and C slits provide much stronger field enhancement compared to the type A devices, exhibiting the enhancement factors of 147 and 226, respectively. Here, the field enhancement inside the type B and C slits is calculated by averaging electric field intensity along the air/ SiO_2 interface without intergap GPRs. In this simulation, the SiN_x thickness is adjusted to 480 nm in the type B and C devices because the quarter wavelength resonance condition in Salisbury screen is no longer valid due to additional surface inductance from the

subwavelength metal slits, and the details will be discussed in Section 3.5. The electric field and the E_x distributions of the type B and C devices with graphene plasmonic resonances are shown in Fig. 3.7.

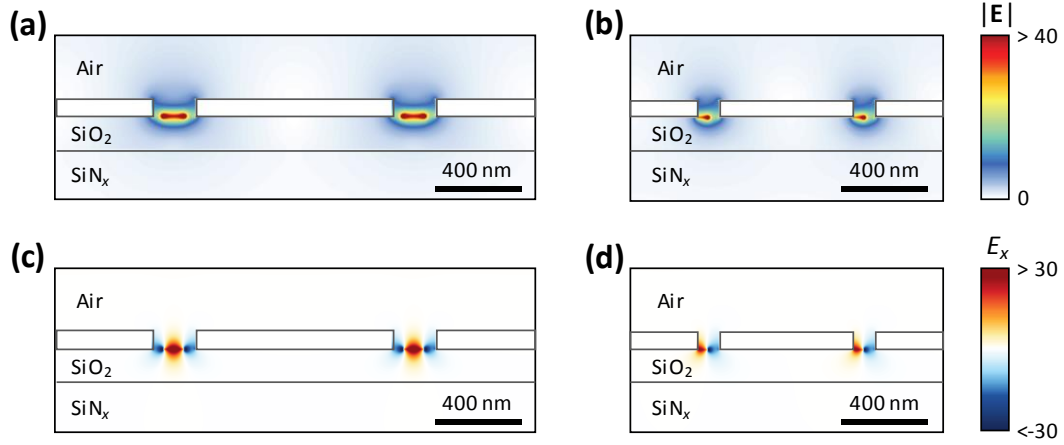


Figure 3.7 | Graphene plasmonic ribbons coupled to subwavelength metal slits. (a) Electric field and (b) E_x distributions in the type B device with graphene plasmonic resonances (c) Electric field and (d) E_x distributions in the type C device with graphene plasmonic resonances.

3.4.2 Perfect Absorption with Lower Graphene Carrier Mobility

Since the absorption in GPRs strongly depends on the oscillator strength of the graphene, the low graphene carrier mobility limits device performance [117]. Figure 3.8(a) summarizes the absorption in each device at $1,356 \text{ cm}^{-1}$ as a function of graphene carrier mobility with optimized graphene Fermi level. The graphene carrier mobilities required to achieve perfect absorption are $3,174$, $2,271$, 613 , and $315 \text{ cm}^2\text{V}^{-1}\text{s}^{-1}$ for the type 0, A, B and C devices, respectively.

The type A device reaches perfect absorption at lower graphene carrier mobility than the type 0 device because of the reduced wavevector mismatch between free-space photons and graphene plasmons. Further intensification in absorption at lower graphene carrier mobility is observed in the type B and C devices due to the enhanced field around the GPRs. The type C slit exhibits larger field enhancement than the type B slit because the narrower slit more effectively confines light into the slit. As a result, the type C device achieves perfect absorption at the lowest graphene carrier mobility. Figure 3.8(b) shows the tunable absorption spectra as a function of graphene Fermi level with $\mu_h=315 \text{ cm}^2\text{V}^{-1}\text{s}^{-1}$, and the maximum absorptions in the type 0, A, B, and C devices are 50.1%, 50.8%, 91.7%, and 100%, respectively. Absorption map of the type C device

as a function of frequency and graphene Fermi level is shown in Fig. 3.8(c), and absorption maps of other devices are shown in Fig. 3.9.

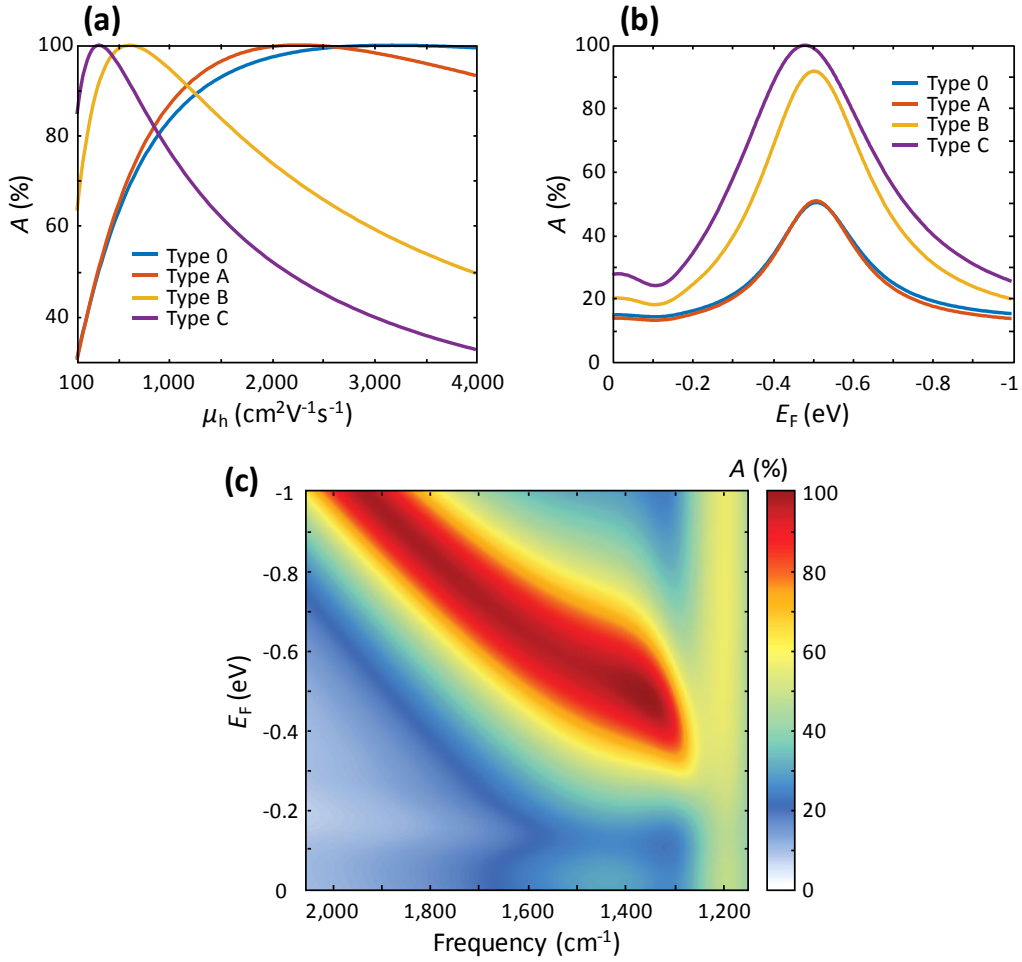


Figure 3.8 | Enhanced light-matter interactions in graphene plasmonic ribbons. (a) Absorption in each device as a function of graphene carrier mobility (μ_h). (b) Tunable absorption in each device with $\mu_h=315 \text{ cm}^2\text{V}^{-1}\text{s}^{-1}$ as a function of graphene Fermi level (E_F). (c) Absorption map in the type C device with $\mu_h=315 \text{ cm}^2\text{V}^{-1}\text{s}^{-1}$ as a function of frequency and graphene Fermi level (E_F). In these simulations, the SiN_x thickness for the type B and C device is 480 nm.

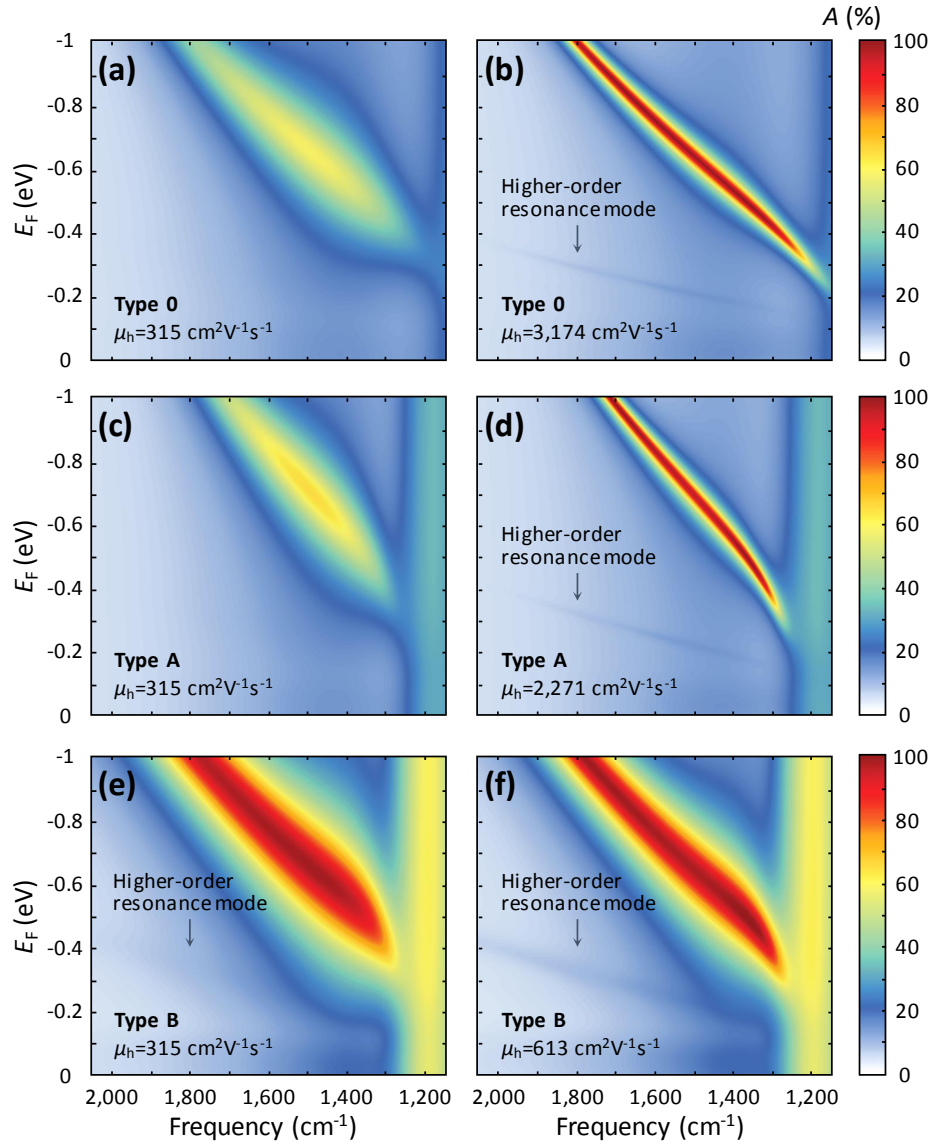


Figure 3.9 | Absorption maps. Absorption maps in the type 0 device with (a) $\mu_h=315 \text{ cm}^2\text{V}^{-1}\text{s}^{-1}$ and (b) $\mu_h=3,174 \text{ cm}^2\text{V}^{-1}\text{s}^{-1}$. Absorption maps in the type A device with (c) $\mu_h=315 \text{ cm}^2\text{V}^{-1}\text{s}^{-1}$ and (d) $\mu_h=2,271 \text{ cm}^2\text{V}^{-1}\text{s}^{-1}$. Absorption maps in the type B device with (e) $\mu_h=315 \text{ cm}^2\text{V}^{-1}\text{s}^{-1}$ and (f) $\mu_h=613 \text{ cm}^2\text{V}^{-1}\text{s}^{-1}$.

3.4.3 Image Graphene Plasmonic Ribbons

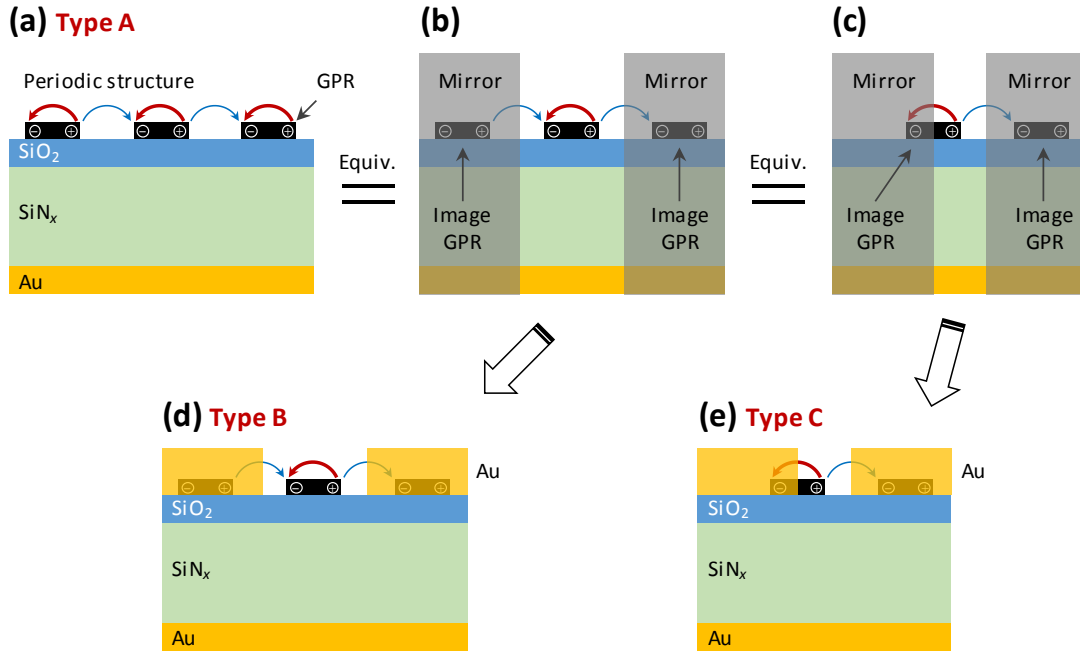


Figure 3.10 | Image graphene plasmonic ribbons. (a) Schematic of charge distribution and induced electric field by graphene plasmons in the type A device, and (b-c) equivalent schematic along with mirrors (or perfect electric conductor). (d-e) Schematic of charge distribution and induced electric field in the type B and C devices derived from equivalent models.

When GPRs are arrayed periodically, the GPRs interact with the adjacent GPRs, and create collective oscillation, as shown in Figs. 3.5(c) and (e). The red regions in Figs. 3.5(c) and (e) are due to the electric fields induced by the graphene plasmons, and the interaction between the adjacent GPRs corresponds the blue regions. With normally incident light, the electric field in a unit cell is symmetric, and the GPRs array is equivalent to a single GPR enclosed by mirror (or perfect electric conductor). Therefore, we can consider the adjacent GPRs as image GPRs inside the mirror, as shown in Fig. 3.10. In the type B device (Fig. 3.10(d)), the graphene plasmonic ribbons (GPRs) are located at the center of the metal slit. Since the metal strips efficiently reflect near-fields from the GPRs, we can consider the metal edges as mirrors similar to the perfect electric conductor boundary constructing image GPRs. In addition to mimicking the interaction between the adjacent GPRs, the metal edges contacting the GPRs in the type C device (Fig. 3.10(e)) reflect the near-fields induced in the GPRs, and virtually create twice wider GPRs. As a result, it creates an effectively collective oscillation, indicating that the GPRs in all type of devices are equivalent.

3.5 Surface Admittance Model

While the theoretical plots generated by full-wave simulations show large absorption enhancement in the proposed devices, it is desirable to develop an analytical model in order to fully understand how this enhancement occurs, and that can be utilized as a design guide for future devices.

In electromagnetics, admittance is defined as the ratio of transverse magnetic field over transverse electric field, and the admittance has been widely used in analyzing electromagnetic responses from multi-layered stacks in response to an incoming wave [61, 123]. The admittance of a finite-thickness layer is usually a complex value, and the real and imaginary part of the admittance correspond to conductance and susceptance of the layer, respectively. Here, the conductance and the susceptance represents the magnitude and the phase relation of the electromagnetic response from the layer, respectively.

3.5.1 Surface Admittance of Metasurface

Assuming that the metasurface thickness is much thinner than free-space light wavelength, the metasurface can be modeled by a thin screen located at $z=0$ with an effective surface admittance Y_s as Eq. (3.2) [60, 61, 111]. By solving the boundary conditions in Fig. 3.11(a) with Eq. (3.2), the effective surface admittance normalized by free-space admittance (Y_0) are derived as Eqs. (3.3) and (3.4) with the coefficients of Eqs. (3.5-6).

$$H_y(0^+) - H_y(0^-) = -Y_s E_x(0) \quad (3.2)$$

$$\tilde{Y}_{s,r} = \frac{Y_{s,r}}{Y_0} = \frac{1 - r_0}{1 + r_0} - \frac{B_1}{A_1} \quad (3.3)$$

$$\tilde{Y}_{s,t} = \frac{Y_{s,t}}{Y_0} = \frac{2}{A_1 t_0} - 1 - \frac{B_1}{A_1} \quad (3.4)$$

$$A_1 = \cos(n_{\text{SiO}_2} k_0 d_{\text{SiO}_2}) - i \frac{n_{\text{SiNx}}}{n_{\text{SiO}_2}} \sin(n_{\text{SiO}_2} k_0 d_{\text{SiO}_2}) \quad (3.5)$$

$$B_1 = n_{\text{SiNx}} \cos(n_{\text{SiO}_2} k_0 d_{\text{SiO}_2}) - i n_{\text{SiO}_2} \sin(n_{\text{SiO}_2} k_0 d_{\text{SiO}_2}) \quad (3.6)$$

Here, $\tilde{Y}_{s,r}$ and $\tilde{Y}_{s,t}$ are normalized surface admittances calculated from reflection coefficient (r_0) and transmission coefficient (t_0), respectively.

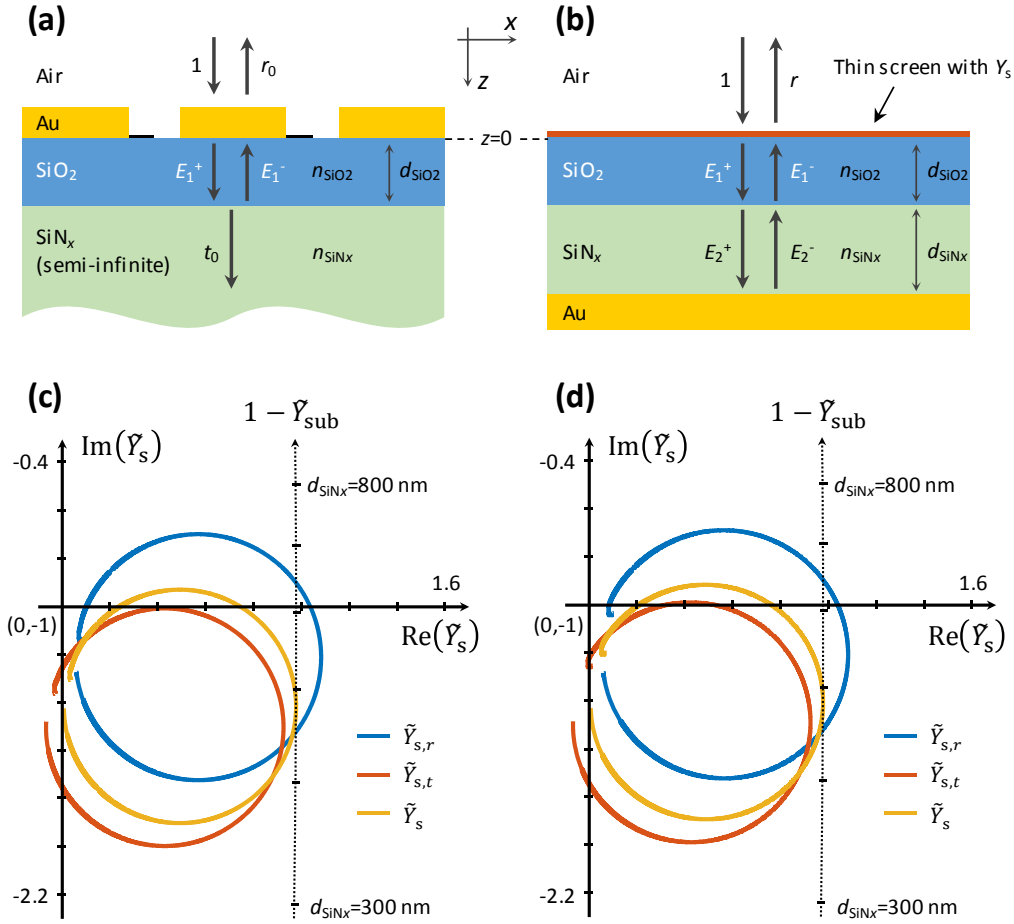


Figure 3.11 | Schematic of surface admittance. (a) Schematic of the metasurface consisting of graphene plasmonic ribbons coupled to subwavelength metal slits, and (b) corresponding a thin screen with effective surface admittance. Surface admittance charts of (c) the type B device with $\mu_h=613 \text{ cm}^2\text{V}^{-1}\text{s}^{-1}$ and (d) the type C device with $\mu_h=315 \text{ cm}^2\text{V}^{-1}\text{s}^{-1}$ showing the effect of the finite thickness metasurfaces. In c and d, the graphene Fermi level varies from 0 eV to -20 eV, and the frequency is $1,356 \text{ cm}^{-1}$.

In the type 0 and A devices, $\tilde{Y}_{s,r}$ and $\tilde{Y}_{s,t}$ are equal because Eq. (3.2) is the exact expression for the zero thickness of the metasurface [59, 61]. In the type B and C devices, however, the $\tilde{Y}_{s,r}$ and the $\tilde{Y}_{s,t}$ are different because light passing through the finite thickness metasurface undergoes phase shift [12], as shown in Figs. 3.11(c) and (d). Therefore, we evaluated the normalized effective surface admittance $\tilde{Y}_s = c_r \tilde{Y}_{s,t} + c_t \tilde{Y}_{s,r} + c_0$ to consider the phase shift through the finite thickness metasurface. The fitting parameters c_r , c_t , and c_0 were determined by comparing full-wave simulations and results from Eq. (3.8). For the type B device, the fitting parameters were $c_r=0.923-i0.148$, $c_t=0.008+i0.053$, and $c_0=0.062-i0.224$. For the type C device, the fitting parameters were

$c_r=0.922-i0.142$, $c_t=0.013+i0.051$, and $c_0=0.057-i0.216$. We expect that these fitting parameters are affected by the weak metal-insulator-metal plasmonic mode induced in the dielectric stack, which is not included in Eq. (3.8), when we combine the metasurface and the back reflector. However, this deviation is very small, indicating that the graphene plasmonic resonances in the metasurfaces are dominant in the devices.

To illustrate the physical meaning of the surface admittance, we modified a susceptibility model for a dispersive material [18],

$$\tilde{Y}_s(E_F) = \tilde{Y}_{s,\infty} + i\tilde{\chi}(E_F) = \tilde{Y}_{s,\infty} + i\tilde{\chi}_0 \frac{E_{F,0}/2}{(E_{F,0} - E_F) + i\Delta E_F/2} \quad (3.7)$$

where \tilde{Y}_s is the surface admittance normalized by free-space admittance (Y_0) as a function of graphene Fermi level (E_F), $\tilde{Y}_{s,\infty}$ is the normalized surface admittance at a high graphene Fermi level limit similar to permittivity at high frequency in the Debye model [124], $\tilde{\chi}_0$ is the difference in the normalized surface admittance between at low and at high graphene Fermi levels, $E_{F,0}$ is the graphene Fermi level at a resonance, and ΔE_F is the linewidth in graphene Fermi level. In the resonant medium model [18], the real and imaginary part of the susceptibility are related to the refractive index of a medium and the absorption, respectively. Therefore, the surface admittance is multiplied by i to match the real and imaginary part of the resonant medium model with the surface conductance and surface susceptance of the metasurface, respectively. We adopted $\tilde{\chi}(E_F)$ as a reduced susceptibility near resonance instead of a full susceptibility expression to account for the Lorentzian lineshape in the surface conductance from dipolar plasmonic resonance [18, 125]. To include the net susceptance of the metasurface dominated by noble metal plasmonic structure, $\tilde{Y}_{s,\infty}$ was taken at $E_F=-20$ eV. Figure 3.12 shows the surface admittances of the metasurface in the type 0, A, B, and C devices calculated by full-wave simulations and the surface admittance model fitted to the simulation result. The graphene carrier mobility was chosen to exhibit perfect absorption in each device.

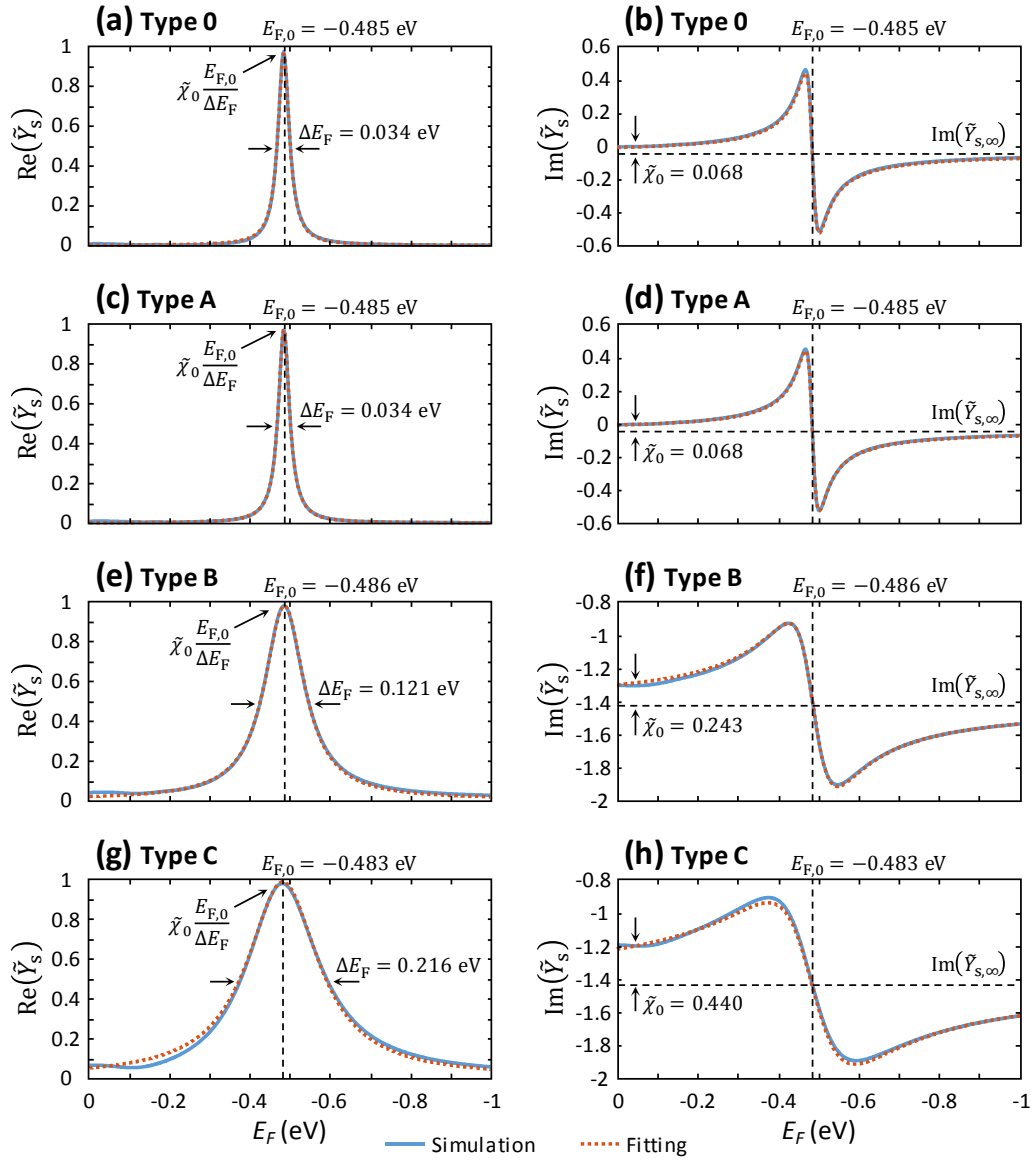


Figure 3.12 | Surface admittance fitting. (a) The real part and (b) imaginary part of the surface admittance of the type 0 metasurface with $\mu_h=3,174 \text{ cm}^2\text{V}^{-1}\text{s}^{-1}$. (c) The real part and (d) imaginary part of the surface admittance of the type A metasurface with $\mu_h=2,271 \text{ cm}^2\text{V}^{-1}\text{s}^{-1}$. (e) The real part and (f) imaginary part of the surface admittance of the type B metasurface with $\mu_h=613 \text{ cm}^2\text{V}^{-1}\text{s}^{-1}$. (g) The real part and (h) imaginary part of the surface admittance of the type C metasurface with $\mu_h=315 \text{ cm}^2\text{V}^{-1}\text{s}^{-1}$.

3.5.2 Analytic Model for Calculating Absorption

After obtaining the surface admittance from the semi-infinite substrate schematic, we can calculate the absorption of the device by considering the interaction between the metasurface and the Salisbury screen. By solving the boundary conditions in Fig. 3.11(b), the reflection coefficient is derived as Eq. (3.8) with the coefficients of Eqs. (3.9-12), and the absorption is $1-|r|^2$.

$$r = -\frac{\tilde{Y}_s + \frac{C_2 + n_{\text{Au}}D_2}{A_2 + n_{\text{Au}}B_2} - 1}{\tilde{Y}_s + \frac{C_2 + n_{\text{Au}}D_2}{A_2 + n_{\text{Au}}B_2} + 1} = -\frac{\tilde{Y}_s + \tilde{Y}_{\text{sub}} - 1}{\tilde{Y}_s + \tilde{Y}_{\text{sub}} + 1} = -\frac{\tilde{Y}_L - 1}{\tilde{Y}_L + 1} \quad (3.8)$$

$$A_2 = 1 - \frac{n_{\text{SiN}_x}}{n_{\text{SiO}_2}} \tan(n_{\text{SiO}_2}k_0d_{\text{SiO}_2}) \cdot \tan(n_{\text{SiN}_x}k_0d_{\text{SiN}_x}) \quad (3.9)$$

$$B_2 = -\frac{i}{n_{\text{SiO}_2}} \tan(n_{\text{SiO}_2}k_0d_{\text{SiO}_2}) - \frac{i}{n_{\text{SiN}_x}} \tan(n_{\text{SiN}_x}k_0d_{\text{SiN}_x}) \quad (3.10)$$

$$C_2 = -in_{\text{SiO}_2} \tan(n_{\text{SiO}_2}k_0d_{\text{SiO}_2}) - in_{\text{SiN}_x} \tan(n_{\text{SiN}_x}k_0d_{\text{SiN}_x}) \quad (3.11)$$

$$D_2 = 1 - \frac{n_{\text{SiO}_2}}{n_{\text{SiN}_x}} \tan(n_{\text{SiO}_2}k_0d_{\text{SiO}_2}) \cdot \tan(n_{\text{SiN}_x}k_0d_{\text{SiN}_x}) \quad (3.12)$$

As shown in Eq. (3.8), we can derive the substrate admittance \tilde{Y}_{sub} determined by the substrate parameters, and the condition of $\tilde{Y}_s = 1 - \tilde{Y}_{\text{sub}}$ achieves perfect absorption. In Figs. 3.11(c) and (d), the dotted black line is the $1 - \tilde{Y}_{\text{sub}}$, which will be called a critical line, as a function of the SiN_x thickness (d_{SiN_x}). This condition corresponds to the critical coupling induced by the interaction between the graphene plasmonic metasurface and the substrate. Or, we can interpret the perfect absorption as an admittance matching condition between the air and the load admittance \tilde{Y}_L , as shown in Eq. (3.8).

3.5.3 Critical Coupling

In the surface admittance charts, the perfect absorption is achieved at a crossing of the surface admittance and the critical line, and the magnitude of the surface admittance is strongly dependent on graphene carrier mobility, as shown in Fig. 3.13. With critical graphene carrier mobility ($\mu_{h,c}$), the surface admittance and substrate lines make a single critical coupling point at critical substrate thickness, where perfect absorption occurs.

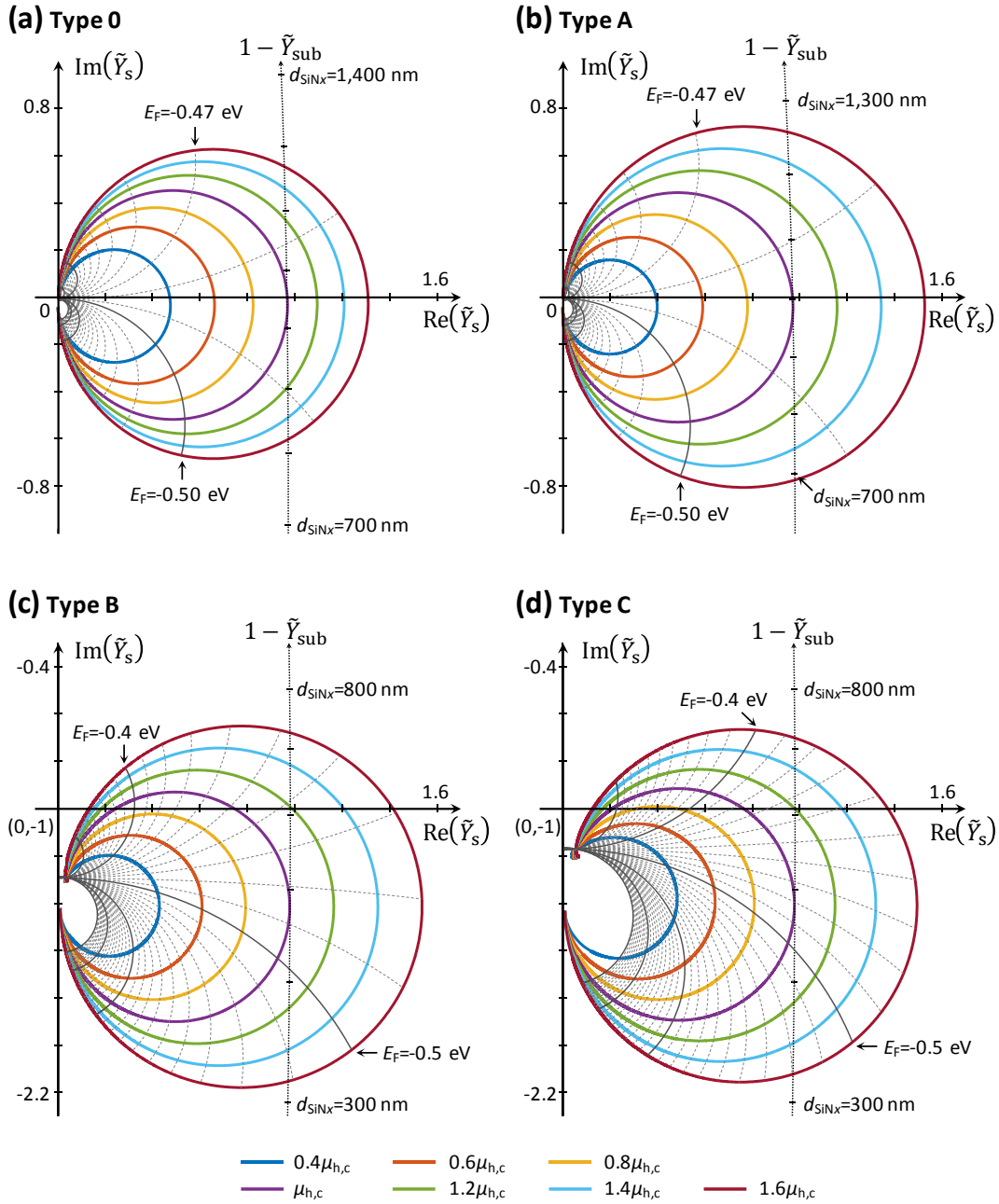


Figure 3.13 | Surface admittance chart. Surface admittance chart calculated by full-wave simulations of (a) the type 0 metasurface with $\mu_h=3,174 \text{ cm}^2\text{V}^{-1}\text{s}^{-1}$, (b) the type A metasurface with $\mu_h=2,271 \text{ cm}^2\text{V}^{-1}\text{s}^{-1}$, (c) the type B metasurface with $\mu_h=613 \text{ cm}^2\text{V}^{-1}\text{s}^{-1}$, and (d) the type C metasurface with $\mu_h=315 \text{ cm}^2\text{V}^{-1}\text{s}^{-1}$. The surface admittances are calculated from 0 eV to -20 eV of graphene Fermi level, and the equi- E_F lines from -0.4 eV to -0.8 eV with 0.01 eV steps (dotted grey lines) and 0.1 eV steps (solid grey lines). The frequency is $1,356 \text{ cm}^{-1}$ for all calculations.

If the graphene carrier mobility is lower than the critical graphene carrier mobility, the surface admittance line does not cross the critical line, and it corresponds to an undercoupled regime. When $\mu_h > \mu_{h,c}$, two critical coupling points exist and deviate from the critical substrate thickness [60]. In this regime, the resonance at the critical substrate thickness is overcoupled, which explains why the absorption declines after the perfect absorption in Fig. 3.8(a). The absorptions versus SiN_x thickness calculated by Eq. (3) dependent on the coupling conditions are summarized in Fig. 3.14, and they show good agreement with full-wave simulations.

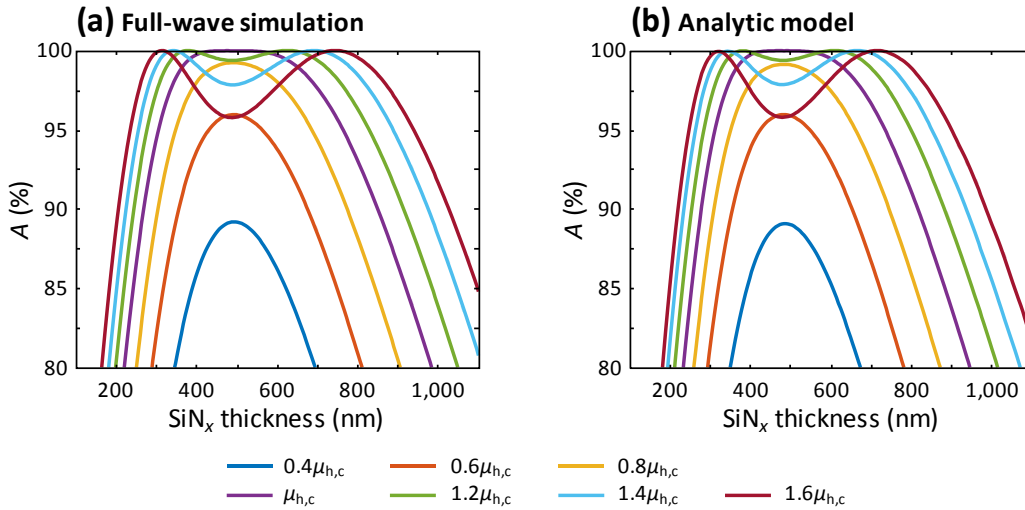


Figure 3.14 | Dependency on substrate thickness. Absorption in the type C device with different graphene carrier mobility (μ_h) as a function of SiN_x thickness calculated by (a) full-wave simulation and (b) analytic model.

This critical coupling can be also interpreted in terms of an admittance matching condition. Presenting the load admittance \tilde{Y}_L by $\tilde{Y}_s + \tilde{Y}_{\text{sub}}$, the condition of $\tilde{Y}_s = 1 - \tilde{Y}_{\text{sub}}$ corresponds to the load admittance matching to air admittance [123], which completely suppresses the reflection from the metasurface. Assuming there is no absorption in the dielectric stack with a perfect back reflector, the real part of the substrate admittance becomes zero, and only the imaginary part of the substrate admittance varies depending on the substrate thickness. Here, the role of the metasurface is to adjust the load admittance to have $\text{Re}(\tilde{Y}_s) = 1$, and the non-zero imaginary part of the \tilde{Y}_s induced by the coupled subwavelength metal slits, or the net susceptance, is compensated by the substrate admittance to match the load admittance to air. For weakly scattering metasurfaces with small $\text{Im}(\tilde{Y}_s)$ in the type 0 and A devices, the admittance matching condition is satisfied when the thickness of the substrate is equal to a quarter of the wavelength. On the other hand, in type B and

C devices, the $\text{Im}(\tilde{Y}_s)$ are fairly large even when the graphene resonators are off-resonant because the coupled noble metal slits significantly advance the phase of light passing through the metasurfaces. Due to this abrupt phase advance, admittance matching occurs for much thinner substrates compared to weakly scattering Salisbury screen.

As mentioned before, the critical line is defined by $1 - \tilde{Y}_{\text{sub}}$, where \tilde{Y}_{sub} is normalized substrate admittance, and is a function of substrate layer thickness. If there is zero absorption in a substrate layer with a perfectly conducting mirror back reflector, the Salisbury screen becomes lossless and the phase term varies depending on the substrate layer thickness. Therefore, the real part of \tilde{Y}_{sub} (the substrate conductance) should always be zero independent of the substrate thickness, and only the imaginary part of \tilde{Y}_{sub} (the substrate susceptance) depends on the substrate thickness. This makes the critical line vertical in a surface admittance chart. In practice, there is small absorption in the SiO_2 and the SiN_x layers due to phonon modes, and Au back reflector is not a perfect conductor. These small absorptions lead to a small conductance in \tilde{Y}_{sub} , resulting in a slight bending of the critical line and a shift in the real part of \tilde{Y}_{sub} away from zero.

The surface conductance, or the real part of the surface admittance, can be a measure of the oscillator strength in the graphene plasmonic metasurface. As shown in the surface admittance charts, the maximum surface conductance strongly depends on the graphene carrier mobility. This is mainly due to the fact that the higher graphene carrier mobility leads to inducing stronger graphene plasmonic resonances in the graphene plasmonic metasurfaces [117]. However, the stronger oscillator strength is not always preferable for achieving higher resonant absorption in the graphene plasmonic metasurfaces. As described in the manuscript, the ‘‘optimum’’ oscillator strength exist to accomplish the critical coupling between the metasurface and the substrate, or to match the load admittance to air. If the oscillator strength exceeds the optimum, the absorption becomes lower, and it is referred as over-coupling.

In a flat graphene sheet, the oscillator strength of graphene plasmonic resonance increases with higher graphene Fermi level because of large amount of free carriers interacting with photons. However, there is also an optimum graphene Fermi level in the GPRs to achieve stronger resonance because we have to consider the Fabry-Perot resonance in the finite size resonators [60]. Therefore, the surface conductance is maximized at a certain graphene Fermi level, and it declines above the optimum graphene Fermi level, as shown in the surface admittance charts.

If the graphene carrier mobility is larger than the critical graphene carrier mobility, the $\text{Re}(\tilde{Y}_s)$ exceeds one at the maximum resonance, which means the system is over-coupled to the free-space as its radiative damping rate is faster than its resistive damping rate [120]. Therefore,

the resonance has to be detuned to lower the optical conductance in the metasurface by adjusting the graphene Fermi level in order to satisfy the admittance matching condition. As we increase the graphene Fermi level from the resonance condition, the graphene plasmonic metasurface begins to advance the phase of light, and similarly phase retardation occurs for lower doping level as shown in Fig. 3.12. Consequently, as shown in Fig. 3.13, the device shows perfect absorption under two distinct admittance matching conditions: thinner substrate at high E_F , and thicker substrate at low E_F .

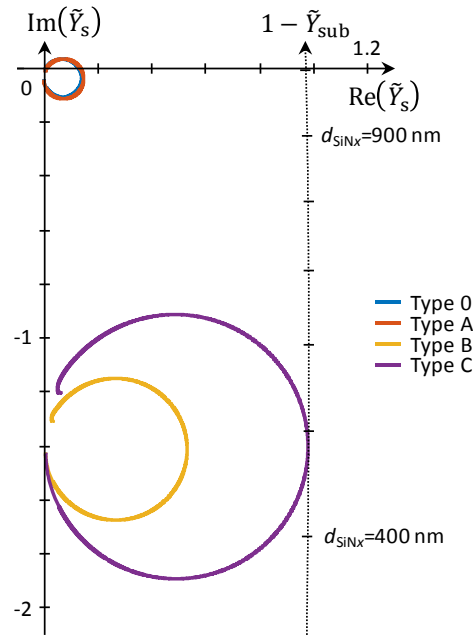


Figure 3.15 | Subwavelength metal slit effect on surface admittance. Surface admittance chart of all devices with $\mu_h=315 \text{ cm}^2\text{V}^{-1}\text{s}^{-1}$.

The surface admittance chart of all devices with $\mu_h=315 \text{ cm}^2\text{V}^{-1}\text{s}^{-1}$ is shown in Fig. 3.15, and the type C device exhibits the largest surface conductance. In addition, we observe that the type B and C devices are more inductive (or negatively larger surface susceptance) than the type 0 and A devices because of the strong noble metal plasmonic resonance induced by the subwavelength metal slits [126, 127].

3.5.4 Perfect Absorption with Lower Graphene Carrier Mobility

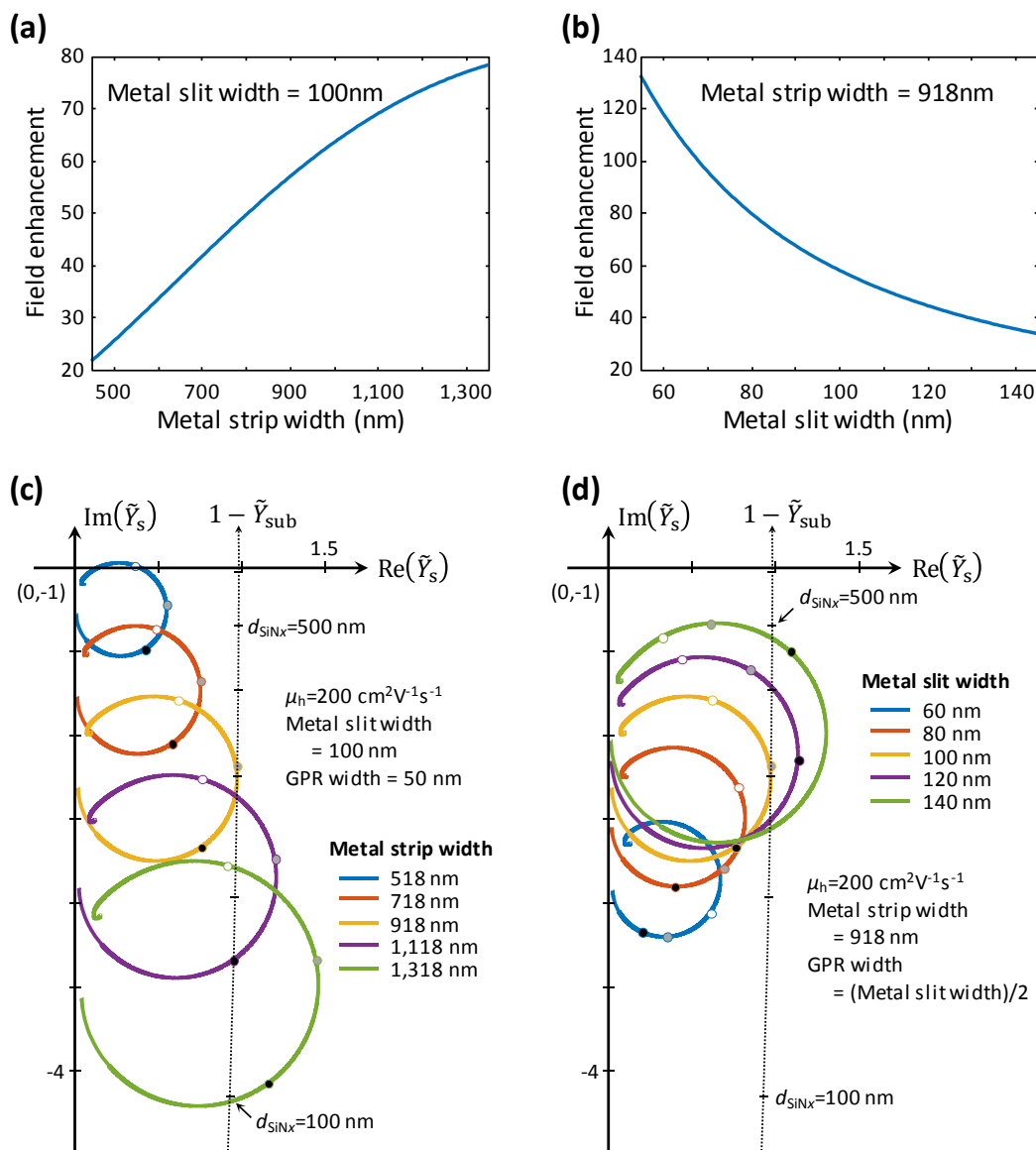


Figure 3.16 | Dependency on structural geometries. Field enhancement inside the subwavelength metal slit on SiO_2 150 nm/semi-infinite SiN_x substrate without intergap GPRs and (a) as a function of metal strip width and (b) as a function of metal slit width. Surface admittance charts of the type C metasurface calculated by full-wave simulations (c) with different metal strip width and (d) with different metal slit width. In c and d, the graphene carrier mobility is assumed as $200 \text{ cm}^2 \text{ V}^{-1} \text{ s}^{-1}$ for all calculations. The white, gray, and black dots in each surface admittance correspond to $E_F = -0.4 \text{ eV}$, $E_F = -0.5 \text{ eV}$, and $E_F = -0.6 \text{ eV}$, respectively. The frequency is $1,356 \text{ cm}^{-1}$ for all calculations.

By optimizing the subwavelength metal slit structure, we can achieve perfect absorption in the graphene plasmonic metasurface with even lower graphene carrier mobility. Fig. 3.16(a) and (b) show the field enhancement factor inside the subwavelength metal slits as a function of metal strip width and metal slit width, respectively. In Fig. 3.16(a), it is shown that wider metal strip width enhances the field enhancement factor because of the increased cross-section capturing more light. The enhanced field enhancement leads to more optically conductive metasurface, as shown in Fig. 3.16(c).

The narrower metal slit also improves the field enhancement factor by squeezing more light, as shown in Fig. 16(b). In the 1:2 ratio of the GPR width and the metal slit width, the narrower metal slits reduces the GPR width, and it results in weakening the oscillator strength in the GPR. As a result, the optical conductivity of the metasurface decreases with the narrower metal slit, as shown in Fig. 3.16(d). Although the wider metal slit would be beneficial in terms of the optical conductivity of the metasurface, it requires higher graphene Fermi level, which could not be achievable by electrostatic gating.

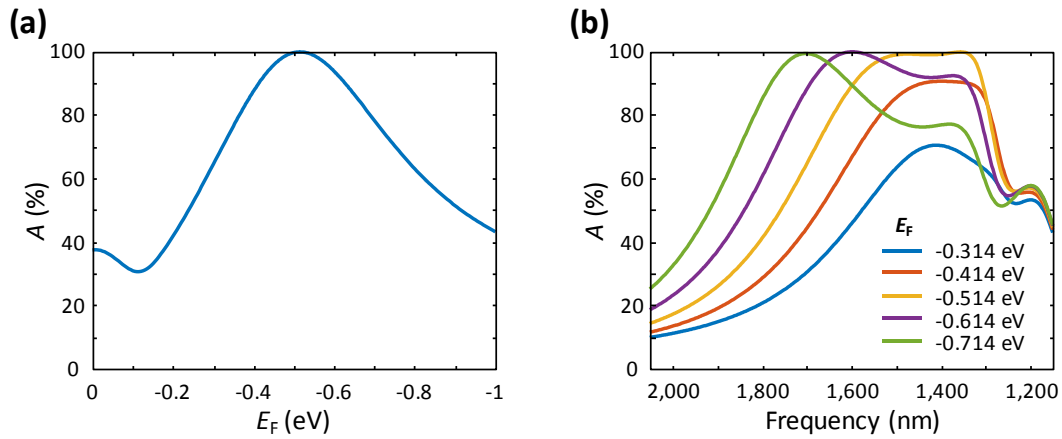


Figure 3.17 | Perfect absorption with lower graphene carrier mobility. (a) Tunable absorption at $1,356 \text{ cm}^{-1}$ in the optimized type C device as a function of graphene Fermi level (E_F) exhibiting the perfect absorption at $E_F = -0.514 \text{ eV}$. (b) Gate-dependent absorption spectra in the optimized type C device with different graphene Fermi level (E_F). In this optimized type C device, The GPR width, the metal slit width, the metal strip width, the SiO_2 thickness, and the SiN_x thickness are 50 nm, 100 nm, 918 nm, 150 nm, and 295 nm, respectively.

Figure 3.17 shows perfect absorption at $1,356 \text{ cm}^{-1}$ in the optimized type C device with $\mu_h = 200 \text{ cm}^2 \text{ V}^{-1} \text{ s}^{-1}$. The GPR width, the metal slit width, the metal strip width, the SiO_2 thickness, and the SiN_x thickness are 50 nm, 100 nm, 918 nm, 150 nm, and 295 nm, respectively. The perfect

absorption is shown with $E_F = -0.514$ eV, and this range is achievable in an electrostatic gating method. Compared to the other devices, the line shapes in graphene Fermi level and frequency are broader, as shown in Figs. 3.17(b) and (c). This broadening originates from the low Q-factor of the graphene plasmonic resonance with low graphene carrier mobility [117]. Further improvement should be possible by tuning the metal strip width and the SiN_x thickness, and it allows for the perfect absorption even with lower graphene carrier mobility.

3.6 Experimental Measurements

To measure the electronically tunable optical responses of the proposed devices, we fabricated the type A on SiO_2 150 nm/ SiN_x 1 μm membranes and the type B, and C devices on SiO_2 150 nm/ SiN_x 500 nm membranes. The top 150 nm layer of SiO_2 was deposited by e-beam evaporation (115 nm) and atomic layer deposition (35 nm). The Ti 3 nm/Au 100 nm layers were deposited on the back side of the membrane by e-beam evaporation, which performed as a back gate for doping graphene as well as a back reflector for the Salisbury screen. After transferring CVD-grown graphene onto the substrate, the GPRs were patterned by a 100 keV e-beam lithography system using a PMMA resist. With the patterned PMMA layer serving as a soft etch mask, the GPRs were cut by reactive ion etching with O_2 at 80 W for 15 s. The subwavelength metal slits were also patterned by e-beam lithography, and the Ti 2 nm/Au 80 nm layers were deposited by e-beam evaporation.

3.6.1 Characteristics of Graphene

The Raman signal of the CVD-grown graphene was measured on thermally grown SiO_2 substrate because of the strong photoluminescence emission of SiN_x over the visible range [128]. In Fig. 3.18(a), the G-peak and the 2D-peak are located at $1,591 \text{ cm}^{-1}$ and $2,693 \text{ cm}^{-1}$, respectively, and their ratio of $I_{2D}/I_G = 2.82$. The Raman spectrum shows that the D-peak ($1,350 \text{ cm}^{-1}$), which corresponds to defects in graphene, is very small, and the ratio of $I_G/I_D = 11.3$.

Figure 3.18(b) shows the gate-dependent resistance of the graphene exhibiting a charge neutral point at gate voltage $V_g = 261$ V for the type A device (SiO_2 150 nm/ SiN_x 1 μm) and at gate voltage $V_g = 183$ V for the type B and C devices (SiO_2 150 nm / SiN_x 500 nm). The graphene Fermi levels are calculated based on this charge neutral point using a capacitor model discussed in Section 2.2.4. In the capacitor model, the dielectric constants of SiO_2 and SiN_x were assumed as 5 and 10 [60, 117, 129], respectively.

Figures 3.18(c-e) show the graphene plasmon resonance frequencies of the type A, B, and C devices obtained by full-wave simulations and mid-infrared measurement results. In the type A device, the -0.08 eV of offset gives better agreement between simulation and the measurement results although good agreement is shown with less than 5% deviation without the offset. We expect that this offset originates from PMMA residue and trapped dopants beneath the graphene which induce local background doping in the GPRs of the type A device [89, 90].

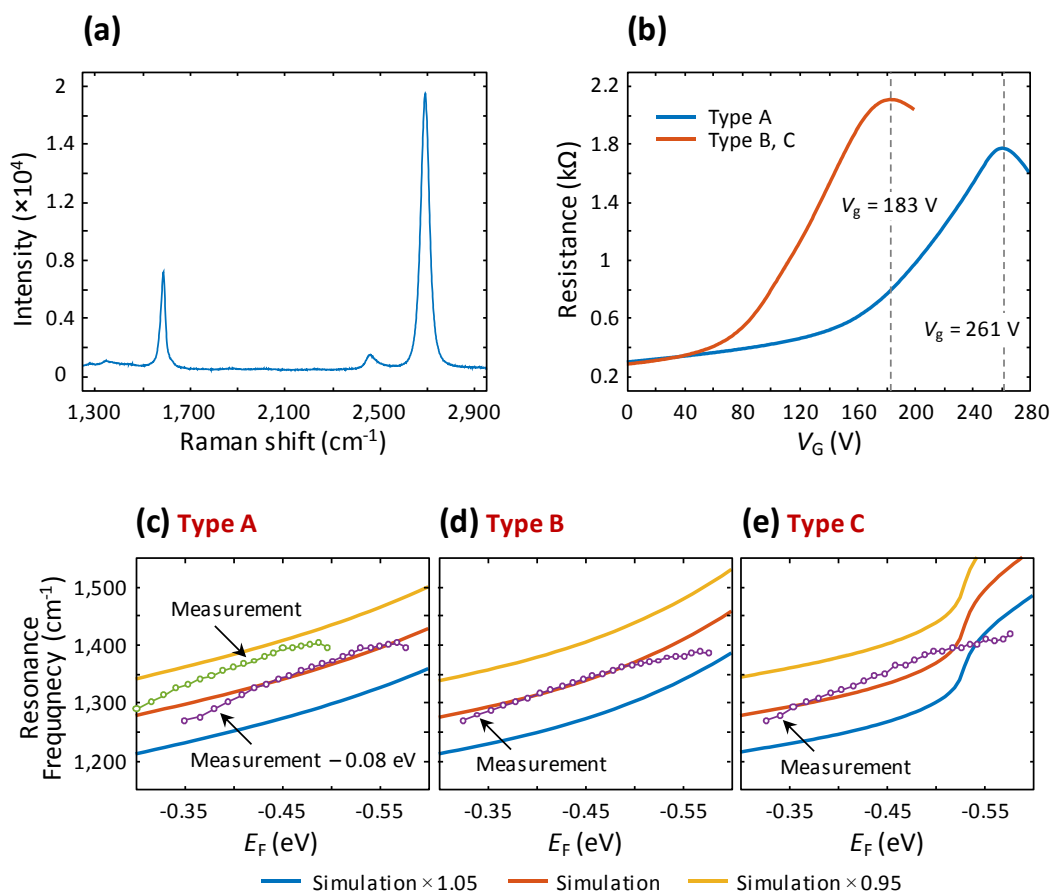


Figure 3.18 | Characteristics of experiment sample. (a) Raman spectrum of graphene transferred onto thermally grown SiO_2 substrate, and (b) gate-dependent resistance measurement of graphene on the SiO_2 150 nm / SiN_x 1 μm /Au substrate for the type A device and the SiO_2 150 nm / SiN_x 500 nm/Au substrate for the type B and C devices showing the charge neutral point at gating voltage $V_g=261$ V and $V_g=183$ V, respectively. Graphene plasmon resonance frequency of (c) type A, (d) type B, and (e) type C devices as a function of graphene Fermi level (E_F) for simulations and mid-infrared measurements. In c, the -0.08 eV of offset gives better agreement with simulation and measurement results.

In the type C device (Fig. 3.18(e)), the measured graphene plasmonic resonance frequencies and the simulations are in good agreement above $E_F = -0.53$ eV. However, the deviation between simulation and measurement increases below $E_F = -0.53$ eV, which we attribute to the pinning effect between the graphene/metal junctions [130] degrading the effective surface conductance at high frequencies, which result in suppression of the resonant absorption.

3.6.2 Mid-Infrared Measurements

To demonstrate the enhanced electronically tunable absorption in the GPRs coupled to the subwavelength metal slits, we measured the absorptions ($A = 1 - R$) for the type A, B, and C devices in a Fourier transform infrared (FTIR) microscope with a polarizer, and calculated the modulation efficiency in reflection ($\eta_R = 1 - R/R_{max}$). Here, R corresponds to the gate-dependent reflectance, and R_{max} is the reflectance when the absorption is minimized at a certain graphene Fermi level between the interband absorption and the graphene plasmonic resonance.

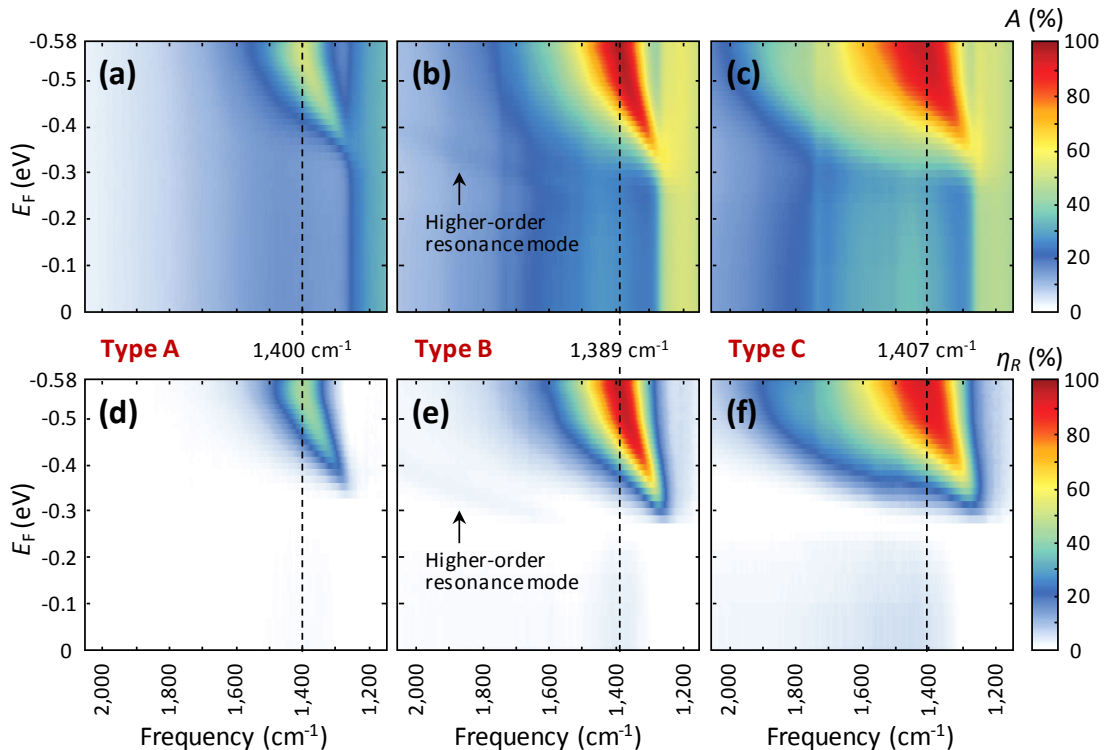


Figure 3.19 | Mid-infrared measurements. (a-c) Gate-dependent tunable resonant absorption spectra in the type A, B, and C devices, respectively, and (d-f) corresponding modulation efficiencies (η_R) calculated based on the first blue lines.

	Type A	Type B	Type C
Frequency	1,400 cm^{-1}	1,389 cm^{-1}	1,407 cm^{-1}
Maximum absorption / E_F	52.4% / -0.550 eV	96.9% / -0.568 eV	94.8% / -0.560 eV
Minimum absorption / E_F	14.0% / -0.316 eV	24.8% / -0.262 eV	29.6% / -0.262 eV
Modulation efficiency (η_R)	44.6%	95.9%	92.6%

Table 3.2 | Summary of measurement results.

Figures 3.19(a-c) show the gate-dependent tunable absorption spectra, and corresponding modulation efficiencies are shown in Figs. 3.19(d-f). Table 3.2 summarizes the measurement results for the type A, B, and C devices. In the type B device, we also observed the higher-order graphene plasmonic resonance mode [51, 131], which is not easily observable in bare GPRs devices with low graphene carrier mobility.

Figure 3.20(a) summarizes the measured absorptions as a function of graphene Fermi level, and corresponding modulation efficiencies are presented in Fig. 3.20(b). As shown by the measurement results, the coupled subwavelength metal slits significantly enhance the absorption in the GPRs, and both the type B and C devices display nearly perfect absorption. In addition, the type A device enables higher tunability than previously measured type 0 device [60], which indicates the low permittivity substrate improves coupling efficiency between free-space photons and graphene plasmons.

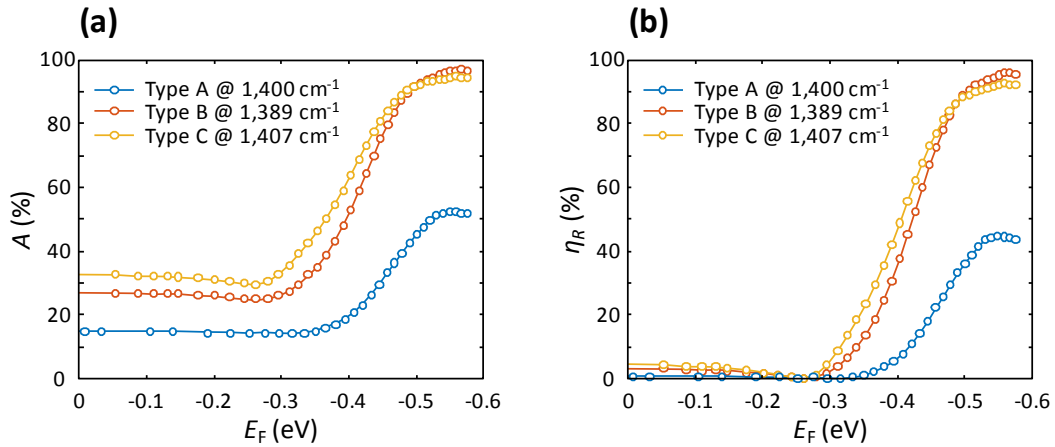


Figure 3.20 | Measurement summary. (a) Absorption comparison and (b) modulation efficiency comparison as a function of graphene Fermi level (E_F) at the frequency exhibiting the maximum absorption in each device.

3.6.3 Numerical Fitting

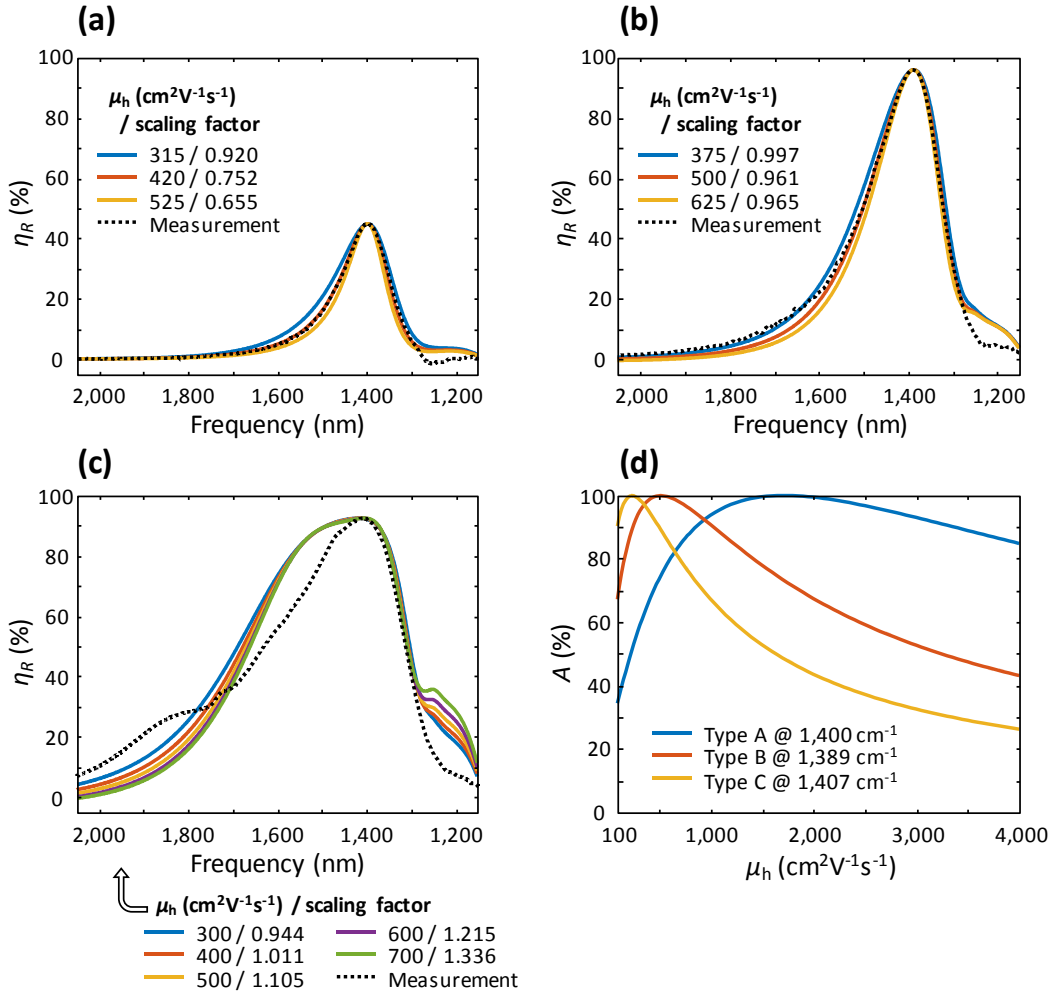


Figure 3.21 | Numerical fitting. Numerical fitting results of modulation efficiencies in (a) type A, (b) type B, and (c) type C devices. The graphene carrier mobilities and scaling factors for each device are presented in the figure legends. (d) Absorption as a function of graphene carrier mobility (μ_h) at the frequencies showing the maximum absorption in each device. The required graphene carrier mobilities for the type A, B, and C devices at their graphene plasmonic resonance frequencies are 1,718 $\text{cm}^2\text{V}^{-1}\text{s}^{-1}$, 521 $\text{cm}^2\text{V}^{-1}\text{s}^{-1}$, and 243 $\text{cm}^2\text{V}^{-1}\text{s}^{-1}$, respectively.

Mid-infrared measurements demonstrate that low permittivity substrates and coupled subwavelength metal slits play pivotal roles in enhancing the resonant absorption in GPRs. To analyze the measurement data, we tuned the graphene carrier mobilities in simulations to match the lineshape of the modulation efficiency spectra, and scaling factors were adopted to adjust the maximum modulation efficiencies in simulation to the measured ones [117], as shown in Fig. 3.21. In the simulations, we also considered the finite NA (0.58) of the objective lens in the FTIR

measurements. Here, we expect that the estimated graphene carrier mobility includes defects in graphene and edge roughness in the ribbons, and the scaling factor considers electrically dead resonators in the GPRs and the finite NA effect in the measurement.

In the type A device, the estimated graphene carrier mobility was $420 \text{ cm}^2\text{V}^{-1}\text{s}^{-1}$, and the scaling factor was 0.752. In the type B device, the estimated graphene carrier mobility of $500 \text{ cm}^2\text{V}^{-1}\text{s}^{-1}$ and the scaling factor of 0.961 show good agreement between the simulation and the measurement results. In practice, the width of each GPR could be slightly different due to small non-uniformities in pattern fabrication, and the spectra would suffer from inhomogeneous broadening, or an ensemble averaging effect. The type A device has more GPRs than the type B device per unit area, thus the ensemble averaging effect should be more significant in the type A device, broadening the spectral width of the collective graphene plasmonic resonances, which can be modeled by lowering effective graphene carrier mobility. In addition, the coupled metal strips are expected to lower the chance of electrical disconnections in the GPRs, which increases the scaling factor in the type B device. At the resonant frequencies exhibiting the highest absorption in each device, the required graphene carrier mobilities for perfect absorption are $1,718 \text{ cm}^2\text{V}^{-1}\text{s}^{-1}$ and $521 \text{ cm}^2\text{V}^{-1}\text{s}^{-1}$ for the type A and B devices, respectively, as shown in Fig. 3.21(d). This indicates the interaction between the substrate and GPRs are in the under-coupled regime in the type A device, and the type B device is closely located at the critical coupling, which results in nearly perfect absorption in the latter.

3.7 Conclusions

In summary, we demonstrated the enhanced electronically tunable resonant absorption in graphene plasmonic metasurface consisting of GPRs coupled to noble metal plasmonic light focusing structures. We showed that the coupled subwavelength metal slits are the key factor for perfect absorption in the GPRs to overcome low graphene carrier mobility limits. In addition, we formulated a rigorous model based on surface admittance to analyze the tunable resonance in the graphene plasmonic metasurface, and elucidated that the perfect absorption is achieved when the interaction between the graphene plasmonic metasurface and the substrate induces critical coupling to free-space. Using the surface admittance analysis, we account for the roles of the graphene plasmonic metasurface and the substrate in an admittance matching condition. In mid-infrared measurements, a maximum absorption of 96.9% was achieved at $1,389 \text{ cm}^{-1}$ with a corresponding modulation efficiency of 95.9%. These results pave the way for realizing tunable perfect light modulation by graphene plasmonic resonances coupled to noble metal plasmonic resonances.

CHAPTER 4

ELECTRONICALLY TUNABLE EXTRAORDINARY OPTICAL TRANSMISSION IN GRAPHENE PLASMONIC RIBBONS COUPLED TO SUBWAVELENGTH METALLIC SLIT ARRAYS

Subwavelength metallic slits arrays have been shown to exhibit extraordinary optical transmission, whereby tunneling surface plasmonic waves constructively interfere to create large forward light propagation. The intricate balancing needed for this interference to occur allows for resonant transmission to be highly sensitive to changes in the environment. Here we demonstrate that extraordinary optical transmission resonance can be coupled to electrostatically tunable graphene plasmonic ribbons to create electrostatic modulation of mid-infrared light. Absorption in graphene plasmonic ribbons situated inside metallic slits can efficiently block the coupling channel for resonant transmission, leading to a suppression of transmission. Full wave simulations predict a transmission modulation of 95.7% via this mechanism. Experimental measurements reveal a modulation efficiency of 28.6% in transmission at $1,397\text{ cm}^{-1}$, corresponding to a 2.67 fold improvement over transmission without a metallic slit array. This work paves the way for enhancing light modulation in graphene plasmonics by employing noble metal plasmonic structures.*

* This chapter is reproduced with some modifications from the manuscript “S. Kim *et al.* Electronically tunable extraordinary optical transmission in graphene plasmonic ribbons coupled to subwavelength metallic slit arrays. *Nat. Commun.* **7**, 12323 (2016)”.

4.1 Introduction

Significant efforts have been made in the past 5 years to create graphene plasmon-based optical modulators that function from THz to mid-infrared frequencies. These devices have exploited the unique plasmon dispersion relation of graphene, which exhibits optical modes with high confinement factors [41-43, 56, 57, 132], and that are electrostatically tunable [35, 46]. Typically, these devices have been based on geometries that employ resonant absorption in graphene nanostructures that have been patterned to confine plasmonic modes that can be electrostatically tuned to control the intensity and frequency of either optical absorption or emission [51, 59, 60, 99-103, 105, 106, 108, 133-135]. However the single layer atomic thickness and low free carrier density of graphene have limited the efficiencies of such modulators, especially at mid-infrared frequencies, where the oscillator strength of the graphene plasmonic modes is low. A number of strategies have been adopted to overcome these difficulties, including using ionic gel or chemical doping to increase the carrier density of the graphene sheet [92, 99, 105, 107], or carefully controlling the substrate to include a metallic back reflector, which creates additional optical resonances that enhance field intensities at the graphene plasmonic ribbons (GPRs) [59, 60, 107, 133], and thus enhance absorption. While those techniques can have theoretical modulation efficiencies of 100%, the use of ionic gels places significant restraints on the applicability, switching speeds, and durability of such devices, and the use of metallic reflectors forces those devices to be used in reflection geometries. In contrast to the reflective type graphene plasmonic modulators, a strategy of using electrostatically tunable graphene plasmons to modulate transmitted light with near-unity efficiency has not yet been reported, to the best of our knowledge. The creation of such a device would have widespread applications in optoelectronic devices such as mid-infrared spatial light modulators, or linear signal processing [12, 136, 137].

In this chapter, we report an approach to use graphene plasmonic modes for light modulation in a transmission geometry that satisfies the above conditions: high modulation efficiency at carrier densities accessible with electrostatic gating. Our modulator design is based on a triple resonant structure, where the plasmonic resonances in graphene plasmonic ribbon are matched to a dielectric substrate Fabry-Perot resonance, and also to the optical resonances in a subwavelength metallic slit array which is designed to exhibit extraordinary optical transmission (EOT) in the mid-infrared. In full wave simulations, the proposed structure shows 95.7% modulation efficiency in transmission. We measured a mid-infrared transmission modulation efficiency of 28.6% at $1,397\text{ cm}^{-1}$, which is 2.67 times higher than that measured for an equivalent GPRs only structure on the same supporting dielectric structure.

4.2 Device Geometry and Light Modulation Mechanism

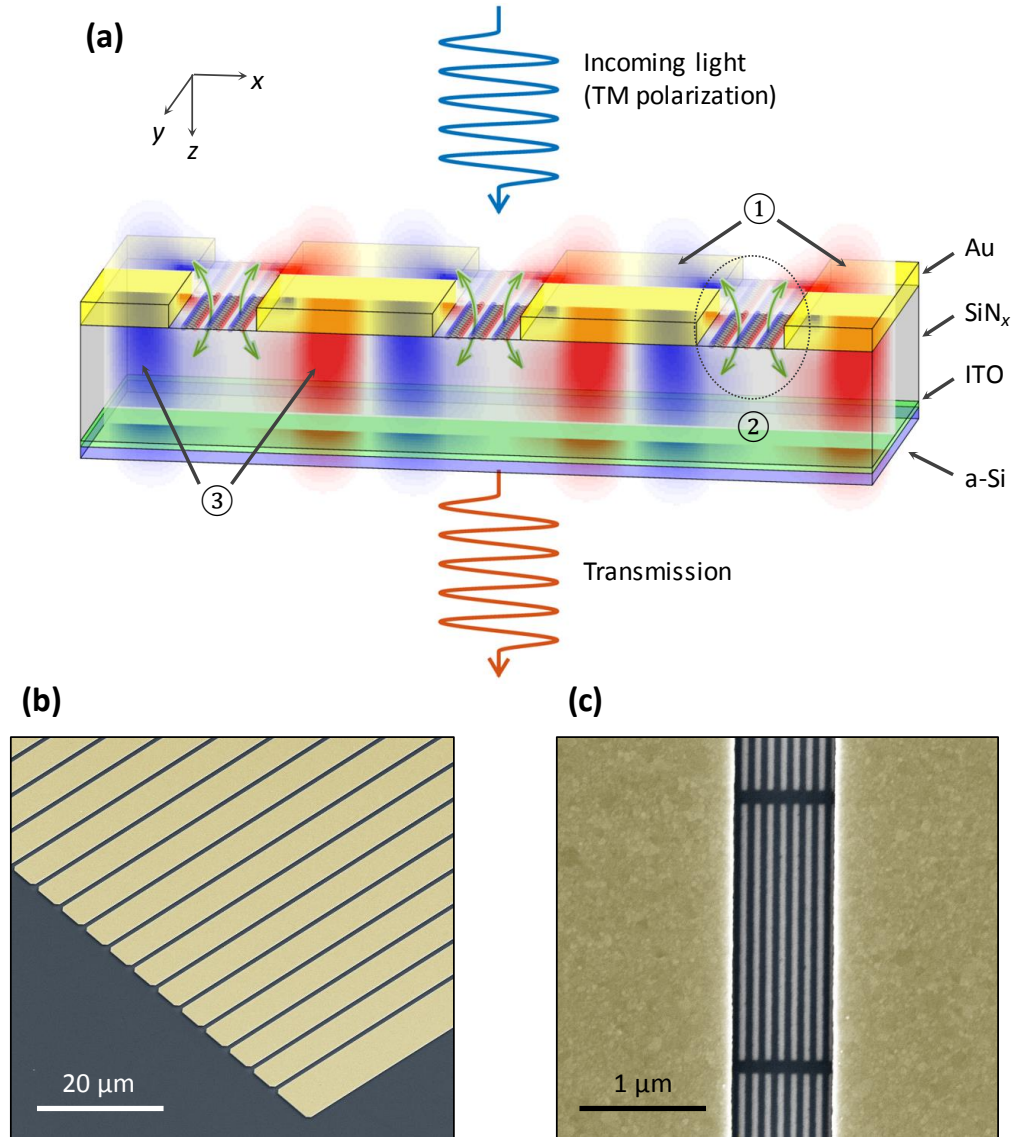


Figure 4.1 | Device and working mechanism. (a) Schematic of the GPRs coupled to subwavelength metallic slit array. Under normal operation (i.e. no GPRs), transverse magnetic (TM) polarized incoming light induces surface plasmons on the top metal surface (①) that tunnel through the subwavelength metallic slits (②), exciting surface plasmons (③) on the bottom metal surface. The surface plasmons on the bottom metal surface are diffracted by the periodic structure and radiate into free space with an enhanced intensity. The role of the GPRs inside the subwavelength metal slits is to block the coupling channel (②), and leading to a suppression of the EOT effect. In this figure, the overlapping field distribution depicts $\text{Re}(E_z)$ for the surface plasmons, and the scale is adjusted to fit the schematic. SEM images (false color) of (b) the subwavelength metallic slit array and (c) the GPRs inside the subwavelength metallic slit fabricated on SiN_x membrane.

Figure 4.1(a) shows the mechanism of the proposed device. In EOT, incoming light is scattered by the periodic structure into surface plasmons on the top metal surface. The surface plasmons then tunnel through the subwavelength metallic slits and excite surface plasmons on the bottom metal surface. The surface plasmon on the bottom metal surface subsequently re-radiates into free space, resulting in a transmitted diffraction peak with a strong intensity at the EOT resonance frequency [23-27, 138]. The subwavelength metallic slits play a pivotal role in EOT via optical coupling between the surface plasmons on the top and bottom metal surfaces. In our modulator, GPRs are placed in the subwavelength metallic slits in order to modulate the EOT resonant coupling. This is accomplished by electrostatically tuning the plasmonic resonances in GPRs to match the resonant frequency of the EOT. When matched, the electric fields in the subwavelength metallic slits give rise to large plasmonic resonance in the GPRs, which leads to blocking the coupling channel for the EOT resonance. As a result, a strong suppression of EOT occurs. To demonstrate this modulation mechanism, we fabricated subwavelength metallic slit array structures with GPRs on SiN_x membranes, as shown in Figs. 4.1(b) and (c). In Fig. 4.1(c), the dark stripes denote the GPRs, and the bright bar corresponds to the etched region that defines the GPRs.

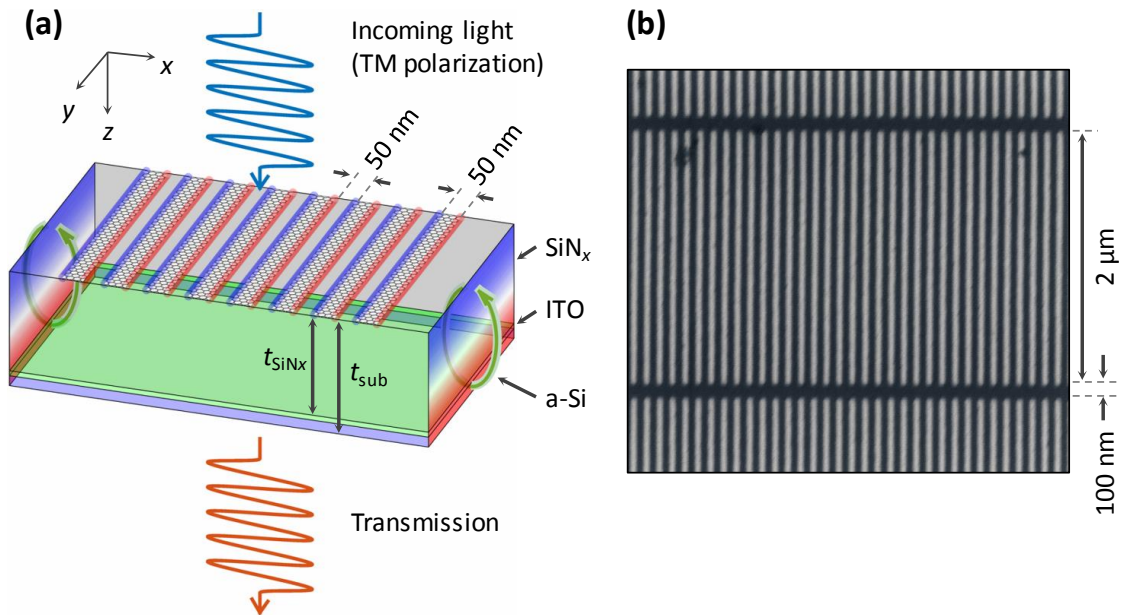


Figure 4.2 | Bare graphene plasmonic ribbons. (a) Schematic of a transmission type bare GPR modulator. Field distributions on the side walls correspond to $\text{Re}(E_x)$ showing the Fabry-Perot resonance in the substrate. (b) SEM image of bare GPRs fabricated on SiN_x membrane. The fabricated GPRs form a mesh to prevent electrical disconnection with $2 \mu\text{m}$ length and 100 nm bridge. The width and the gap of the GPRs are both 50 nm .

Figure 4.2(a) shows the schematic of the equivalent GPRs only structure on the same supporting dielectric structure as a control sample, and the SEM image of the fabricated device is shown in Fig. 4.2(b).

4.3 Substrate Geometry Optimization

To achieve electronically tunable transmission, the substrate must be transparent at the operating frequency, yet also allow for electrostatic gating. Additionally, the substrate will support Fabry-Perot type resonances, which can lead to constructive or destructive interference effects that modify the electric field intensities on the top surface and thus the absorption in the GPRs. In order to satisfy these constraints, we use a 2 μm SiN_x membrane (Norcada, NX10500N) with a DC conducting indium-tin-oxide (ITO, 4 nm) / a-Si (60 nm) contact on the bottom side of the membrane, as shown in Fig. 4.1(a). The DC conducting contact was deposited on the bottom side of the SiN_x membrane by RF sputtering at room temperature. The RF sputtering powers for the ITO and the a-Si were 48 W and 150 W, respectively.

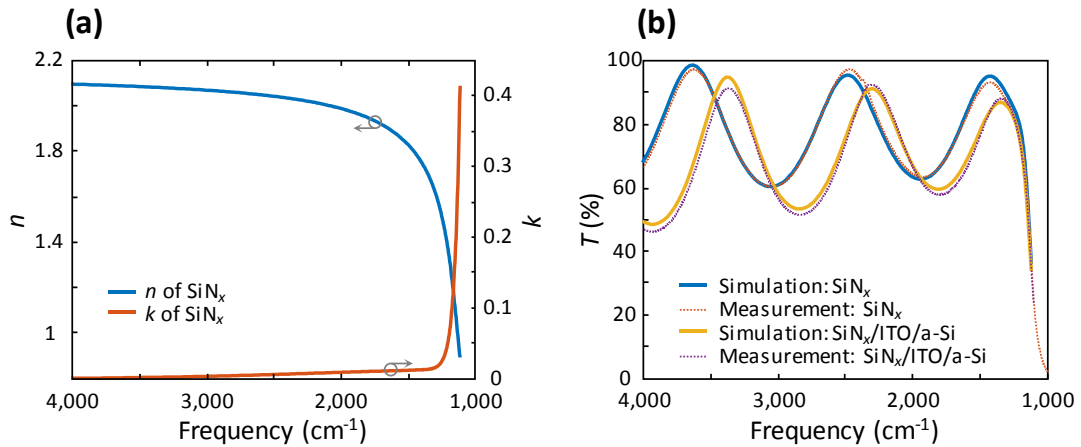


Figure 4.3 | Characteristic of membrane. (a) Refractive index of SiN_x measured by mid-infrared ellipsometry. (b) Transmission spectra for a single SiN_x 2 μm membrane and a SiN_x membrane with transparent back contact (ITO 4 nm / a-Si 60 nm). The solid lines are simulation results, and the dotted lines were obtained by a mid-infrared transmission measurement.

The frequency dependent dielectric function of SiN_x was measured using mid-infrared ellipsometry, as shown in Fig. 4.3(a). For ITO, we used tabulated data [139]. In the case of a-Si, we scaled a-Si data from Palik data [17] by a weighting factor of 0.88, which reflects the optical characteristic difference depending on the sputtering condition, such as temperature and RF power

[140]. Transmission spectra of a single SiN_x membrane and the SiN_x membrane with the DC conducting contact were measured using a Fourier transform infrared (FTIR) microscope, as shown in Fig. 4.3(b), and it is shown that the DC conducting layer induces redshift in transmission spectra.

To optimize the substrate thickness for maximizing absorption in GPRs, we performed full wave simulations for an array of bare 50 nm wide GPRs, varying the SiN_x thickness. The calculations were performed at $\lambda^{-1}=1,340 \text{ cm}^{-1}$, which is the resonant frequency of 50 nm GPRs for $E_F=-0.465 \text{ eV}$, and a graphene carrier mobility (μ_h) of $15,000 \text{ cm}^2\text{V}^{-1}\text{s}^{-1}$ was assumed for the graphene sheet [35]. Here, the negative sign of E_F denotes that the graphene is hole doped.

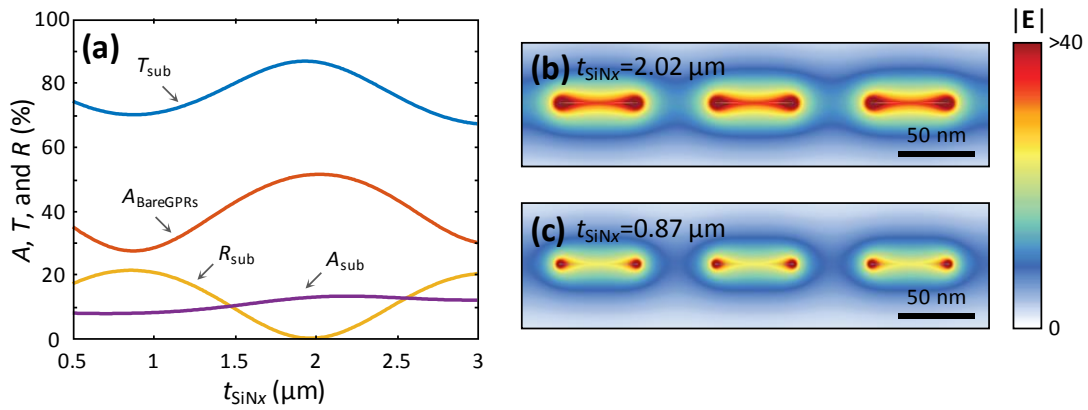


Figure 4.4 | Resonance in a substrate. (a) The red line indicates absorption in the bare graphene plasmonic ribbons (GPRs) device depending on the SiN_x thickness (t_{SiN_x}) with the graphene Fermi level position $E_F=-0.465 \text{ eV}$. The blue, yellow, the purple lines correspond to transmittance, reflectance, and absorption, respectively, depending on the SiN_x thickness through the $\text{SiN}_x/\text{ITO}/\text{a-Si}$ substrate without the GPRs. Total electric field distributions around the bare GPRs at the $E_F=-0.465 \text{ eV}$ with the SiN_x thickness of (b) $2.02 \mu\text{m}$ and (c) $0.87 \mu\text{m}$.

As shown in Fig. 4.4(a), the transmission spectrum exhibits a Fabry-Perot resonance that depends on the SiN_x thickness (t_{SiN_x}), and leads to variation in plasmonic absorption by GPRs. In contrast to GPR reflection modulators that achieve maximum absorption at $t_{\text{sub}}=\lambda/4n_{\text{sub}}$ [59, 60], the absorption for transmission modulators has a maximum at $t_{\text{sub}}=\lambda/2n_{\text{sub}}$ with $t_{\text{SiN}_x}=2.02 \mu\text{m}$, and the minimum occurs at $t_{\text{sub}}=\lambda/4n_{\text{sub}}$ with $t_{\text{SiN}_x}=0.87 \mu\text{m}$ (t_{sub} : substrate thickness, t_{SiN_x} : SiN_x thickness, n_{sub} : effective refractive index of substrate). Considering this structure as a Fabry-Perot cavity, the maximal absorption point corresponds to transmission resonance in the forward direction, as shown Fig. 4.3(b). This effect arises from the zero phase shift for light reflected from the bottom a-Si/air interface. These reflected waves constructively interfere with incident light when the reflection path length is $2t_{\text{sub}}=\lambda/n_{\text{sub}}$, which corresponds to 2π in terms of the phase difference. As a result, a

standing wave is formed in the substrate with a maximum on the surface, which leads to enhanced absorption in GPRs. We also observe that the near field intensities around GPRs are enhanced at resonance, as shown in Figs. 4.4(b) and (c).

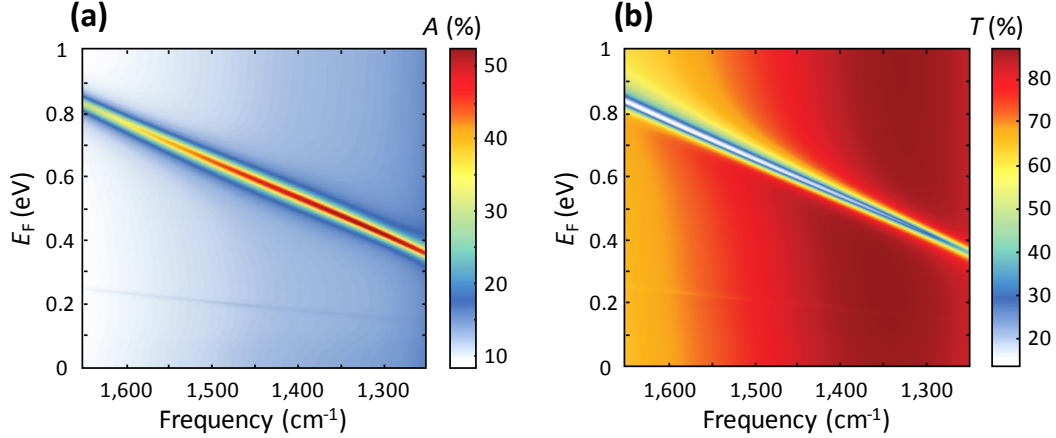


Figure 4.5 | Graphene plasmonic ribbons. (a) Absorption and (b) transmittance in bare GPRs device as a function of frequency and E_F with $t_{\text{SiN}_x}=2 \mu\text{m}$.

To further characterize the device, we calculate the spectral absorption as a function of graphene Fermi level position (E_F) for a $2 \mu\text{m}$ layer of SiN_x , as shown in Fig. 4.5(a). In the absence of substrate resonances, a higher doping level, by itself, leads to strong oscillator strength in the GPRs, and thus enhances plasmonic absorption [51, 101, 105]. However, in this device the absorption is strongest at $\lambda^{-1}=1,340 \text{ cm}^{-1}$, which occurs not for maximal doping level, but when the plasmonic resonance in GPRs and substrate resonance are matched, as shown Fig. 4.5(a). As a result, transmission declines along the plasmonic absorption in GPRs, as shown in Fig. 4.5(b).

4.4 Theoretical Modulation of Coupled Structure

4.4.1 Light Modulation in Coupled Structure

In the proposed coupled structure, GPRs are located inside subwavelength metallic slits to modulate the coupling between the surface plasmon modes on the top and bottom metal surfaces. Four parameters dictate the subwavelength metallic slit array design: the metallic material, metal thickness, slit width, and period in transverse direction, as shown in Fig. 4.1(a). We used Au with a thickness of 80 nm, and the subwavelength metallic slit width is 800 nm, which can support eight GPRs inside each metallic slit. For a given subwavelength metallic slit width, the EOT resonance

frequency is determined by the subwavelength metallic slit array period. A period of $5.54 \mu\text{m}$ is used in simulation to match an EOT peak at $\lambda^{-1}=1,340 \text{ cm}^{-1}$.

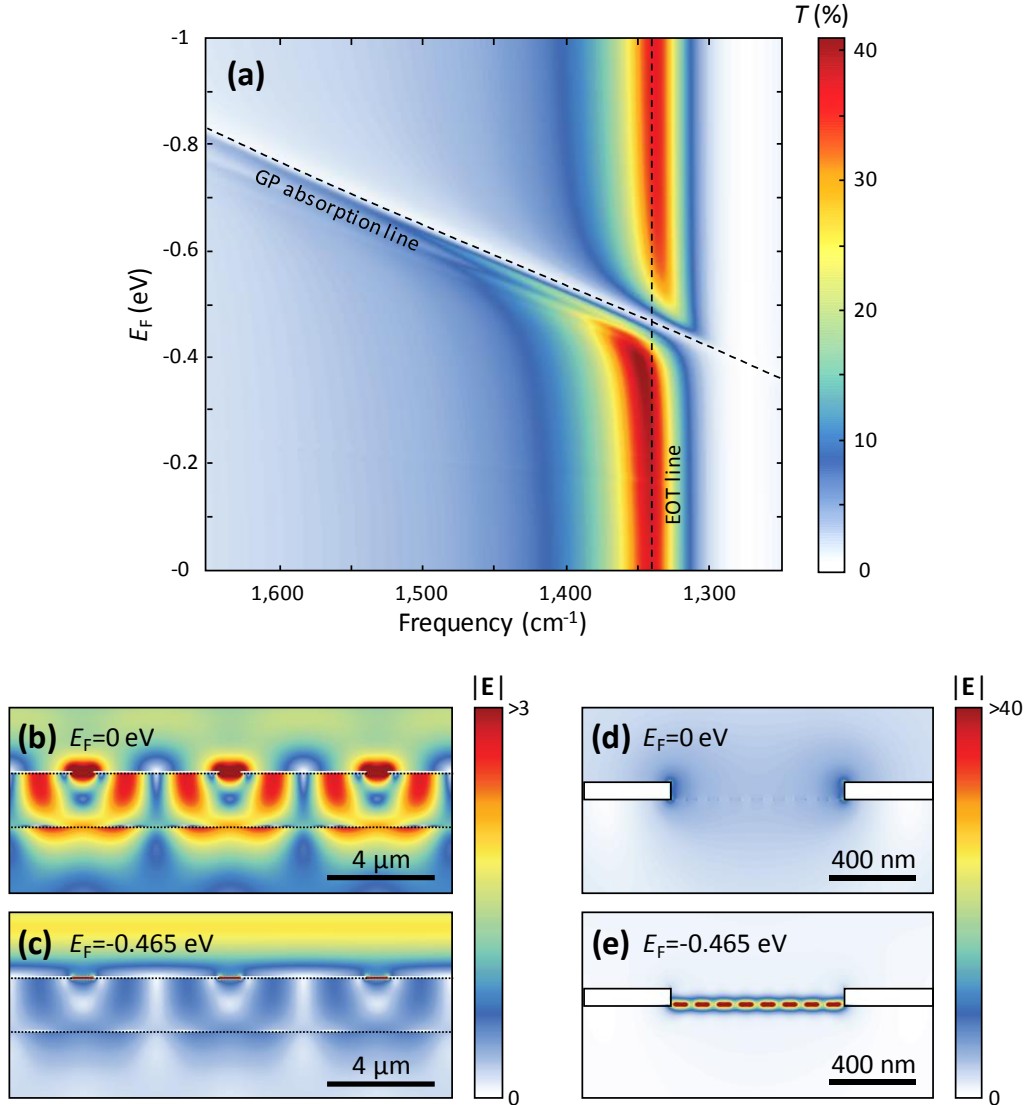


Figure 4.6 | Coupled structure simulations. (a) Transmittance map exhibiting graphene plasmon (GP) absorption and EOT as a function of frequency and graphene Fermi level (E_F). (b-e) Total electric field distributions when turning the graphene plasmons off ($E_F=0 \text{ eV}$) and on ($E_F=-0.465 \text{ eV}$) at $\lambda^{-1}=1,340 \text{ cm}^{-1}$.

After combining the GPRs and the subwavelength metallic slit array, the 0th order transmittance (T) as a function of frequency and E_F is shown in Fig. 4.6(a). When the plasmonic resonance in GPRs deviates from the EOT resonance frequency, the subwavelength metallic slit array exhibits resonant transmission. However when the GPRs are gated such that plasmonic

resonance in GPRs matches the EOT resonance ($E_F = -0.465$ eV), there is a strong dip in the transmission spectrum at the crossing between two resonant modes, as shown in Fig. 4.6(a). The total electric field distributions on and off the plasmonic resonance in GPRs are shown in Figs. 4.6(b-e). When the plasmonic resonance in GPRs is detuned from the EOT mode, we observe a metallic surface plasmon mode on the bottom metal surface and confined fields inside the subwavelength metallic slits, indicating coupling between the two surface plasmon modes (Figs. 4.6(b) and (d)). In contrast, as the plasmonic resonance in GPRs is tuned to the EOT frequency ($E_F = -0.465$ eV), both the metallic surface plasmon modes on the bottom metal surface and inside the subwavelength metallic slits are diminished significantly (Fig. 4.6(c)) because the coupling channel is blocked through interaction with the intergap GPRs (Fig. 4.6(e)).

4.4.2 Dependency on Graphene Carrier Mobility

To evaluate the modulation performance, we compare modulation efficiencies of the bare GPRs and graphene plasmonic ribbons combined with the subwavelength metallic slit array (GPRs-EOT). Here, modulation efficiency in transmittance (η_T) is defined by $1 - T/T_{\max}$, where T is transmittance as a function of E_F , and T_{\max} corresponds to the transmission spectrum for the graphene Fermi level position that maximizes the transmitted intensity at the resonant frequency. In this simulation for GPRs, the T_{\max} occurs at $E_F = -0.310$ eV, where there is sufficient doping to prevent graphene inter-band absorption, but insufficient carrier density to support plasmonic modes in the GPRs.

Figure 4.7(a) shows that, for high carrier mobility graphene ($\mu_h = 15,000$ cm²V⁻¹s⁻¹), the coupled structure shows a moderate improvement over the bare GPRs, with the theoretical maximum modulation efficiency increasing from $\eta_T = 74.5\%$ to 95.7% . As the graphene carrier mobility is lowered, the overall modulation efficiency decreases in both devices. However, the relative benefits of the GPRs-EOT structure are enhanced with lower graphene carrier mobility, as shown in Fig. 4.7(a) and (b). For example, at $\mu_h = 3,000$ cm²V⁻¹s⁻¹ the modulation efficiency of the bare GPRs is 50.6% , while the GPRs-EOT structure achieves 85.9% efficiency, and for $\mu_h = 1,000$ cm²V⁻¹s⁻¹ these values change to 27.3% and 65.2% , respectively. Thus the GPRs-EOT structure can exhibit large transmission modulation and is more robust against ribbon disorder compared to bare GPR based devices.

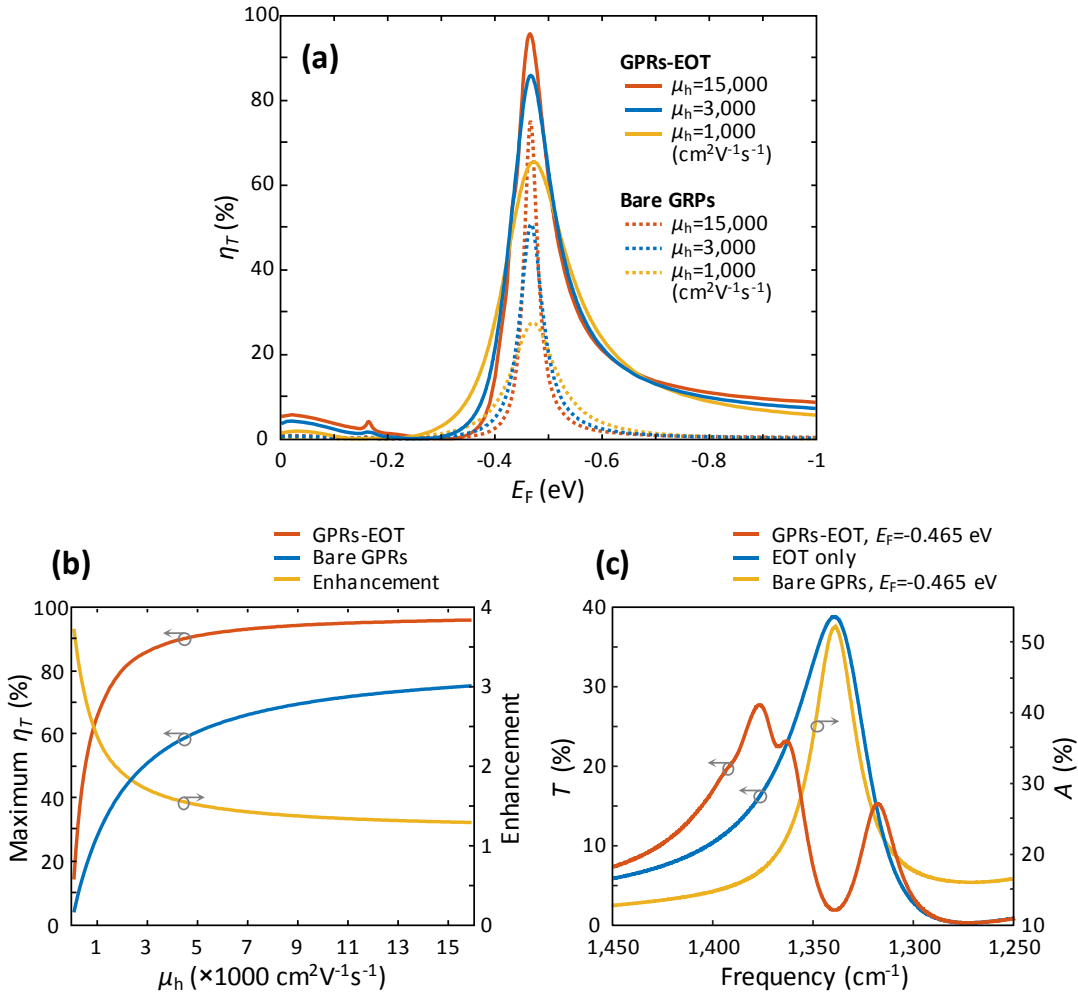


Figure 4.7 | Light modulation in transmission. (a) Comparison of modulation efficiency in transmission (η_T) between the bare GPRs device and the coupled structure (GPRs-EOT) device as a function of graphene Fermi level (E_F) with different graphene carrier mobilities (μ_h). (b) Maximum modulation efficiency in transmission of bare GPRs and GPRs-EOT as a function of graphene carrier mobility (μ_h). The enhancement factor is calculated from the ratio of the maximum modulation efficiencies. (c) Anti-crossing behavior (red line) by strong coupling between the EOT resonance without GPRs (blue line) and the resonance in bare GPRs (yellow line). The “EOT only” indicates the subwavelength metallic slit array without GPRs.

4.5 Anti-Crossing Behavior in Coupled Structure

Modulation can be interpreted qualitatively using an effective medium theory that considers plasmonic modes in the subwavelength metallic slit array coupled to deeply subwavelength GPRs. There is significant spatial overlap between the plasmonic modes in GPRs and the EOT modes of the subwavelength metallic slit array, such that plasmonic resonances in

GPRs can alter the local dielectric environment experienced by EOT modes when the two frequencies approach one another.

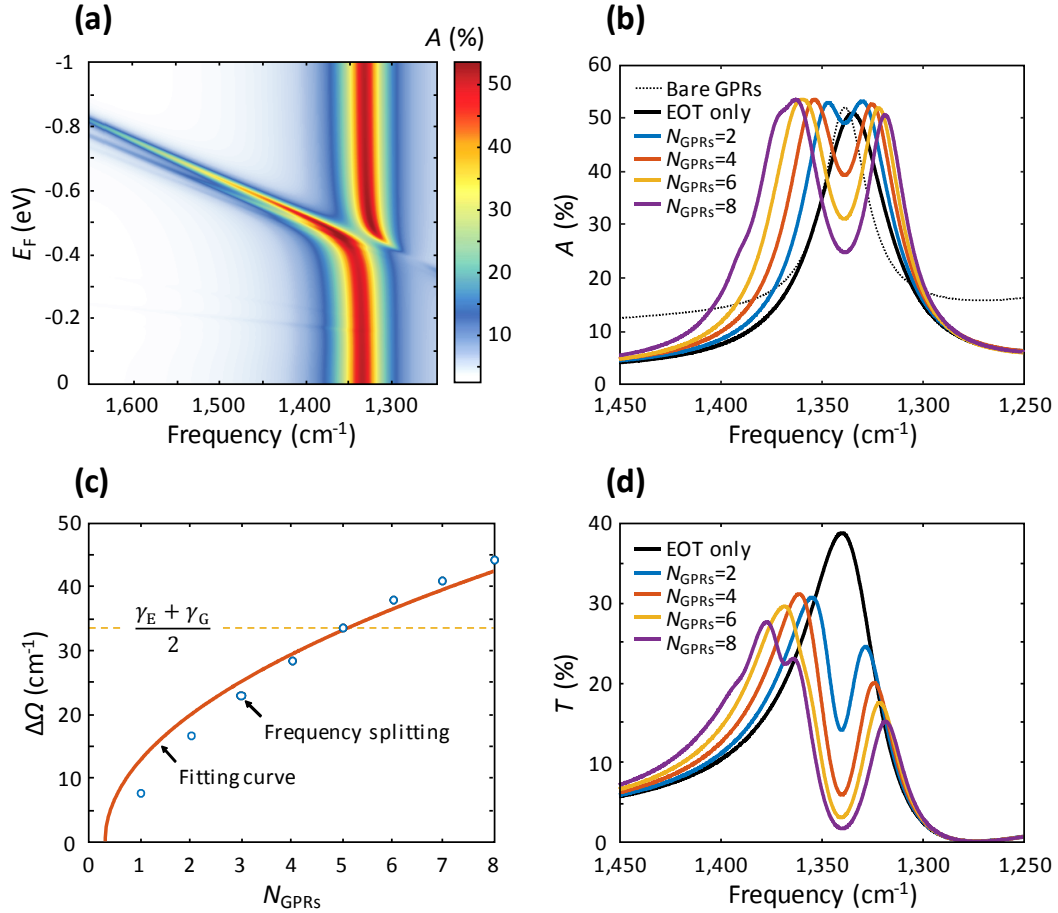


Figure 4.8 | Anti-crossing behavior in the coupled structure. (a) Absorption map of the coupled structure (GPRs-EOT) as a function of frequency and graphene Fermi level (E_F) exhibiting anti-crossing behavior. (b) Absorption spectra, (c) frequency splitting, and (d) transmission spectra as a function of number of graphene plasmonic ribbons (N_{GPRs}) inside the subwavelength metallic slit. In (b) and (d), the ‘‘EOT only’’ indicates the subwavelength metallic slit array without GPRs.

For E_F values far above or far below -0.465 eV, resonant absorption of the GPRs is far away from the transmission resonance of the subwavelength metallic slit array, and the two effects effectively behave independently. As the E_F approached -0.465 eV, however, the plasmonic resonance in GPRs creates large deviations in the local dielectric function near the energy of the EOT mode. Specifically, at energies just below or above the plasmonic resonance in GPRs, the effective permittivity is increased or decreased, respectively. This allows the subwavelength

metallic slit array to support two distinct modes, even though its geometry selects for only one wave vector. That is, a longer wavelength mode exists which experiences a larger permittivity, and a shorter wavelength mode exists which experiences a smaller permittivity. This creates the splitting, or anti-crossing behavior between the graphene plasmonic resonant mode and the EOT resonant mode, as observed in Fig. 4.7(c), and the coupling strength between the EOT structure and the embedded GPRs can be determined from the frequency splitting.

4.5.1 Dependence on Number of Intergap Graphene Plasmonic Ribbons

The frequency splitting is larger than the linewidth of each of the two resonant modes, as shown in Fig. 4.7(c). This indicates that the energy exchange rate between the two resonant modes is faster than the damping rate of each mode, which suggests that the GPRs-EOT device is operating in the strong coupling regime [141]. As a result, the coupled structure shows anti-crossing behavior at a crossing between the graphene plasmonic resonant mode and EOT resonant mode, as shown in Fig. 4.8(a).

The strong coupling nature of this device is further confirmed by modeling the frequency splitting as a function of graphene ribbon density, from which we find a square root relationship [142, 143]. To be specific, the frequency splitting depends on the number of GPRs inside the subwavelength metallic slit (N_{GPRs}), as shown in Fig. 4.8(b). In this calculation, the pitch of the ribbons was determined by 800 nm divided by N_{GPRs} , where the 800 nm corresponds to the subwavelength metallic slit width, and the graphene Fermi level for each N_{GPRs} was tuned to minimize the transmission. To evaluate this relationship, we used the classical oscillator model [143]

$$\Delta\Omega \cong \frac{\alpha}{\lambda_{\text{res}}^{-1}} \sqrt{N_{\text{GPRs}} - \left[\frac{\lambda_{\text{res}}^{-1}(\gamma_{\text{G}} - \gamma_{\text{E}})}{2\alpha} \right]^2} \quad (4.1)$$

where $\Delta\Omega$ is the frequency splitting, α is the coupling coefficient, $\lambda_{\text{res}}^{-1}$ is the resonance frequency, N_{GPRs} is the number of GPRs, and γ_{G} and γ_{E} are the absorption linewidth of bare GPRs and GPRs-EOT, respectively.

In this model, we fitted our data of frequency splitting as a function of number of graphene ribbons N_{GPRs} to extract the coupling coefficient α . The best fit was obtained with $\alpha=2.04 \times 10^4 \text{ cm}^{-2}$, and the root mean square error was 2.39 cm^{-1} , as shown in Fig. 4.8(c). We believe that the small deviation between the model and the calculated frequency splitting comes from assumptions in the classical oscillator model. The model assumes that a single GPR does not interact with adjacent

GPRs, and the coupling coefficient is identical for all GPRs. In a real system, the graphene plasmons are a collective oscillation, which would affect the linewidth γ_G . In addition, the coupling coefficient α would be altered depending on the position of each GPR. Regardless of discrepancies between the assumptions in the model and the real system, this model shows good agreement with the calculated frequency splitting. In addition, the coupled system exhibits a strong coupling when it contains six or more GPRs, as we can see by considering the frequency splitting and the average linewidth of the two resonant modes, as shown in Fig. 4.8(c). As a result of this coupling between two resonant modes, the splitting is also exhibited in transmission spectra, as shown Fig. 4.8(d).

4.5.2 Dependency on Graphene Carrier Mobility

As the graphene carrier mobility is lowered, the Q-factor of the GPRs decreases, and this anti-crossing behavior is lost because the energy exchange rate should be faster than the decay rate of each resonant mode to create strong coupling [141]. Therefore, the anti-crossing behavior disappears if the Q-factor of one resonant mode becomes too low, which happens with a low graphene carrier mobility. As shown in Figs. 4.9(a) and (b), the Q-factor of the GPRs becomes lower as the graphene carrier mobility is decreased. As a result, the anti-crossing behavior in the coupled structure is nearly indiscernible at $\mu_h=1,000 \text{ cm}^2\text{V}^{-1}\text{s}^{-1}$, and completely disappears at $\mu_h=450 \text{ cm}^2\text{V}^{-1}\text{s}^{-1}$, as shown in Figs. 4.9(c) and (d). At a low graphene carrier mobility, there is no dip in the absorption spectra. A clear dip in the absorption spectra begins to emerge at $\mu_h=1,500 \text{ cm}^2\text{V}^{-1}\text{s}^{-1}$, and the frequency splitting is nearly saturated above $\mu_h=5,000 \text{ cm}^2\text{V}^{-1}\text{s}^{-1}$. This tendency is also observed in the transmission spectra, as shown in Figs. 4.9(e) and (f).

In a low graphene carrier mobility regime ($\mu_h \leq 1,000 \text{ cm}^2\text{V}^{-1}\text{s}^{-1}$), the GPRs-EOT modulator still displays relative high efficiencies, but the modulation is achieved by absorption in the GPRs, where the optical modes decay too rapidly to interact strongly with the EOT structure. Notably, the modulation enhancement of the GPRs-EOT device over the bare GPRs device becomes more significant in this damping-dominant regime. Therefore we suggest that coupling between the two resonant modes is the dominant mechanism for light modulation for high carrier mobility graphene (or equivalently a high Q-factor in the graphene plasmonic resonant mode), while the GPRs with low carrier mobility graphene simply damp the EOT mode.

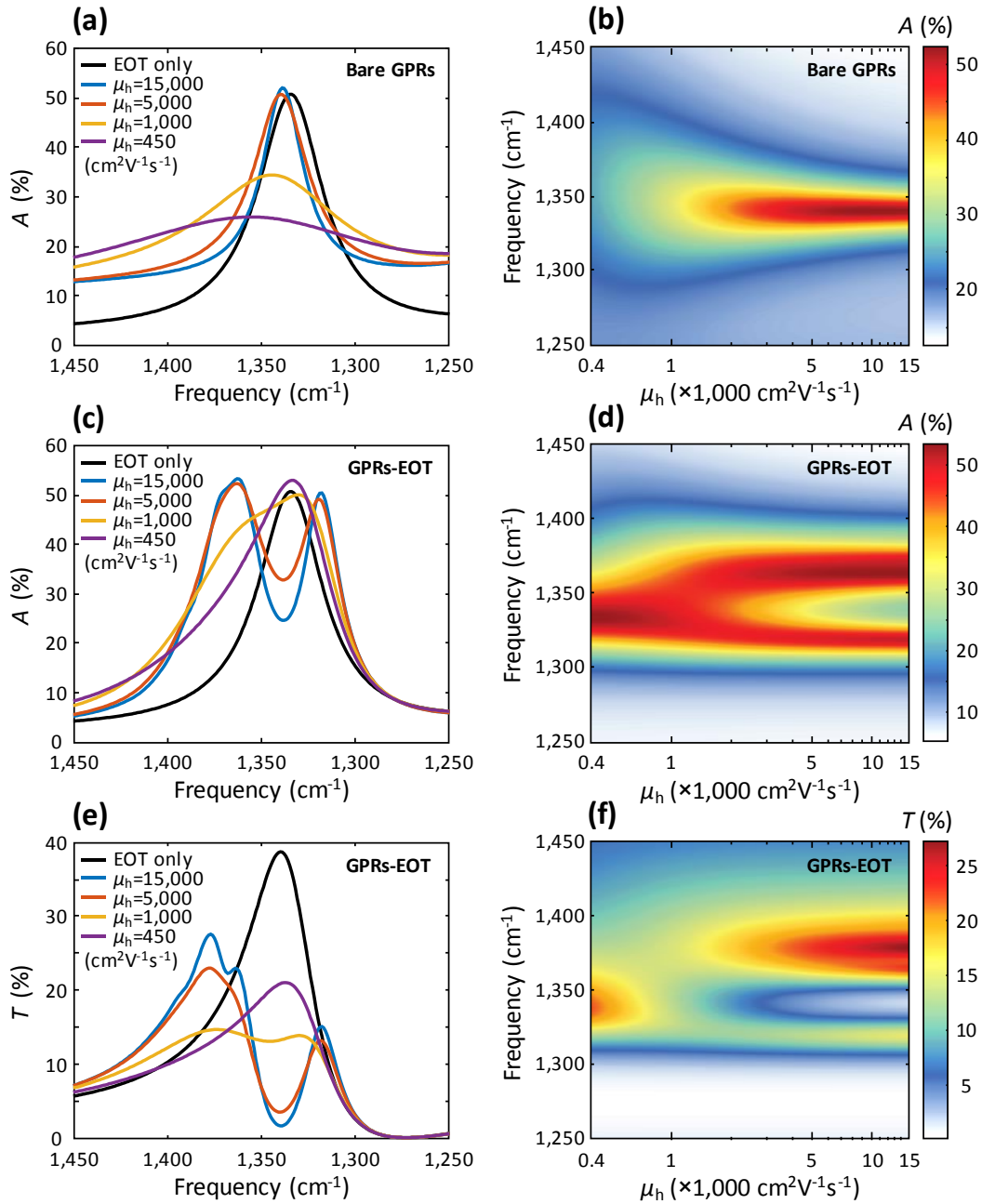


Figure 4.9 | Anti-crossing behavior dependence on graphene carrier mobility. (a) Absorption spectra and (b) absorption map of the bare GPRs device as a function of graphene carrier mobility (μ_h). (c) Absorption spectra and (d) absorption map of the coupled structure (GPRs-EOT) device as a function of graphene carrier mobility (μ_h). (e) Transmission spectra and (f) transmission map of the coupled structure (GPRs-EOT) device as a function of graphene carrier mobility (μ_h). In (a), (c), and (e), the “EOT only” indicates the subwavelength metallic slit array without GPRs.

4.5.3 Absorption-Induced Transparency

In contrast to the decreased transmission seen here due to plasmonic absorption in the GPRs, it has been reported that transmission can increase via absorption, described as absorption-induced transparency [144-146]. In Ref. 146, a nanodisk is used to extract photons from a subwavelength hole and scatter them into free space, so that light transmission is enhanced. This mechanism is possible because the nanodisk's scattering cross-section is comparable to its absorption-cross section. Refs. 147 and 148 report that EOT structures hybridized with dye absorber layers have noted an increase in EOT transmission when the dye is placed inside the subwavelength holes. In those devices, the absorbing medium fills the subwavelength metallic holes, allowing for an altered in-hole propagation constant. While those effects may play some role in the transmission properties of the structure we propose here, we note that in this device the transmission is decreased as the absorbing plasmonic resonances are activated, rather than increased. In the device we demonstrate here, however, the scattering cross-section of GPRs is much smaller than its absorption cross-section due to its extreme spatial confinement [59]. In addition, the GPRs are located only at the bottom the subwavelength metallic slits, making such an effect less likely. While absorption induced transparency might be achievable in devices where the array of tunable GPRs completely fills the subwavelength metallic slits, it is difficult to experimentally realize such a device.

4.6 Experimental Measurements

To demonstrate modulator performance, we fabricated bare GPRs and GPRs-EOT on 2 μm SiN_x membranes. First, a transparent back gate electrode composed of 4 nm of ITO and 60 nm of a-Si was sputtered onto the bottom side of the SiN_x membrane. Since this back electrode is directly connected to the Si frame of the SiN_x membrane, we can apply a gating voltage through the Si frame. After transferring CVD-grown graphene to the top surface, the GPRs were patterned by 100 keV electron beam lithography using a PMMA resist. The graphene plasmonic ribbons were then cut using reactive ion etching with oxygen at 80 W for 15 s, with the patterned PMMA serving as a soft etch mask. Finally, we defined subwavelength metallic slit arrays by electron beam lithography, and the metallic layer was deposited by electron beam evaporation of Ti (3 nm) followed by Au (80 nm). The slit width is 800 nm, and the period of the slit array is 5.6 μm , which puts the EOT peak at $\lambda^{-1}=1,403 \text{ cm}^{-1}$ with undoped graphene in a mid-infrared transmission measurement. Transmission measurements were performed using a Fourier transform

infrared (FTIR) microscope with a polarizer in order to eliminate the transverse electric component from the incoming light.

4.6.1 Characteristics of Graphene

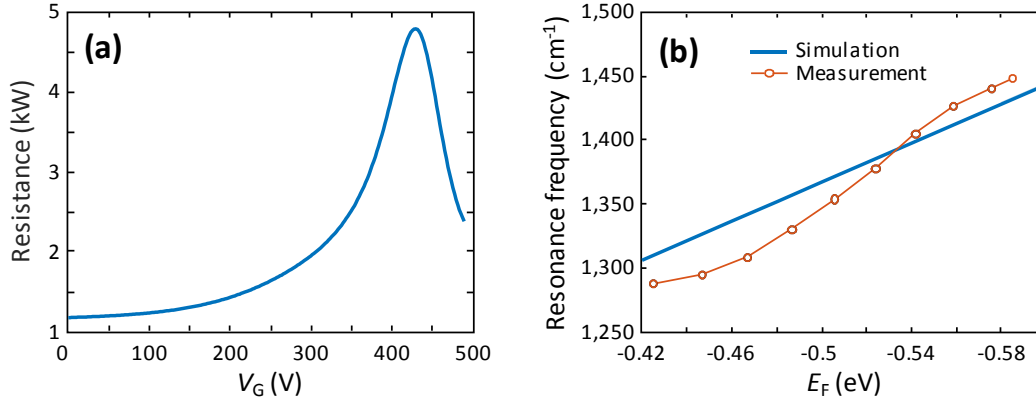


Figure 4.10 | Characteristics of graphene. (a) Gate dependent resistance measurement of graphene on the SiN_x substrate showing the charge neutral point at gating voltage $V_G=430$ V. (b) Graphene plasmon resonance frequency as a function of graphene Fermi level (E_F) for simulations and mid-infrared transmission measurement.

To calculate the graphene Fermi level on SiN_x membrane from the gate voltage (V_G) between the graphene and the back contact, we used the capacitor model in Section 2.2.4 based on the charge neutral point (CNP) measured by a gate dependent resistance measurement of graphene, as shown in Fig. 4.10(a). In the calculation, we assumed the dielectric constant of SiN_x as 10 [60]. As shown in the Fig. 4.10(b), the graphene plasmon resonance frequency depending on graphene Fermi level between simulations and mid-infrared transmission measurement shows good agreement with this dielectric constant. The slight discrepancy between the simulation and the measurement results could come from atmospheric and substrate impurities [147, 148]. Non-uniform DC electric field along the graphene ribbons, such as the lightning rod effect at the edges, could also affect the doping level.

4.6.2 Light Modulation in Transmission

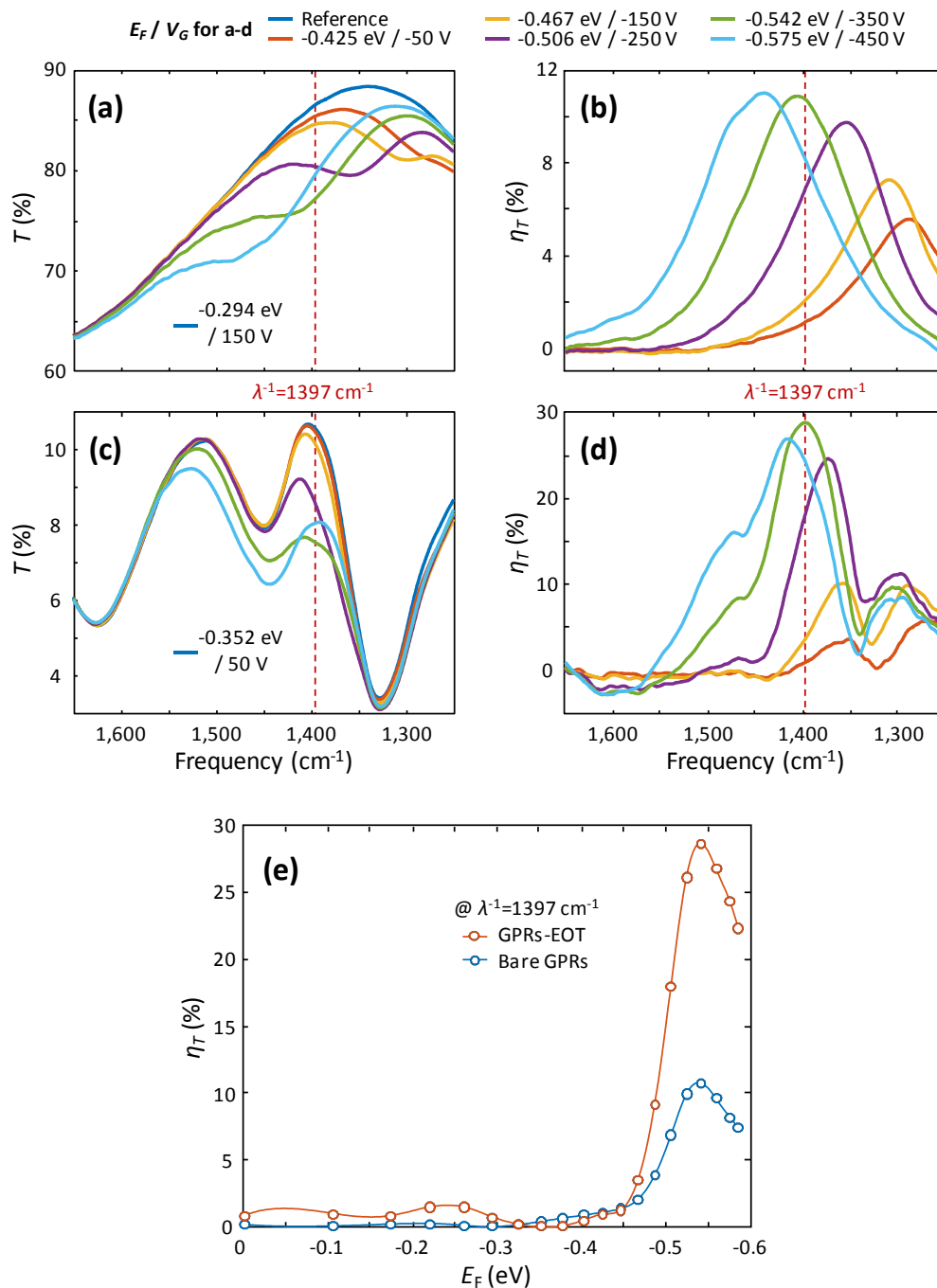


Figure 4.11 | Experimental results. (a) Gate-dependent measured transmission spectra and (b) modulation efficiency (η_T) of the bare GPRs device. (c) Gate-dependent measured transmission spectra and (d) modulation efficiency (η_T) of the coupled structure (GPRs-EOT) device. (e) Gate dependent measured modulation efficiency comparison at $\lambda^{-1} = 1397 \text{ cm}^{-1}$ between bare GPRs device and GPRs-EOT device.

Figure 4.11 compares the experimentally measured transmission spectra and modulation features of bare GPRs and GPRs-EOT devices. As shown in Figs. 4.11(a) and (c), both devices display gate dependent transmission features that become stronger and shift to higher energies with increased graphene doping. To calculate and compare the modulation efficiencies, transmission spectra are normalized by the transmission spectrum with $E_F = -0.294$ eV for bare GPRs device and $E_F = -0.353$ eV for GPRs-EOT device, corresponding to graphene Fermi levels that exhibit maximum transmittance at the EOT resonance frequency. The resulting gate dependent modulation efficiencies in transmission are shown in Figs. 4.11(b) and (d). Both devices exhibit narrowband modulation features that become more intense and blue shift with higher graphene doping. The subwavelength metallic slit array exhibits an EOT peak at $\lambda^{-1} = 1,403$ cm^{-1} where no plasmons exist in the GPRs because of low doping, as shown in Fig. 4.11(c). As doping increases, plasmons are excited in the GPRs inside the subwavelength metallic slits, and block the coupling channel for the EOT resonance. As a result, we observe the transmittance at the EOT peak decline until E_F reaches -0.542 eV, which corresponds to the crossing point between the EOT resonance and the plasmonic resonance in GPRs.

Figure 4.11(e) summarizes the modulation efficiencies of bare GPRs and GPRs-EOT devices. At $\lambda^{-1} = 1,397$ cm^{-1} , the GPRs-EOT device shows maximal modulation efficiency of 28.6% with $E_F = -0.542$ eV, while the bare GPRs device has a maximum modulation efficiency of only 10.7% at the same E_F .

4.6.3 Broad Angular Distribution Effect

The experimental measurements shown in Fig. 4.11 differ from simulations in a number of important ways. Notably, the experimental modulation is lower than the simulated one, and the spectral width of the experimental transmission resonance is significantly broader. These features can be attributed to a number of factors that distinguish measurement from simulations.

The incoming light is illuminated by a Cassegrain-type objective lens with a high numerical aperture (NA) of 0.58, which means the light incidence angle ranges from -35° to 35° . Such a broad angular distribution of incident light results in a broad transmission spectrum and lower transmittance in the EOT structure because the EOT resonance condition strongly depends on incident angle as well as the period of the subwavelength metallic slit array. To estimate the effect from the broad incidence angular distribution, we calculated transmission characteristics by superposing spectra having the incident angle from -35° to 35° with 1° intervals. In these simulations, the period of the subwavelength metallic slit array is 5.2 μm , matching the EOT

resonance frequency ($1,403 \text{ cm}^{-1}$) in our measurements. The resulting calculated transmission spectra are shown in Fig. 4.12(a), and the superposed spectrum (solid green line) shows several differences relative to the transmission spectrum for normally incident light (dotted blue line). Specifically, the superposed spectrum reveals a broader transmission spectrum with an additional peak at higher frequency ($1,618 \text{ cm}^{-1}$). Moreover, the angular spread of incident light lowers the maximum theoretical transmittance of the EOT structure from 42.1% to 9.32%.

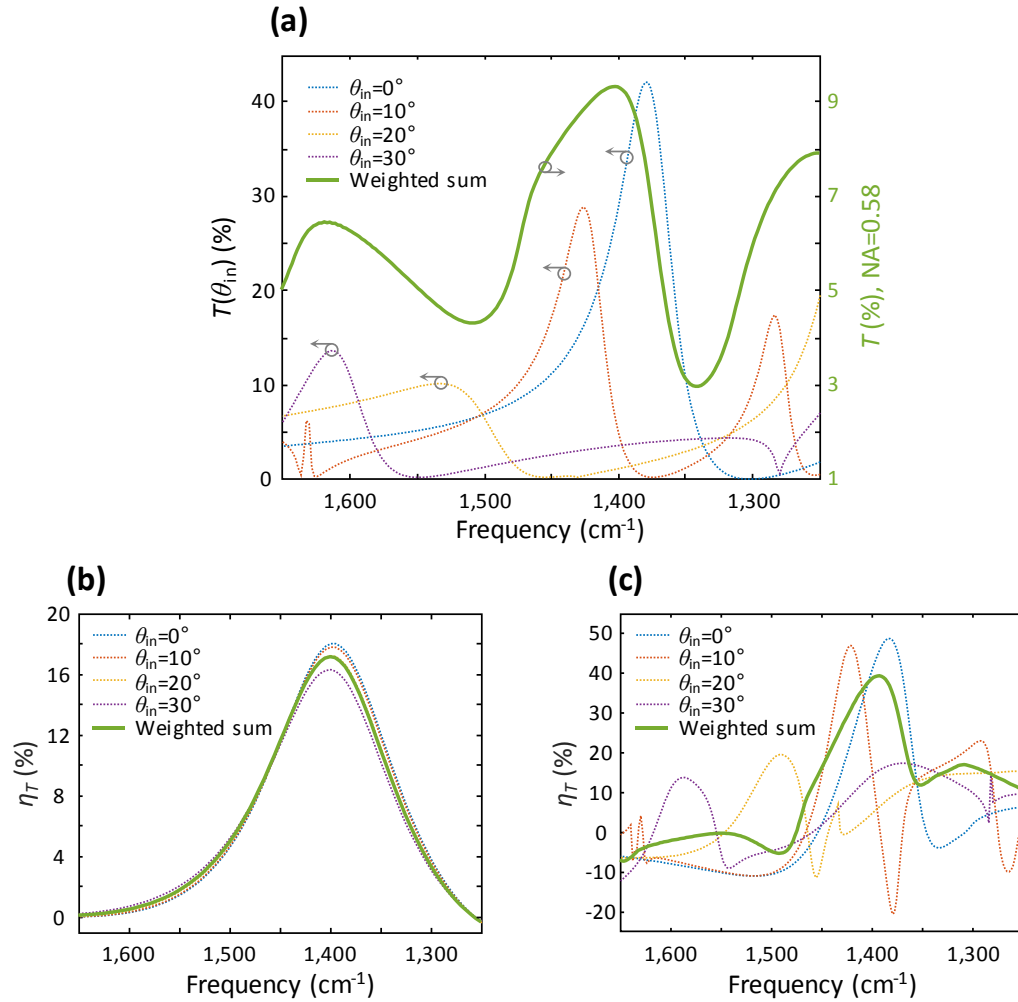


Figure 4.12 | Broad angular distribution effect. (a) Simulation results demonstrating the effect of a broad angular distribution of incoming light. Dotted lines (left axis): transmission spectra of the subwavelength metallic slit array with different incident angles (θ_{in}). Solid line (right axis): weighted sum of transmission spectra at different angles for an objective numerical aperture (NA) of 0.58. (b) Calculated modulation efficiencies for coupled structure (GPRs-EOT) device varying the incident angle (θ_{in}) and the weighed sum. (c) Calculated modulation efficiencies for bare GPRs device varying the incident angle (θ_{in}) and the weighed sum.

The broad angular distribution of incoming light also affects the modulation efficiency in the GPRs-EOT, as shown in Fig. 4.12(b). Similar to the EOT spectrum in Fig. 4.12(a), the modulation peak also blue-shifts with oblique incident light. As a result, the maximum modulation efficiency of the weighted sum spectrum is reduced by 20.3% compared with the modulation spectrum using purely normal incoming light. In the case of bare GPRs, the simulation results show that the NA effect is not so large, as shown in Fig. 4.12(c). Although the modulation efficiency decreases slightly as the incident angle increases, the line shape and the peak position do not change significantly.

4.6.4 Numerical Fitting

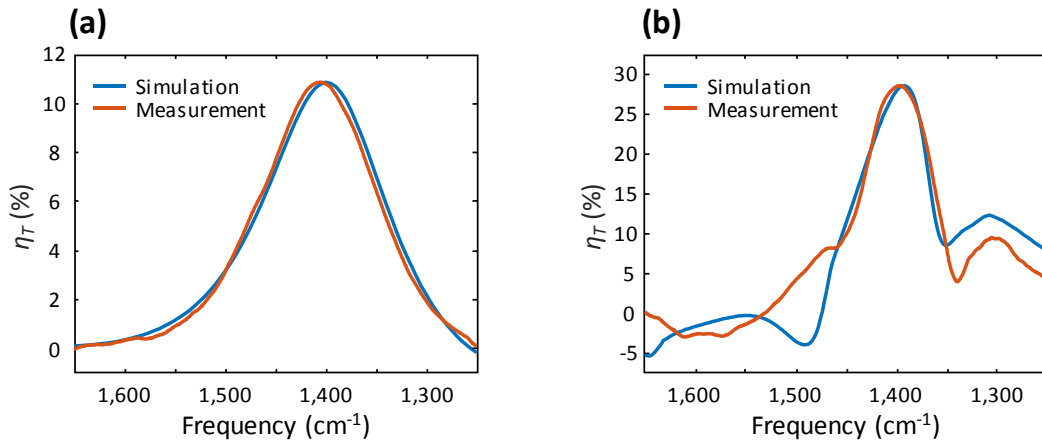


Figure 4.13 | Numerical fitting. (a) Comparison between the measurement result and the simulation result of bare GPRs with a broad angular distribution of incoming light and a scaling factor of 0.633 to account for degradation. (b) Comparison between measurement and simulation result of GPRs-EOT device with a broad angular distribution of incoming light and a scaling factor of 0.734 to account for degradation.

In addition to the broad light incidence angular distribution, some imperfections in fabrication could degrade the modulation efficiency, including, PMMA residue on graphene, carrier density variation in the graphene created by localized charges, a variation in the width of the GPRs resulting from lithography, edge states of the GPRs induced by the etching process, and some resonators that are electronically isolated. These imperfections result in broadening of the graphene plasmon resonance linewidth and a lower modulation efficiency compared with simulations. To account for the broad incident angular distribution and imperfections in fabrication, we tuned

graphene carrier mobility and employed a scaling factor as fitting parameters to explain the linewidth and modulation efficiency.

Figure 4.13(a) shows the simulation and experimental data with $E_F = -0.542$ eV, which corresponds to the graphene Fermi level showing the maximum modulation efficiency in the coupled structure (GPRs-EOT) device. With aforementioned broad angular distribution of incoming light, a graphene carrier mobility of $450 \text{ cm}^2\text{V}^{-1}\text{s}^{-1}$ and a scaling factor of 0.633 to account for degradation, the simulation result matches the measurement result very well. In Fig. 4.13(b), we compared the measurement data with simulation results with a scaling factor of 0.734 to account for degradation. This value is slightly higher compared to the scaling factor for bare GPRs. We expect that there are less dead resonators in the GPRs inside the subwavelength metal slits than in the bare GPRs device because the dimension in transverse direction is much shorter compared with the bare GPRs structure, and therefore could reduce the chance of disconnection. With these fitting parameters, the expected modulation efficiencies with purely normal incident light are 11.4% for bare GPRs device and 36.0% for GPRs-EOT device.

4.7 Conclusions

In summary, GPRs coupled to subwavelength metallic slit array that exhibit EOT enable strong transmission modulation at mid-infrared frequencies. Light absorption in GPRs efficiently suppresses the EOT resonance resulting in high modulation efficiency. Simulations indicate a transmission modulation efficiency of 95.7%. This modulation occurs with small changes in the graphene Fermi level position, within ranges that are accessible with electrostatic gating methods. Experimental mid-infrared transmission measurements of a fabricated device demonstrate that the proposed device exhibits 2.67 times higher than the modulation efficiency of a bare GPRs device. The experimental modulation efficiency could be enhanced by use of graphene with higher carrier mobility and by transmission measurements using a parallel rather than convergent beam illumination configuration since EOT resonances are quite angle-sensitive. The results illustrate the potential for coupling graphene plasmon resonances and conventional noble metal plasmon resonances to achieve transmission-type light modulation, which may be useful in, e.g., actively tunable amplitude modulated infrared metasurfaces and real-time hologram systems.

CHAPTER 5

ELECTRONICALLY TUNABLE GRAPHENE PLASMONIC RESONANCE ENERGY TRANSPORT

We report electronically tunable graphene plasmonic resonance energy transport along graphene plasmonic ribbons, and we devise a platform to demonstrate the energy transport in the mid-infrared. In this structure, two metal-insulator-metal plasmonic waveguides are connected by a subwavelength metal slit, and graphene plasmonic ribbons are located inside this slit. Due to the large impedance mismatch between the noble metal plasmonic waveguide and the subwavelength metal slit, light coupling efficiency across the junction is poor. If the graphene plasmonic ribbons inside the slit are tuned to support strong graphene plasmonic resonances, this generates another pathway for transferring light energy across the junction. As a result, the light transmission across the subwavelength metal slit is enhanced significantly compared to a bare slit without the graphene plasmonic resonance energy transport. In order to electronically modulate the transmission in the noble metal plasmonic waveguide using the graphene plasmonic resonance energy transport, we also have to actively suppress the light energy transfer across the junction. To achieve this, we engineer the junction geometry in order to induce a strong Fano resonance between a non-resonant propagation mode across the junction and a resonant transmission mode via the graphene plasmonic resonance energy transport. Theoretical calculations predict 100% of light modulation efficiency with moderate graphene carrier mobility ($1,660 \text{ cm}^2\text{V}^{-1}\text{s}^{-1}$) at a graphene Fermi level easily accessible with electrostatic gating. The maximum resonant transmission in the plasmonic waveguide across the junction is 43.4%, while the transmission is 14.2% without the graphene plasmon resonance energy transfer mode.

5.1 Introduction

Graphene has been recently proposed as a candidate material to create electronically tunable light modulation devices controlling the phase and the intensity of light at high data rates with little loss. These effects can be created by controlling the graphene interband transitions, as well as by tuning the graphene plasmons supported by the free carriers in graphene plasmonic ribbons (GPRs). The graphene plasmons are particularly interesting for application purposes because the semi-metallic and the two dimensional nature of graphene allows for these modes to be highly tunable from THz to mid-infrared and at a deeply subwavelength scale. Furthermore, while the interband absorption efficiency in graphene is limited to a quantum of optical conductance ($\sim 2.3\%$), the oscillator strength of the graphene plasmonic modes can potentially be much higher, allowing for a higher dynamic range of active control.

These properties have created interests in producing active plasmonic devices based on graphene plasmons that have high modulation depth and can be integrated in chips at length scales approaching those of electronic transistors. Thus far, it has been shown that the oscillator strength in graphene plasmonically-driven optical modulators can be significantly enhanced when they are combined with noble metal plasmonic structures, and electronically tunable absorption up to nearly 70% has been demonstrated in graphene plasmonic metasurface coupled to subwavelength noble metal plasmonic slits. While both reflection and transmission have been successfully modulated by GPRs, those devices have mostly been based on patterning large scale ribbon arrays into a graphene sheet such that it excites collective oscillation in the arrays. Since these devices are based on an array of resonators, they have a large footprint and do not offer an opportunity to study graphene plasmonic resonances in a local area.

In this chapter, we report graphene plasmonic resonance energy transport along GPRs, and it will be shown that the energy transport along the GPRs via localized graphene plasmons is more efficient than the energy transport along a flat graphene sheet via graphene plasmons. In order to demonstrate the electronically tunable and efficient graphene plasmonic resonance energy transport in the mid-infrared, we devise a platform consisting of two metal-insulator-metal (MIM) plasmonic waveguides connected by a subwavelength metal slit, and the GPRs are located inside the slit. If the intergap GPRs are tuned to support strong graphene plasmonic resonances, this generates another pathway for transporting light energy across the junction. As a result, the light transmission across the subwavelength metal slit is enhanced significantly compared to a slit without the graphene plasmonic resonance energy transport.

In addition to the enhanced light transmission efficiency, we also present complete suppression of the transmission across the junction by inducing a strong Fano resonance between a non-resonant propagation mode across the junction and a resonant transmission mode via graphene plasmonic resonance energy transport. Theoretical calculations predict 100% of light modulation efficiency in transmission across the junction with moderate graphene carrier mobility ($1,660 \text{ cm}^2\text{V}^{-1}\text{s}^{-1}$) at a graphene Fermi level easily accessible with electrostatic gating. The maximum resonant transmission in the plasmonic waveguide across the junction is 43.4%, while the transmission is 14.2% without the graphene plasmon resonance energy transfer mode. Notably, the 100% of light modulation efficiency is achievable within a length scale of $\lambda_0/20$, where λ_0 is the free-space wavelength, and the required shift in graphene Fermi level is less than 0.1 eV.

5.2 Graphene Plasmonic Resonance Energy Transport

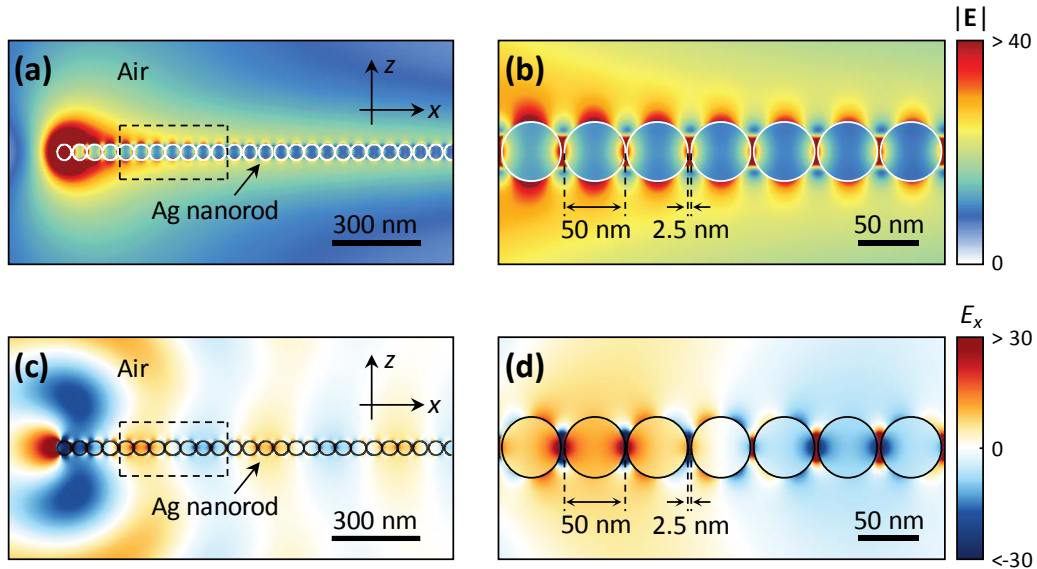


Figure 5.1 | Plasmonic resonance energy transport. Plasmonic resonance energy transport along an Ag nanorod. Electric field distributions (a) in a large field of view and (b) inside the dotted region in a. E_x field distributions (c) in a large field of view and (d) inside the dotted region in c.

It has been reported and demonstrated that light can be guided along a metallic nanoparticle chain [149-153]. In this metal nanoparticle chain, localized surface plasmons are excited in the metallic nanoparticles, and the light energy is transferred via plasmonic coupling between the adjacent nanoparticles. Similar to a conservative plasmonic waveguide system, the light propagates unidirectionally along the nanoparticle chain and exhibits exponential decay as propagating.

Therefore, the interaction between the adjacent localized surface plasmons is the key for the electromagnetic energy transport along the metallic nanoparticle chain.

Figure 5.1 shows the plasmonic resonance energy transport along a metal nanorod chain at the free-space wavelength of 473 nm. The diameter of each nanorod is 50 nm, and the gap between the nanorods is 2.5nm. It is assumed that only the first Ag nanorod is excited in this simulation. Figures 5.1(a) and (b) show a spatially confined non-radiative plasmonic mode propagating along the Ag nanorod chain, and strong coupling between the adjacent localized surface plasmons in the nanorods induces the significantly enhanced near-fields inside the gaps shown in Figs. 5.1(c) and (d).

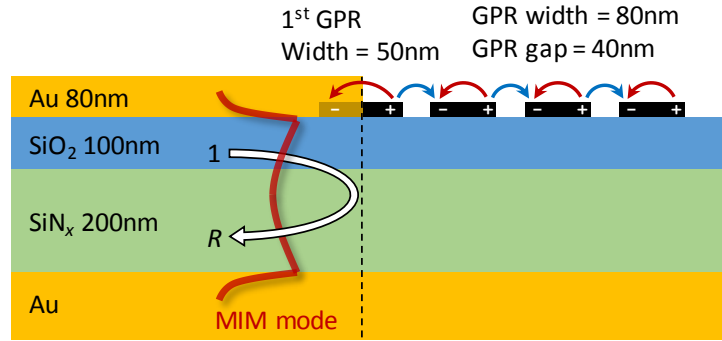


Figure 5.2 | Schematic of launching graphene plasmonic resonance energy transport. The incoming MIM waveguide mode excites localized graphene plasmons in the first GPR denoted by the red arrow, and the graphene plasmonic resonance energy transports along the GPR chain by interacting between the adjacent GPRs denoted by the blue arrows.

Since the graphene plasmons in the GPRs can be considered as localized surface plasmons, we can expect an energy transport along the GPRs via plasmonic coupling between the adjacent GPRs similar to metal nanoparticle chain. Figure 5.2 shows a schematic to evaluate the graphene plasmonic resonance energy transport along GPRs. In this schematic, the insulator layer consists of SiO₂ 100 nm and SiN_x 200 nm, and the left side MIM waveguide is for exciting localized graphene plasmons in the first GPR. The gap width of all GPRs is 40 nm, the first GPR has 50 nm of ribbon width, and other GPRs' ribbon width is 80 nm.

5.2.1 Energy Transfer from MIM Waveguide Mode to Graphene Plasmonic Mode

In Figure 5.3(a), we calculated the electric field intensity at the center of the second GPR ($x=130$ nm) at $1,354\text{cm}^{-1}$ as a function of graphene Fermi level. To appraise the energy transport performance along the GPRs, we also calculated the electric field intensity with a flat graphene sheet at the same position. The graphene carrier mobility in the both calculations was assumed as $1,660\text{cm}^2\text{V}^{-1}\text{s}^{-1}$.

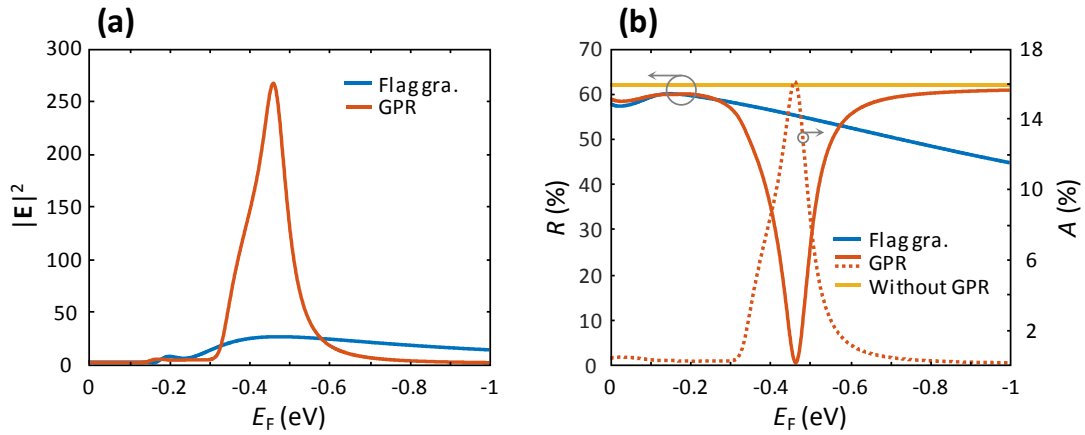


Figure 5.3 | Energy transfer. (a) Electric field intensity in the second GPR and at the same position in the flat graphene sheet as a function of graphene Fermi level (E_F). The intensity is normalized by the average intensity of the incoming MIM waveguide mode at the junction. (b) Reflectance of the MIM waveguide mode at the junction as a function of graphene Fermi level (E_F) with the GPR chain and the flat graphene sheet and without GPRs.

As shown in Figure 5.3(a), the electric field intensity with GPRs exhibits a strong resonance depending on the graphene Fermi level, and the electric field intensity with GPRs is maximized at $E_F = -0.461$ eV. Here, the negative sign of E_F denote that the graphene is hole doped. Although the electric field intensity with a flat graphene sheet also increases at the same graphene Fermi level due to the graphene plasmon mode compared to the lower graphene Fermi level, it does not exhibit a strong resonance dependent upon the graphene Fermi level. Due to the strong graphene plasmonic resonance in the GPRs, Fig. 5.3(a) shows that the energy transport to the second GPRs surpasses that at the same position in a flat graphene at the same graphene Fermi level.

Such a strong graphene plasmonic resonance in GPRs is also displayed in the reflectance of the MIM waveguide mode at the junction, as shown in Fig. 5.3(b). In this structure, the incoming MIM waveguide mode can be coupled to a radiation mode into free-space, a surface plasmon mode

bound to the bottom metal surface, and a graphene plasmon mode at the junction, and an uncoupled remaining amount will be reflected backwards. The strong dip in reflectance with the GPRs at $E_F = -0.464$ eV in Fig. 5.3(b) implies that the energy of the incoming MIM waveguide mode is efficiently transferred to one of the three modes. However, the radiation mode and the surface plasmon mode rarely depend on the graphene Fermi level because their impedances are not strongly affected by the graphene Fermi level, and the reflectance without the GPRs is denoted by a yellow line in Fig. 5.3(b). Therefore, the strong dip in the reflectance with the GPRs indicates the efficient energy transfer from the MIM waveguide mode to the graphene plasmon mode along the GPRs.

The resonant absorption in the GPRs as a function of graphene Fermi level can be considered to estimate the efficient energy transfer from the MIM waveguide mode to the graphene plasmonic mode along the GPRs. As shown in 5.3(b), the maximum absorption in the second GPR occurs at $E_F = -0.461$ eV, and this graphene Fermi level nearly coincides with the dip in the reflectance of the MIM waveguide at $E_F = -0.464$ eV. From this analysis, we can determine that the energy transfer from the MIM waveguide mode to the graphene plasmonic mode along the GPRs is maximized at the maximum graphene plasmonic resonance in the GPRs.

5.2.2 Energy Propagation along Graphene Plasmonic Ribbons

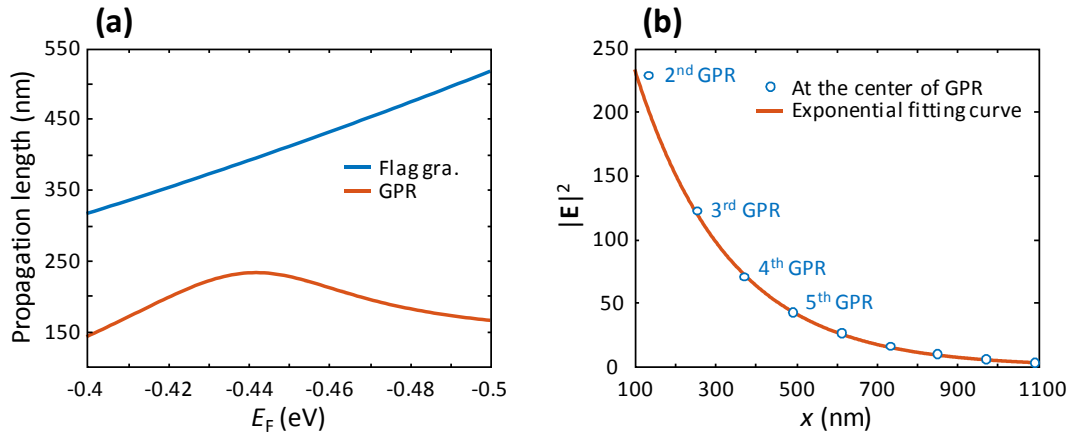


Figure 5.4 | Energy propagation. (a) Propagation length along the GPR chain and the flat graphene sheet as a function of graphene Fermi level (E_F). (b) Exponential fitting to estimate the propagation length at $E_F = -0.442$ eV. To eliminate the effect of the strong radiation field around the junction, the curve is fitted by the intensities at the center of GPRs between the 3rd and the 8th GPRs.

In order to efficiently transport the light energy a certain distance, we also have to consider the decay along the GPRs or the flat graphene sheet as well as the transfer of light energy from the

input MIM waveguide to the graphene plasmonic waveguides. Figure 5.4(a) shows the propagation length along the GPRs and the flat graphene sheet as a function of graphene Fermi level between -0.4 eV and -0.5 eV. The propagation length along the flat graphene sheet was calculated by the graphene plasmon dispersion relation discussed in Chapter 2, and we evaluated the propagation constant along the GPRs by fitting the intensity at the center of GPRs (from the second to the fifth GPRs) with an exponential curve, as shown in Fig. 5.4(b). In the flat graphene sheet, the propagation length monochromatically increase with doping level because the resistive damping in the graphene sheet is reduced with higher graphene carrier density. However, the graphene plasmon mode along the GPRs exhibit a resonance depending on the graphene Fermi level, and the maximum propagation length, or the minimum decay rate, occurs at $E_F = -0.442$ eV. It indicates that the energy transport along the GPRs originates from the interaction between the adjacent GPRs, and the optimum resonance condition exists to enhance the energy transport along the GPRs.

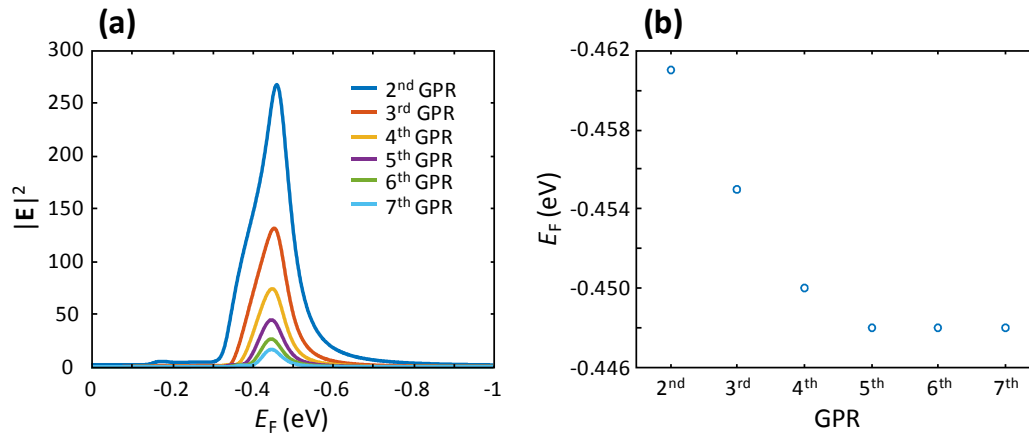


Figure 5.5 | Energy transport. (a) Graphene Fermi level-dependent maximum electric field intensities at the center of each GPR. (b) Graphene Fermi level exhibiting maximum electric field intensities at the center of each GPR.

Regarding propagation length, the flat graphene sheet exhibits lower decay rate than the GPRs, as shown in Fig. 5.4(a). However, the total amount energy transported a certain distance is determined by the energy extracted from the MIM waveguide mode and the decay rate. In Section 5.2.1, it has been shown that more energy can be transferred to the GPRs than the flat graphene sheet from the MIM waveguide mode, and the energy transfer efficiency to the GPRs is large enough to compensate for the low propagation length, which leads to higher light energy transport along the GPRs than the flat graphene sheet.

In the GPRs chain, the optimum graphene Fermi level is also determined by both the energy transfer efficiency and the propagation length. In Fig. 5.3, we can estimate that the energy transfer efficiency to the first GPR is maximized at $E_F = -0.461$ eV, and the decay rate along the GPR chain is minimized at $E_F = -0.442$ eV. As a result of the energy transfer efficiency and the decay rate, the energy transport to each GPR is maximized at different graphene Fermi level, as shown in Fig. 5.5.

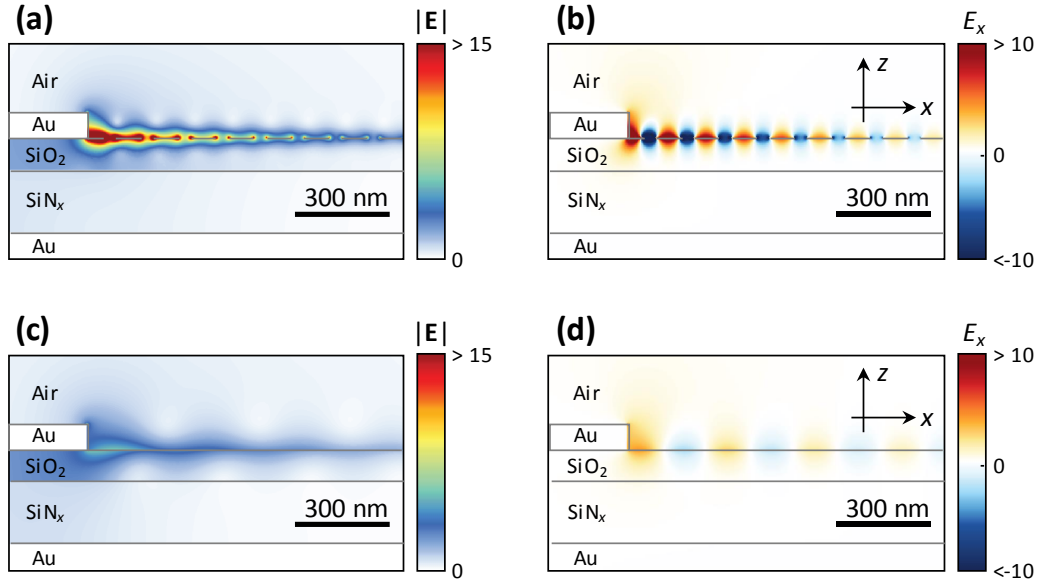


Figure 5.6 | Electric field distribution comparison. (a) Electric field distribution and (b) E_x field distribution with the GPR chain at $E_F = -0.450$ eV. (c) Electric field distribution and (d) E_x field distribution with the flat graphene sheet at $E_F = -0.450$ eV.

Figure 5.6 compares the electric field distributions with the GPRs and the flat graphene sheet at $E_F = -0.450$ eV, where the electric field intensity is maximized at the center of the 4th GPR. In Fig. 5.6, it is shown that the near-field distributions around the GPRs is stronger than that around the flat graphene sheet, which indicates efficient graphene plasmon resonance energy transport along the GPR chain. In addition, Fig. 5.6(b) shows that the magnitude of interaction between the adjacent GPRs (shown in blue), which allows for the energy transport along the GPR chain, is comparable to the localized cavity mode in the GPRs (shown in red).

5.3 Electronically Tunable Light Modulation in MIM Waveguides Connected by a Subwavelength Metal Slit

In Section 5.2, we reported graphene plasmonic resonance energy transport along GPRs, and it has been theoretically analyzed that the energy transport is more efficient along a GPR chain than a flat graphene sheet. Since the graphene plasmonic resonance energy transport depends on the graphene Fermi level, we can modulate the transmitted light in the system if energy transport can be sufficiently suppressed. In this chapter, we present a platform to enhance and suppress the energy transport across two MIM waveguides connected by a subwavelength metal slit to achieve electronically tunable light modulation in the MIM waveguide.

5.3.1 Light Transmission across the Subwavelength Metal Slit

Figure 5.7 shows the schematic of the proposed devices to modulate transmission across MIM waveguides connected by a subwavelength metal slit. The width of the metal slit is 380nm, and four GPRs are located inside the metal slit, equally spaced with a 40 nm gap width. The first and the fourth GPRs have 50nm of ribbon width, and the second and the third GPRs' ribbon width is 80 nm. The top and bottom Au layers' thickness is both 80nm. The insulator consists of SiO₂ and SiN_x, and their thicknesses are 100 nm, and 200 nm, respectively.

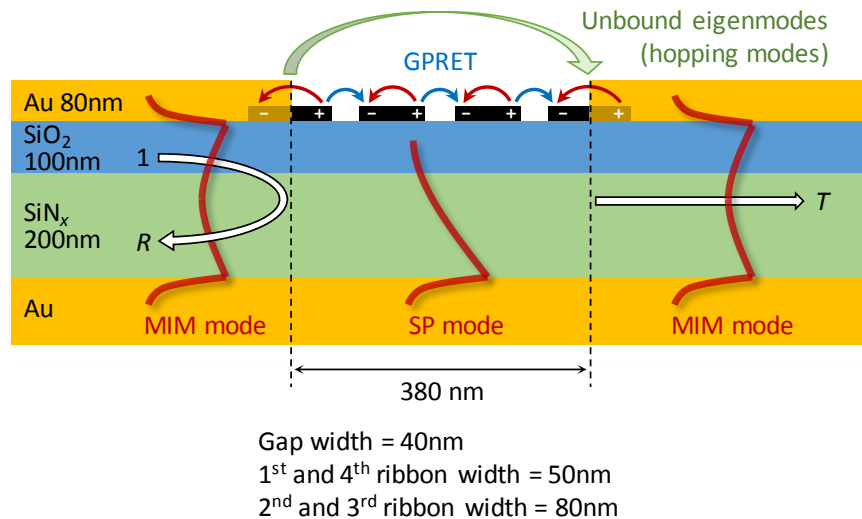


Figure 5.7 | Schematic of device. Incoming light from the left side MIM waveguide can be transmitted across the subwavelength metal slit via three pathways: unbound eigenmodes, a surface plasmon (SP) mode bound to the bottom metal surface, and graphene plasmonic resonance energy transport (GPRET).

There are three light transmission pathways from the left MIM waveguide to the right MIM waveguide across the subwavelength metal slit, as shown in Fig. 5.7. First, light can be transmitted via a surface plasmon mode bound to the bottom metal surface. Second, incoming light in the left MIM waveguide will be scattered at the junction, and the scattered unbound eigenmodes, or hopping modes, can be directly coupled to the right MIM waveguide. Third, the incoming MIM waveguide mode launches the graphene plasmons in the first GPR, and the graphene plasmons can be propagate along the GPRs via interaction between the adjacent GPRs, corresponding to the graphene plasmon resonance energy transport.

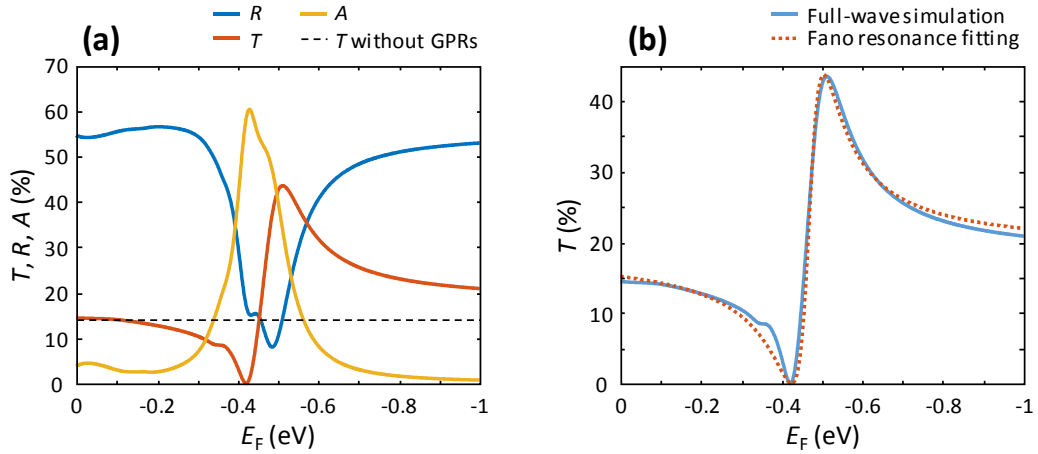


Figure 5.8 | Light modulation by intergap graphene plasmonic ribbons. (a) Transmittance, reflectance, and absorption across the subwavelength metal slit with the intergap GPRs as a function of graphene Fermi level (E_F). The black dotted line corresponds to transmittance without the intergap GPRs. (b) Transmittance comparison between full-wave simulation and the Fano resonance model in Eq. (5.1).

Figure 5.8(a) shows the transmittance and the reflectance across the subwavelength metal slit, and the absorption in the GPRs as a function of graphene Fermi level. In this simulation, the frequency and the graphene carrier mobility are assumed to be $1,354 \text{ cm}^{-1}$ and $1,660 \text{ cm}^2\text{V}^{-1}\text{s}^{-1}$, respectively. The black dotted line corresponds to the transmittance without the GPRs. At around the maximum absorption in the GPRs ($E_F = -0.429 \text{ eV}$), the transmittance changes abruptly, and a maximum and a minimum occurs at $E_F = -0.512 \text{ eV}$ and $E_F = -0.421 \text{ eV}$, respectively. Notably, the maximum transmittance (43.4%) is three times larger than the transmittance without the GPRs (14.2%), and the reflectance becomes zero at the minimum. Moreover, a 100% modulation efficiency is achievable in a deeply subwavelength length scale active region. Considering the free-

space wavelength λ_0 is $7.39\mu\text{m}$, the required length of the active region, or the subwavelength metal slit, is only $\lambda_0/20$. In addition, the required change in the graphene Fermi level for 100% modulation efficiency is less than 0.1 eV, as shown in Fig. 5.8.

The electric field distribution and the time-averaged power flow along x -axis at the graphene Fermi level exhibiting the minimum and the maximum transmittance are shown in Fig. 5.9. The near-fields around the GPRs at both graphene Fermi levels are strongly enhanced due to graphene plasmons in the GPRs. However, it is shown that light cannot propagate across the subwavelength metal slit at $E_F=-0.421$ eV due to destructive interference with the non-resonant mode and the resonant mode, while smooth propagation is observed at $E_F=-0.512$ eV.

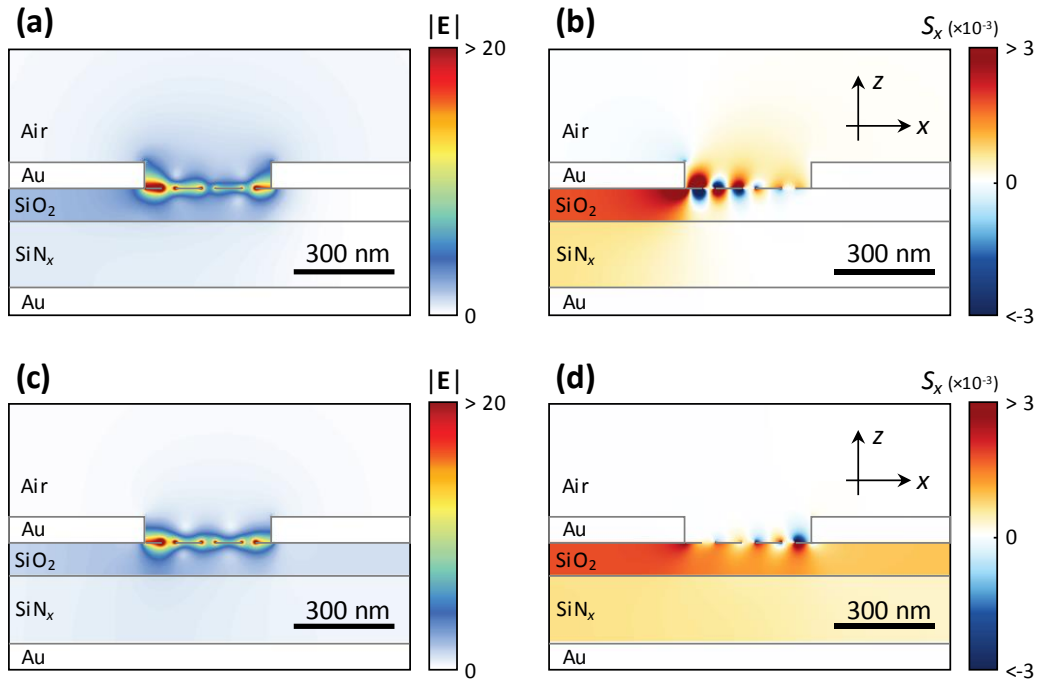


Figure 5.9 | Electric field and power flow distributions. (a) Electric field distribution and (b) S_x distribution exhibiting the minimum transmittance at $E_F=-0.421$ eV. (c) Electric field distribution and (d) S_x distribution exhibiting the maximum transmittance at $E_F=-0.512$ eV.

In contrast to the reflection and the absorption lineshapes exhibiting symmetric resonances depending on graphene Fermi level, the transmission displays an asymmetric resonance. Considering that the unbound eigenmodes and the surface plasmon mode across the subwavelength metal slit are not strongly dependent on the graphene Fermi level, we could expect that they will show a broad lineshape as a function of graphene Fermi level, so that these two modes correspond to a broad non-resonant propagation mode across the subwavelength metal slit. Compared to these

two modes, the strong resonant shape in absorption indicates that the graphene plasmon mode propagating along the GPRs is strongly determined by the graphene Fermi level, corresponding to a narrow resonant propagation mode across the subwavelength metal slit. Since the non-resonant and the resonant propagation modes coexist inside the subwavelength metal slit, we can expect the overall transmission across the subwavelength metal slit will exhibit a Fano resonance lineshape.

5.3.2 Fano Resonance within the Subwavelength Metal Slit

To induce Fano resonance, we need two interfering modes: a broad non-resonant mode, or continuum, and a sharp resonant mode, or discrete state [154, 155]. As these two modes interfere destructively or constructively depending on their phase difference, the interference results in the asymmetric lineshape. Within the subwavelength metal slit, there are two pathways for light transmission: a non-resonant propagation (unbound eigenmodes and a surface plasmon mode) and a resonant propagation via the graphene plasmonic resonance energy transfer. Therefore, the asymmetric lineshape in the transmittance arise from the Fano resonance between the two propagation modes.

The Fano resonance in the transmittance can be modeled by [154, 155]

$$T = C_T \frac{[(E_F - E_{F,0}) + (\Delta E_F/2)q]^2}{(E_F - E_{F,0})^2 + (\Delta E_F/2)^2} \quad (5.1)$$

where C_T is the coefficient to fit the maximum transmittance, E_F is the graphene Fermi level, $E_{F,0}$ is the graphene Fermi level at a resonance, ΔE_F is the linewidth in graphene Fermi level, and q is the asymmetric parameter describing the energy balance between the non-resonant mode and the resonant mode. When q is on the order of unity, the amount of non-resonant and resonant modes are comparable, which leads to a well-balanced interference exhibiting the asymmetric Fano lineshape [154-157]. Figure 5.8(b) shows the Fano resonance fitting curve with $C_T=0.187$, $E_{F,0}=0.470$ eV, $\Delta E_F=0.079$ eV, and $q=1.156$. Here, q of nearly one confirms that both the non-resonant mode and the resonant mode contribute to the transmission across the subwavelength metal slit, and the asymmetric lineshape in the transmittance originates from the Fano resonance between the two modes.

To account for the interference caused by the phase difference between the two modes, we decomposed the non-resonant mode and the resonant mode in Fig. 5.10. In this calculation, we assumed that the non-resonant mode consisting of the unbound eigenmodes and the surface plasmon mode are independent of the graphene Fermi level such that the transmission coefficient

of the non-resonant mode ($t_{\text{non-res}}$) is equal to the transmission coefficient across the subwavelength metal slit without the GPRs. Then, the transmission coefficient of the resonant mode (t_{res}) via the graphene plasmonic resonance energy transport is calculated by $t_{\text{total}} - t_{\text{non-res}}$, where t_{total} is the total transmission coefficient across the subwavelength metal slit as a function of graphene Fermi level.

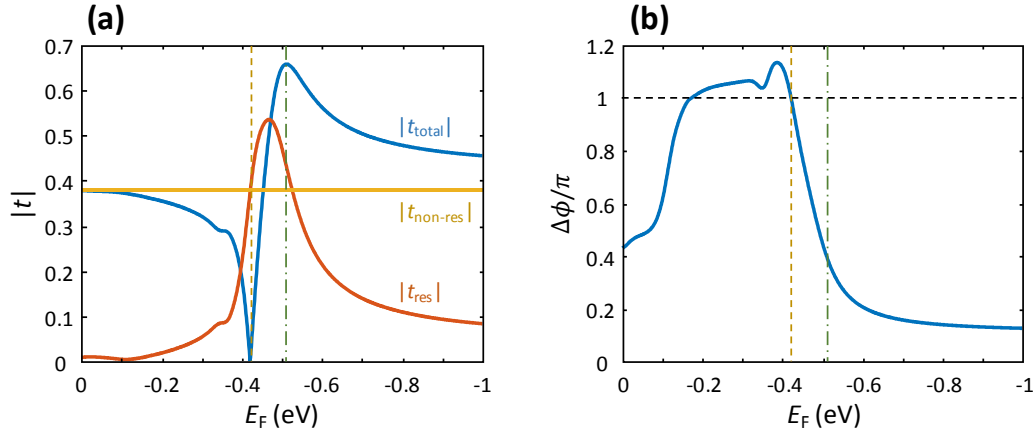


Figure 5.10 | Transmission coefficients. (a) Transmission coefficients as a function of graphene Fermi level (E_F). (b) Phase difference between the non-resonant mode and the resonant mode as a function of graphene Fermi level. The yellow dotted line and the green dashed line are located at $E_F = -0.421$ eV and $E_F = -0.512$ eV where the transmission is minimum and maximum, respectively.

Assuming that the $t_{\text{non-res}}$ is a constant independent of graphene Fermi level and the magnitude of t_{res} displays a Lorentzian-like resonant shape, the interference of the two modes results in the asymmetric lineshape in t_{total} , as shown in Fig. 5.10(a). The graphene Fermi level exhibiting the maximum $|t_{\text{res}}$ is -0.468 eV, and the full-width half-maximum of $|t_{\text{res}}|^2$ is calculated by 0.105 eV. These values show good agreement with the Fano resonance fitting in Fig. 5.8(b), and this result confirms the validation of the assumption.

At $E_F = -0.421$ eV where the t_{total} becomes minimum, the magnitudes of the $t_{\text{non-res}}$ and the t_{res} are identical, and the phase difference ($\Delta\phi$) is equal to π , as shown in Fig. 5.10(b). This relationship indicates the total destructive interference, and it leads to complete suppression of the transmission across the subwavelength metal slit. After $E_F = -0.421$ eV, the phase difference is abruptly deviates from π toward zero. This phase relationship allows for constructive interference, resulting in the maximum transmission at $E_F = -0.512$ eV.

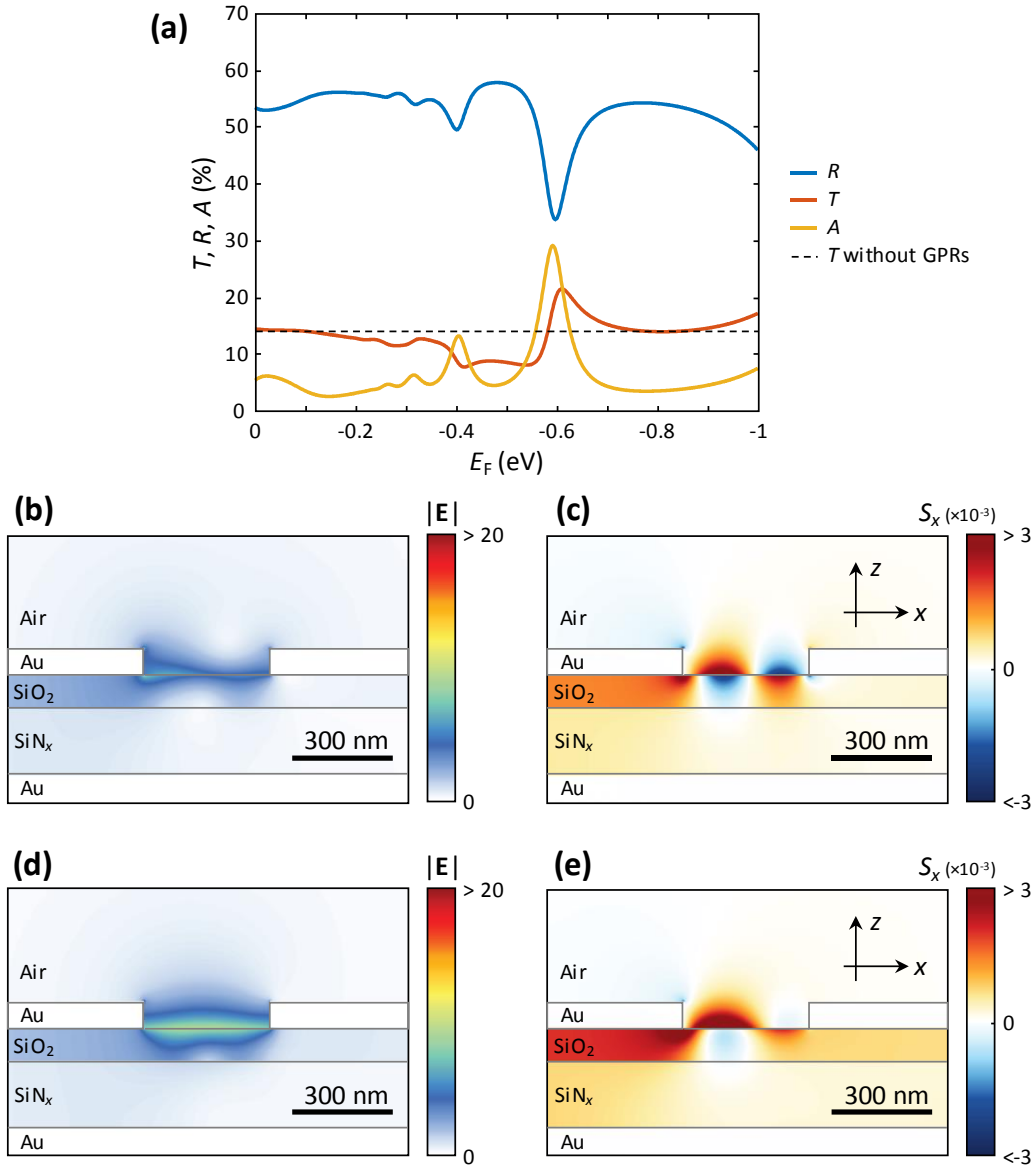


Figure 5.11 | Light modulation by an intergap graphene sheet. (a) Transmittance, reflectance, and absorption across the subwavelength metal slit with an intergap graphene sheet as a function of graphene Fermi level (E_F). The black dotted line corresponds to transmittance without the intergap GPRs. (b) Electric field distribution and (c) S_x distribution at $E_F = -0.539$ eV exhibiting the minimum transmittance. (d) Electric field distribution and (e) S_x distribution at $E_F = -0.610$ eV exhibiting the maximum transmittance.

Similar light modulation effects across the subwavelength metal slit are also observed with a flat graphene sheet, as shown in Fig. 5.11. However, the light modulation strength is not comparable to that with the intergap GPRs because the graphene plasmonic resonance energy transport is more efficient along the GPRs than the flat graphene sheet. In Fig. 5.11(a), the

fluctuation in the transmittance arises from the interference between the non-resonant propagation mode and the higher-order graphene plasmon mode in the flat graphene sheet.

5.3.3 Light Modulation Efficiency Dependent on Graphene Carrier Mobility

The oscillator strength of graphene plasmons in the GPRs is strongly dependent on the graphene carrier mobility because the graphene carrier mobility determines the resistive damping rate of the oscillation. To be specific, higher graphene carrier mobility results in higher Q-factor in the resonance and a more optically conductive graphene plasmonic metasurface, as discussed in Chapters 3 and 4. Such a dependency on the graphene carrier mobility is also observed in the graphene plasmonic resonance energy transport.

Figure 5.12(a) shows the transmittance characteristics depending on the graphene carrier mobility. The maximum transmittance (T_{\max}) monochromatically increases with graphene carrier mobility because the higher graphene carrier mobility reduces the decay rate along the GPRs, which results in more efficient graphene plasmonic resonance energy transport along the GPR chain. However, the modulation efficiency ($\eta_T=1-T_{\min}/T_{\max}$) is maximized at $\mu_h=1,660 \text{ cm}^2\text{V}^{-1}\text{s}^{-1}$, then decreases with higher graphene carrier mobility because of the minimum transmittance (T_{\min}) dependent on the graphene carrier mobility. Figure 5.12(b) shows the transmittance as a function of graphene Fermi level with different graphene carrier mobilities.

This tendency can be understood when we examine the transmission coefficients shown in Figs. 5.12(c) and (d). To achieve 100% of modulation efficiency, we need to totally suppress the transmission, and the total suppression in the transmission requires completely destructive interference between the non-resonant mode and the resonant mode. It indicates that the transmission strength of two mode should be equal when their phase difference is π . This condition is satisfied with $\mu_h=1,660 \text{ cm}^2\text{V}^{-1}\text{s}^{-1}$, as shown in Fig. 5.10. If $\mu_h=1,000 \text{ cm}^2\text{V}^{-1}\text{s}^{-1}$, the transmission strength of the resonant mode is smaller than that of the non-resonant mode when their phase difference is π at $E_F=-0.403 \text{ eV}$. If the graphene carrier mobility becomes even lower ($\mu_h=500 \text{ cm}^2\text{V}^{-1}\text{s}^{-1}$), the phase difference cannot reach π because of the weak oscillator strength in the GPRs. On the other hand, the transmission strength of the resonant mode with $\mu_h=4,000 \text{ cm}^2\text{V}^{-1}\text{s}^{-1}$ at $\Delta\phi=\pi$ ($E_F=-0.428 \text{ eV}$) is larger than that of the non-resonant mode. As a result, those two modes cannot achieve complete destructive interference, and the minimum transmittance becomes a non-zero value.

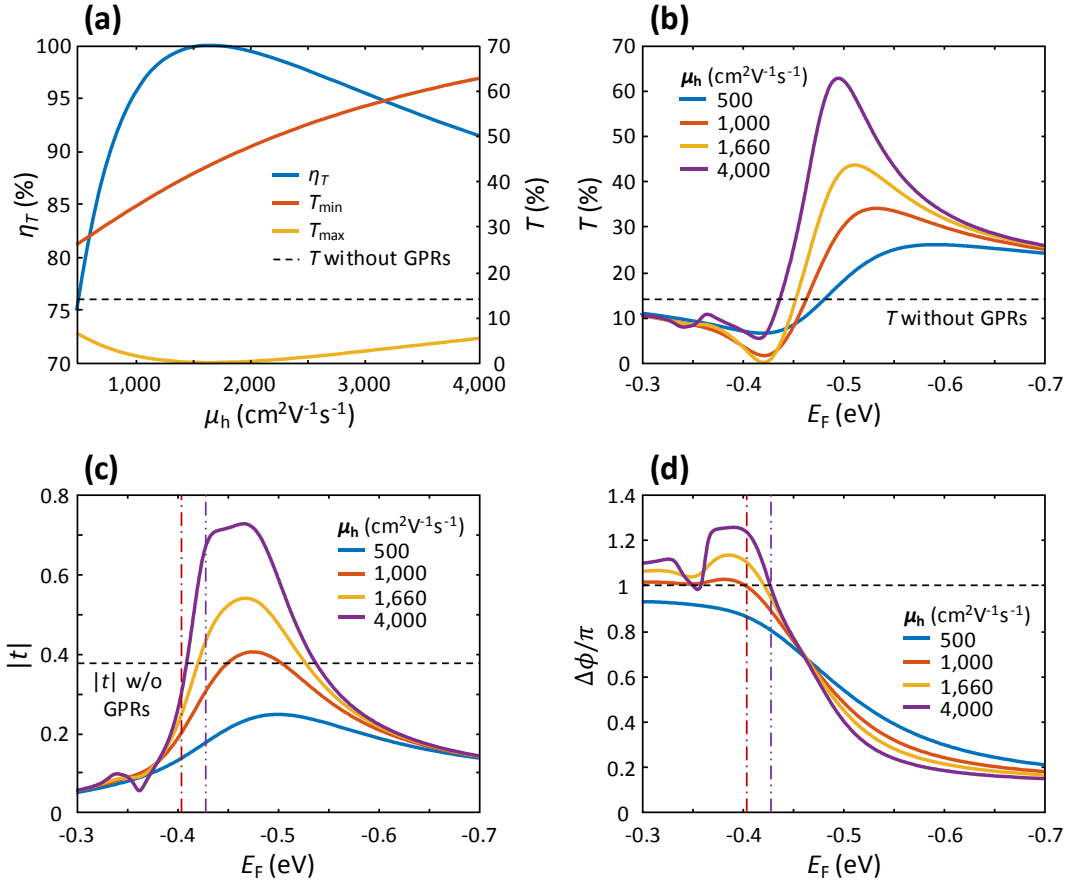


Figure 5.12 | Dependency on graphene carrier mobility. (a) Transmittance and modulation efficiency as a function of graphene carrier mobility (μ_h). (b) Transmittance with different graphene carrier mobilities as a function of graphene Fermi level (E_F). (c) Transmission coefficients and (d) phase difference between the non-resonant mode and the resonant mode as a function of graphene Fermi level with different graphene carrier mobilities. In c and d, the red dashed line and the purple double dashed line are located at $E_F = -0.403$ eV and $E_F = -0.428$ eV, respectively.

5.4 Conclusions

In summary, we report electronically tunable graphene plasmonic resonance energy transport along GPR chain. Because of the efficient energy transfer from incoming light to the GPR, it is shown that the energy transport efficiency is higher along the GPR chain than a flat graphene sheet. Using this energy transport effect, we devise an active light modulator integrated in a plasmonic waveguide with a 100% light modulation efficiency achieved by a Fano resonance induced by a non-resonant propagation mode and a resonant propagation mode via the graphene plasmonic resonance energy transport. In this device, the transmittance is enhanced by a factor of

3 compared to a device without GPRs, and the required length scale of the active region for 100% of light modulation efficiency is no more than $1/20$ of free-space wavelength. In addition, less than 0.1 eV shift in graphene Fermi level is necessary to tune the transmittance from the minimum and the maximum. We believe that this device can be utilized to realize integrated ultrafast and high efficiency plasmonic circuits.

BIBLIOGRAPHY

1. M. Gu *et al.* Optical storage arrays: A perspective for future big data storage. *Light Sci. Appl.* **3**, e177 (2014).
2. B. Parida *et al.* A review of solar photovoltaic technologies. *Renewable Sustainable Energy Rev.* **15**, 1625-1636 (2011).
3. B. Lee. Review of the present status of optical fiber sensors. *Opt. Fiber Technol.* **9**, 57-79 (2003).
4. D. Wencel *et al.* Optical chemical pH sensors. *Anal. Chem.* **86**, 15-29 (2014).
5. Y. H. Su *et al.* Photochemical transformations accelerated in continuous-flow reactors: Basic concepts and applications. *Chem. Eur. J.* **20**, 10562-10589 (2014).
6. X. Zhang *et al.* Superlenses to overcome the diffraction limit. *Nat. Mater.* **7**, 435-441 (2008).
7. H. A. Atwater *et al.* Plasmonics for improved photovoltaic devices. *Nat. Mater.* **9**, 205-213 (2010).
8. E. S. Thrall *et al.* The role of photon energy and semiconductor substrate in the plasmon-mediated photooxidation of citrate by silver nanoparticles. *J. Phys. Chem. C* **117**, 26238-26247 (2013).
9. W. L. Barnes *et al.* Surface plasmon subwavelength optics. *Nature* **424**, 824-830 (2003).
10. J. Takahara *et al.* Guiding of a one-dimensional optical beam with nanometer diameter. *Opt. Lett.* **22**, 475-477 (1997).
11. Y. R. Fang *et al.* Nanoplasmonic waveguides: Towards applications in integrated nanophotonic circuits. *Light Sci. Appl.* **4**, e294 (2015).
12. N. F. Yu *et al.* Flat optics with designer metasurfaces. *Nat. Mater.* **13**, 139-150 (2014).
13. S. Schlucker. Surface-enhanced Raman spectroscopy: Concepts and chemical applications. *Angew. Chem. Int. Ed.* **53**, 4756-4795 (2014).
14. S. Kim *et al.* Off-axis directional beaming of optical field diffracted by a single subwavelength metal slit with asymmetric dielectric surface gratings. *Appl. Phys. Lett.* **90**, 051113 (2007).
15. S. Kim *et al.* Optical beam focusing by a single subwavelength metal slit surrounded by chirped dielectric surface gratings. *Appl. Phys. Lett.* **92**, 013103 (2008).
16. H. Raether. Surface-plasmons on smooth and rough surfaces and on gratings. *Springer-Verlag* **111**, 1-133 (1988).
17. E. D. Palik *et al.* *Handbook of optical constants of solids* (Academic Press, 1998).

18. B. E. A. Saleh *et al.* *Fundamentals of photonics* (Wiley Interscience, 2007).
19. B. Lee *et al.* The use of plasmonics in light beaming and focusing. *Prog. Quantum Electron.* **34**, 47-87 (2010).
20. J. B. Pendry *et al.* Extremely low frequency plasmons in metallic mesostructures. *Phys. Rev. Lett.* **76**, 4773-4776 (1996).
21. M. E. Stewart *et al.* Nanostructured plasmonic sensors. *Chem. Rev.* **108**, 494-521 (2008).
22. W. Rechberger *et al.* Optical properties of two interacting gold nanoparticles. *Opt. Commun.* **220**, 137-141 (2003).
23. T. W. Ebbesen *et al.* Extraordinary optical transmission through sub-wavelength hole arrays. *Nature* **391**, 667-669 (1998).
24. J. A. Porto *et al.* Transmission resonances on metallic gratings with very narrow slits. *Phys. Rev. Lett.* **83**, 2845-2848 (1999).
25. L. Martin-Moreno *et al.* Theory of extraordinary optical transmission through subwavelength hole arrays. *Phys. Rev. Lett.* **86**, 1114-1117 (2001).
26. D. Pacifici *et al.* Quantitative determination of optical transmission through subwavelength slit arrays in Ag films: Role of surface wave interference and local coupling between adjacent slits. *Phys. Rev. B* **77**, 115411 (2008).
27. D. Pacifici *et al.* Universal optical transmission features in periodic and quasiperiodic hole arrays. *Opt. Express* **16**, 9222-9238 (2008).
28. J. A. Dionne *et al.* Plasmon slot waveguides: Towards chip-scale propagation with subwavelength-scale localization. *Phys. Rev. B* **73**, 035407 (2006).
29. W. S. Cai *et al.* Compact, high-speed and power-efficient electrooptic plasmonic modulators. *Nano Lett.* **9**, 4403-4411 (2009).
30. A. Melikyan *et al.* High-speed plasmonic phase modulators. *Nat. Photonics* **8**, 229-233 (2014).
31. I. M. Pryce *et al.* Highly strained compliant optical metamaterials with large frequency tunability. *Nano Lett.* **10**, 4222-4227 (2010).
32. I. M. Pryce *et al.* Compliant metamaterials for resonantly enhanced infrared absorption spectroscopy and refractive index sensing. *ACS Nano* **5**, 8167-8174 (2011).
33. M. J. Dicken *et al.* Frequency tunable near-infrared metamaterials based on VO₂ phase transition. *Opt. Express* **17**, 18330-18339 (2009).
34. L. A. Sweatlock *et al.* Vanadium dioxide based plasmonic modulators. *Opt. Express* **20**, 8700-8709 (2012).
35. K. S. Novoselov *et al.* Two-dimensional gas of massless Dirac fermions in graphene. *Nature* **438**, 197-200 (2005).

36. M. S. Fuhrer *et al.* Graphene: Materially better carbon. *MRS Bull.* **35**, 289-295 (2010).
37. A. H. Castro Neto *et al.* The electronic properties of graphene. *Rev. Mod. Phys.* **81**, 109-162 (2009).
38. C. Lee *et al.* Measurement of the elastic properties and intrinsic strength of monolayer graphene. *Science* **321**, 385-388 (2008).
39. A. A. Balandin *et al.* Superior thermal conductivity of single-layer graphene. *Nano Lett.* **8**, 902-907 (2008).
40. R. R. Nair *et al.* Fine structure constant defines visual transparency of graphene. *Science* **320**, 1308-1308 (2008).
41. Z. Fei *et al.* Gate-tuning of graphene plasmons revealed by infrared nano-imaging. *Nature* **487**, 82-85 (2012).
42. J. N. Chen *et al.* Optical nano-imaging of gate-tunable graphene plasmons. *Nature* **487**, 77-81 (2012).
43. P. Alonso-Gonzalez *et al.* Controlling graphene plasmons with resonant metal antennas and spatial conductivity patterns. *Science* **344**, 1369-1373 (2014).
44. F. H. L. Koppens *et al.* Graphene plasmonics: A platform for strong light-matter interactions. *Nano Lett.* **11**, 3370-3377 (2011).
45. M. Jablan *et al.* Plasmonics in graphene at infrared frequencies. *Phys. Rev. B* **80**, 245435 (2009).
46. A. N. Grigorenko *et al.* Graphene plasmonics. *Nat. Photonics* **6**, 749-758 (2012).
47. F. J. García de Abajo. Multiple excitation of confined graphene plasmons by single free electrons. *ACS Nano* **7**, 11409-11419 (2013).
48. T. Low *et al.* Graphene plasmonics for terahertz to mid-infrared applications. *ACS Nano* **8**, 1086-1101 (2014).
49. F. J. García de Abajo. Graphene plasmonics: Challenges and opportunities. *ACS Photonics* **1**, 135-152 (2014).
50. T. J. Constant *et al.* All-optical generation of surface plasmons in graphene. *Nat. Phys.* **12**, 124-127 (2016).
51. H. G. Yan *et al.* Damping pathways of mid-infrared plasmons in graphene nanostructures. *Nat. Photonics* **7**, 394-399 (2013).
52. G. X. Ni *et al.* Ultrafast optical switching of infrared plasmon polaritons in high-mobility graphene. *Nat. Photonics* **10**, 244-247 (2016).
53. S. A. Mikhailov *et al.* New electromagnetic mode in graphene. *Phys. Rev. Lett.* **99**, 016803 (2007).

54. S. G. Menabde *et al.* Direct optical probing of transverse electric mode in graphene. *Sci. Rep.* **6**, 21523 (2016).
55. D. A. Kuzmin *et al.* Transverse-electric plasmonic modes of cylindrical graphene-based waveguide at near-infrared and visible frequencies. *Sci. Rep.* **6**, 26915 (2016).
56. E. H. Hwang *et al.* Dielectric function, screening, and plasmons in two-dimensional graphene. *Phys. Rev. B* **75**, 205418 (2007).
57. C. H. Gan *et al.* Synthesis of highly confined surface plasmon modes with doped graphene sheets in the midinfrared and terahertz frequencies. *Phys. Rev. B* **85**, 125431 (2012).
58. J. A. Dionne *et al.* Are negative index materials achievable with surface plasmon waveguides? A case study of three plasmonic geometries. *Opt. Express* **16**, 19001-19017 (2008).
59. S. Thongrattanasiri *et al.* Complete optical absorption in periodically patterned graphene. *Phys. Rev. Lett.* **108**, 047401 (2012).
60. M. S. Jang *et al.* Tunable large resonant absorption in a midinfrared graphene Salisbury screen. *Phys. Rev. B* **90**, 165409 (2014).
61. R. L. Fante *et al.* Reflection properties of the Salisbury screen. *IEEE Trans. Antennas Propag.* **36**, 1443-1454 (1988).
62. W. J. Zhu *et al.* Carrier scattering, mobilities, and electrostatic potential in monolayer, bilayer, and trilayer graphene. *Phys. Rev. B* **80**, 235402 (2009).
63. L. A. Falkovsky *et al.* Space-time dispersion of graphene conductivity. *Eur. Phys. J. B* **56**, 281-284 (2007).
64. L. A. Falkovsky. Optical properties of graphene. *J. Phys. Conf. Ser.* **129**, 012004 (2008).
65. G. W. Hanson. Dyadic Green's functions and guided surface waves for a surface conductivity model of graphene. *J. Appl. Phys.* **103**, 064302 (2008).
66. P. R. Somani *et al.* Planer nano-graphenes from camphor by CVD. *Chem. Phys. Lett.* **430**, 56-59 (2006).
67. X. S. Li *et al.* Large-area synthesis of high-quality and uniform graphene films on copper foils. *Science* **324**, 1312-1314 (2009).
68. C. Mattevi *et al.* A review of chemical vapour deposition of graphene on copper. *J. Mater. Chem.* **21**, 3324-3334 (2011).
69. Y. Zhang *et al.* Review of chemical vapor deposition of graphene and related applications. *Acc. Chem. Res.* **46**, 2329-2339 (2013).
70. S. Bae *et al.* Roll-to-roll production of 30-inch graphene films for transparent electrodes. *Nat. Nanotechnol.* **5**, 574-578 (2010).

71. J. W. Suk *et al.* Transfer of CVD-grown monolayer graphene onto arbitrary substrates. *ACS Nano* **5**, 6916-6924 (2011).
72. K. S. Novoselov *et al.* Electric field effect in atomically thin carbon films. *Science* **306**, 666-669 (2004).
73. L. Wang *et al.* One-dimensional electrical contact to a two-dimensional material. *Science* **342**, 614-617 (2013).
74. X. S. Li *et al.* Large-area graphene single crystals grown by low-pressure chemical vapor deposition of methane on copper. *J. Am. Chem. Soc.* **133**, 2816-2819 (2011).
75. Z. Yan *et al.* Toward the synthesis of wafer-scale single-crystal graphene on copper foils. *ACS Nano* **6**, 9110-9117 (2012).
76. Y. F. Hao *et al.* The role of surface oxygen in the growth of large single-crystal graphene on copper. *Science* **342**, 720-723 (2013).
77. C. C. Wang *et al.* Growth of millimeter-size single crystal graphene on cu foils by circumfluence chemical vapor deposition. *Sci. Rep.* **4**, 4537 (2014).
78. S. R. Xing *et al.* Kinetic study of graphene growth: Temperature perspective on growth rate and film thickness by chemical vapor deposition. *Chem. Phys. Lett.* **580**, 62-66 (2013).
79. H. Wang *et al.* Controllable synthesis of submillimeter single-crystal monolayer graphene domains on copper foils by suppressing nucleation. *J. Am. Chem. Soc.* **134**, 3627-3630 (2012).
80. D. H. Jung *et al.* Effects of hydrogen partial pressure in the annealing process on graphene growth. *J. Phys. Chem. C* **118**, 3574-3580 (2014).
81. X. L. Liang *et al.* Toward clean and crackless transfer of graphene. *ACS Nano* **5**, 9144-9153 (2011).
82. E. V. Efremov *et al.* Achievements in resonance Raman spectroscopy review of a technique with a distinct analytical chemistry potential. *Anal. Chim. Acta* **606**, 119-134 (2008).
83. R. Beams *et al.* Raman characterization of defects and dopants in graphene. *J. Phys.: Condens. Matter* **27**, 083002 (2015).
84. A. C. Ferrari. Raman spectroscopy of graphene and graphite: Disorder, electron-phonon coupling, doping and nonadiabatic effects. *Solid State Commun.* **143**, 47-57 (2007).
85. L. M. Malard *et al.* Raman spectroscopy in graphene. *Phys. Rep.* **473**, 51-87 (2009).
86. A. C. Ferrari *et al.* Raman spectroscopy as a versatile tool for studying the properties of graphene. *Nat. Nanotechnol.* **8**, 235-246 (2013).
87. K. Xu *et al.* Graphene visualizes the first water adlayers on mica at ambient conditions. *Science* **329**, 1188-1191 (2010).

88. K. T. He *et al.* Scanning tunneling microscopy study and nanomanipulation of graphene-coated water on mica. *Nano Lett.* **12**, 2665-2672 (2012).
89. J. Chan *et al.* Reducing extrinsic performance-limiting factors in graphene grown by chemical vapor deposition. *ACS Nano* **6**, 3224-3229 (2012).
90. A. Pirkle *et al.* The effect of chemical residues on the physical and electrical properties of chemical vapor deposited graphene transferred to SiO₂. *Appl. Phys. Lett.* **99**, 122108 (2011).
91. Y. C. Lin *et al.* Graphene annealing: How clean can it be? *Nano Lett.* **12**, 414-419 (2012).
92. A. Das *et al.* Monitoring dopants by Raman scattering in an electrochemically top-gated graphene transistor. *Nat. Nanotechnol.* **3**, 210-215 (2008).
93. C. F. Chen *et al.* Controlling inelastic light scattering quantum pathways in graphene. *Nature* **471**, 617-620 (2011).
94. J. K. Liu *et al.* The dependence of graphene Raman D-band on carrier density. *Nano Lett.* **13**, 6170-6175 (2013).
95. J. Hong *et al.* Origin of new broad Raman D and G peaks in annealed graphene. *Sci. Rep.* **3**, 2700 (2013).
96. K. Kumar *et al.* The influence of thermal annealing to remove polymeric residue on the electronic doping and morphological characteristics of graphene. *Carbon* **65**, 35-45 (2013).
97. B. J. Kim *et al.* High-performance flexible graphene field effect transistors with ion gel gate dielectrics. *Nano Lett.* **10**, 3464-3466 (2010).
98. H. T. Liu *et al.* Chemical doping of graphene. *J. Mater. Chem.* **21**, 3335-3345 (2011).
99. L. Ju *et al.* Graphene plasmonics for tunable terahertz metamaterials. *Nat. Nanotechnol.* **6**, 630-634 (2011).
100. H. G. Yan *et al.* Tunable infrared plasmonic devices using graphene/insulator stacks. *Nat. Nanotechnol.* **7**, 330-334 (2012).
101. V. W. Brar *et al.* Highly confined tunable mid-infrared plasmonics in graphene nanoresonators. *Nano Lett.* **13**, 2541-2547 (2013).
102. Z. Y. Fang *et al.* Gated tunability and hybridization of localized plasmons in nanostructured graphene. *ACS Nano* **7**, 2388-2395 (2013).
103. V. W. Brar *et al.* Hybrid surface-phonon-plasmon polariton modes in graphene/monolayer h-bn heterostructures. *Nano Lett.* **14**, 3876-3880 (2014).
104. J. Kim *et al.* Electrical control of optical plasmon resonance with graphene. *Nano Lett.* **12**, 5598-5602 (2012).
105. Z. Y. Fang *et al.* Active tunable absorption enhancement with graphene nanodisk arrays. *Nano Lett.* **14**, 299-304 (2014).

106. V. W. Brar *et al.* Electronic modulation of infrared radiation in graphene plasmonic resonators. *Nat. Commun.* **6**, 7032 (2015).
107. V. Thareja *et al.* Electrically tunable coherent optical absorption in graphene with ion gel. *Nano Lett.* **15**, 1570-1576 (2015).
108. Z. Y. Li *et al.* Modulation of mid-infrared light using graphene-metal plasmonic antennas. *Appl. Phys. Lett.* **102**, 131108 (2013).
109. Y. Yao *et al.* Broad electrical tuning of graphene-loaded plasmonic antennas. *Nano Lett.* **13**, 1257-1264 (2013).
110. Y. Yao *et al.* Wide wavelength tuning of optical antennas on graphene with nanosecond response time. *Nano Lett.* **14**, 214-219 (2014).
111. Y. Yao *et al.* Electrically tunable metasurface perfect absorbers for ultrathin mid-infrared optical modulators. *Nano Lett.* **14**, 6526-6532 (2014).
112. Y. Zhang *et al.* Graphene based tunable metamaterial absorber and polarization modulation in terahertz frequency. *Opt. Express* **22**, 22743-22752 (2014).
113. M. M. Jadidi *et al.* Tunable terahertz hybrid metal-graphene plasmons. *Nano Lett.* **15**, 7099-7104 (2015).
114. P. Q. Liu *et al.* Highly tunable hybrid metamaterials employing split-ring resonators strongly coupled to graphene surface plasmons. *Nat. Commun.* **6**, 8969 (2015).
115. S. F. Shi *et al.* Optimizing broadband terahertz modulation with hybrid graphene/metasurface structures. *Nano Lett.* **15**, 372-377 (2015).
116. B. Zhao *et al.* Strong plasmonic coupling between graphene ribbon array and metal gratings. *ACS Photonics* **2**, 1611-1618 (2015).
117. S. Kim *et al.* Electronically tunable extraordinary optical transmission in graphene plasmonic ribbons coupled to subwavelength metallic slit arrays. *Nat. Commun.* **7**, 12323 (2016).
118. V. E. Dorgan *et al.* Mobility and saturation velocity in graphene on SiO₂. *Appl. Phys. Lett.* **97**, 082112 (2010).
119. Z. Fei *et al.* Edge and surface plasmons in graphene nanoribbons. *Nano Lett.* **15**, 8271-8276 (2015).
120. C. H. Wu *et al.* Large-area wide-angle spectrally selective plasmonic absorber. *Phys. Rev. B* **84**, 075102 (2011).
121. G. Volpe *et al.* Controlling the optical near field of nanoantennas with spatial phase-shaped beams. *Nano Lett.* **9**, 3608-3611 (2009).
122. L. Novotny *et al.* Antennas for light. *Nat. Photonics* **5**, 83-90 (2011).
123. D. M. Pozar. *Microwave engineering* (Wiley, 2012).

124. P. Q. Mantas. Dielectric response of materials: Extension to the Debye model. *J. Eur. Ceram. Soc.* **19**, 2079-2086 (1999).
125. C. Sönnichsen *et al.* Plasmon resonances in large noble-metal clusters. *New J. Phys.* **4**, 93.1-93.8 (2002).
126. N. Engheta *et al.* Circuit elements at optical frequencies: Nanoinductors, nanocapacitors, and nanoresistors. *Phys. Rev. Lett.* **95**, 095504 (2005).
127. G. Georgiou *et al.* Active loaded plasmonic antennas at terahertz frequencies: Optical control of their capacitive-inductive coupling. *Phys. Rev. B* **91**, 125443 (2015).
128. J. Kistner *et al.* Photoluminescence from silicon nitride-no quantum effect. *J. Appl. Phys.* **110**, (2011).
129. G. C. Schwartz *et al.* The effective dielectric-constant of silicon dioxides deposited in the spaces between adjacent conductors. *J. Electrochem. Soc.* **139**, L118-L122 (1992).
130. P. A. Khomyakov *et al.* Nonlinear screening of charges induced in graphene by metal contacts. *Phys. Rev. B* **82**, 115437 (2010).
131. H. G. Yan *et al.* Infrared Spectroscopy of Tunable Dirac Terahertz Magneto-Plasmons in Graphene. *Nano Lett.* **12**, 3766-3771 (2012).
132. J. Christensen *et al.* Graphene plasmon waveguiding and hybridization in individual and paired nanoribbons. *ACS Nano* **6**, 431-440 (2012).
133. R. Alaei *et al.* A perfect absorber made of a graphene micro-ribbon metamaterial. *Opt. Express* **20**, 28017-28024 (2012).
134. M. Liu *et al.* Double-layer graphene optical modulator. *Nano Lett.* **12**, 1482-1485 (2012).
135. S. H. Mousavi *et al.* Inductive tuning of Fano-resonant metasurfaces using plasmonic response of graphene in the mid-infrared. *Nano Lett.* **13**, 1111-1117 (2013).
136. P. Genevet *et al.* Holographic optical metasurfaces: A review of current progress. *Rep. Prog. Phys.* **78**, (2015).
137. N. Meinzer *et al.* Plasmonic meta-atoms and metasurfaces. *Nat. Photonics* **8**, 889-898 (2014).
138. X. Zhang *et al.* Microscopic analysis of surface Bloch modes on periodically perforated metallic surfaces and their relation to extraordinary optical transmission. *Phys. Rev. B* **89**, (2014).
139. D. Dubreuil *et al.* Optical and electrical properties between 0.4 and 12 μm for Sn-doped In_2O_3 films by pulsed laser deposition and cathode sputtering. *Appl Optics* **46**, 5709-5718 (2007).
140. P. Pal *et al.* RF sputtered silicon for MEMS. *J Micromech Microeng* **15**, 1536-1546 (2005).
141. G. Khitrova *et al.* Vacuum Rabi splitting in semiconductors. *Nat. Phys.* **2**, 81-90 (2006).

142. G. S. Agarwal. Vacuum-field Rabi splittings in microwave absorption by Rydberg atoms in a cavity. *Phys. Rev. Lett.* **53**, 1732-1734 (1984).
143. S. Rudin *et al.* Oscillator model for vacuum Rabi splitting in microcavities. *Phys. Rev. B* **59**, 10227-10233 (1999).
144. K. Imura *et al.* Anomalous light transmission from plasmonic-capped nanoapertures. *Nano Lett.* **11**, 960-965 (2011).
145. J. A. Hutchison *et al.* Absorption-induced transparency. *Angew Chem Int Edit* **50**, 2085-2089 (2011).
146. S. G. Rodrigo *et al.* Theory of absorption-induced transparency. *Phys. Rev. B* **88**, (2013).
147. P. L. Levesque *et al.* Probing charge transfer at surfaces using graphene transistors. *Nano Lett.* **11**, 132-137 (2011).
148. S. Ryu *et al.* Atmospheric oxygen binding and hole doping in deformed graphene on a SiO₂ substrate. *Nano Lett.* **10**, 4944-4951 (2010).
149. M. Quinten *et al.* Electromagnetic energy transport via linear chains of silver nanoparticles. *Opt Lett* **23**, 1331-3 (1998).
150. M. L. Brongersma *et al.* Electromagnetic energy transfer and switching in nanoparticle chain arrays below the diffraction limit. *Phys. Rev. B* **62**, 16356-16359 (2000).
151. S. A. Maier *et al.* Local detection of electromagnetic energy transport below the diffraction limit in metal nanoparticle plasmon waveguides. *Nat. Mater.* **2**, 229-232 (2003).
152. B. Willingham *et al.* Energy transport in metal nanoparticle chains via sub-radiant plasmon modes. *Opt. Express* **19**, 6450-6461 (2011).
153. D. Solis, Jr. *et al.* Electromagnetic energy transport in nanoparticle chains via dark plasmon modes. *Nano Lett* **12**, 1349-53 (2012).
154. U. Fano. Effects of configuration interaction on intensities and phase shifts. *Phys. Rev.* **124**, 1866-1878 (1961).
155. A. E. Miroshnichenko *et al.* Fano resonances in nanoscale structures. *Rev. Mod. Phys.* **82**, 2257-2298 (2010).
156. B. Luk'yanchuk *et al.* The Fano resonance in plasmonic nanostructures and metamaterials. *Nat. Mater.* **9**, 707-715 (2010).
157. P. Y. Fan *et al.* Optical Fano resonance of an individual semiconductor nanostructure. *Nat. Mater.* **13**, 471-475 (2014).